High-temperature diode formed by epitaxial GaP layers

M. M. Sobolev and V. G. Nikitin

A. F. Ioffe Physicotechnical Institute, Russian Academy of Sciences, St. Petersburg

(Submitted October 22, 1997)
Pis'ma Zh. Tekh. Fiz. **24**, 1–7 (May 12, 1998)

The preparation of pure, undoped, high-temperature GaP grown by liquid-phase epitaxy is reported. Results are presented of studies of GaP $p-n$ structures grown at various crystallization initiation temperatures, using the capacitance–voltage ($C-V$) method and deep-level transient spectroscopy (DLTS). The characteristics of GaP are determined by the low concentration of background impurities and deep-level defects. Measurements of the temperature dependence of the forward branch of the current–voltage characteristic showed that the thermometric characteristic of the diode is linear between -191 and $\sim+600\,^{\circ}$C. © *1998 American Institute of Physics.* [S1063-7850(98)00105-0]

Gallium phosphide is now widely used to fabricate light-emitting diodes in the visible range. Wide-gap GaP may also be regarded as a promising material to develop high-temperature electronics devices and photodetectors.[1] However, its application is impeded by the difficulties involved in producing comparatively pure GaP with a background impurity level lower than 10^{16} cm^{-3} and a concentration of deep-level point defects less than 10^{14} cm^{-3}. Reports of the preparation of GaP with a residual donor impurity concentration of the order of 10^{14}–10^{15} cm^{-3} have appeared only comparatively recently.[2,3] A low level of residual impurities is an important requirement for the preparation of high-temperature GaP but is not the only one. Another equally important criterion which determines the production of high-temperature, thermally stable GaP is the presence of deep-level point defects formed during the epitaxial growth process. It is known[4] that the intrinsic properties of GaP, the concentration and presence of defects, and also the behavior of background impurities in the material is determined by the degree of deviation from stoichiometry and thus by the region of homogeneity which depends on the crystallization temperature. This explains the need to study the quality of epitaxial undoped GaP layers—the concentrations of free carriers and deep-level defects—as a function of the technological growth conditions of the epitaxial layers, especially the crystallization initiation temperature.

Here we report the preparation of pure, undoped, high-temperature GaP. Results are presented of studies of GaP $p-n$ structures using the capacitance–voltage ($C-V$) method and deep-level transient spectroscopy (DLTS). The thermometric characteristic of a GaP diode structure is also presented.

Layers of n-GaP were grown by liquid-phase epitaxy by cooling a Ga-P flux at a constant rate of 0.1–0.3 °C/min. The substrates were [100]-oriented n- and p-type GaP wafers with a carrier concentration of $\sim 10^{18}$ cm^{-3}, grown by the Czochralski method. The epitaxial growth process was carried out in a hydrogen stream with a dew point of -65 C at crystallization initiation temperatures of 700–950 °C. The thicknesses of the epitaxial layers were of the order of 5–20 μm. Doped n^+-type epitaxial layers in $p^+-n^0-n^+$ structures and p^+-type layers in n^+-n^0-p^+ structures were obtained by incorporating Si and Mg in the fluxes, respectively. The Hall effect was measured by the four-probe method using layers grown on semi-insulating GaP substrates. The $C-V$ and DLTS measurements were made using a Bio-Rad DLTS 4600 spectrometer. The presence of a p-n structure allowed us to study deep traps of majority and minority carriers by applying suitable filling pulses to the sample. The duration of these filling pulses was 5 ms. The temperature of the sample in the cryostat was swept between 80 and 450 K. The thermal activation energy E and the capture cross section σ were determined using the Arrhenius dependence of T/e on $1000/T$, where e is the rate of electron and hole emission and T is the maximum temperature of the DLTS peak. The concentrations of deep-level defects and impurities were determined from the relation $N_t=2(N_d-N_a)|\Delta C|_m/C_0$, where N_d-N_a is the concentration of uncompensated shallow donor levels, $|\Delta C|_m$ is the height of the DLTS peak, and C_0 is the steady-state capacitance of the depleted layer at appropriate reverse biases.

Figures 1a and 1b show the changes in the concentration of free electrons and their mobility in undoped epitaxial GaP n^0 layers, determined using the Hall effect and $C-V$ measurements, plotted as a function of the crystallization initiation temperature T_0. The results of the Hall measurements showed that the compensation coefficient in our epitaxial GaP n^0 layers is less than 0.5 and the shallow donor concentration N_d is thus much higher than the acceptor concentration N_a and $n=N_d-N_a\cong N_d$. It can be seen from the results plotted in Fig. 1 that as T_0 increases, the concentration of free electrons in the layers decreases while their mobility increases. The free electron concentration in the layers varies between 1.5×10^{17} cm^{-3} and 7×10^{14} cm^{-3}. The electron mobility at room temperature in GaP layers grown at $T\cong 900\,^{\circ}$C was 200–250 cm^2/V·s. At liquid nitrogen temperature the mobility increased by an order of magnitude. In the purest samples with $n\approx 5\times10^{14}$ cm^{-3}, the mobility reached 3000 cm^2/V·s. The DLTS measurements made for

 © 1998 American Institute of Physics

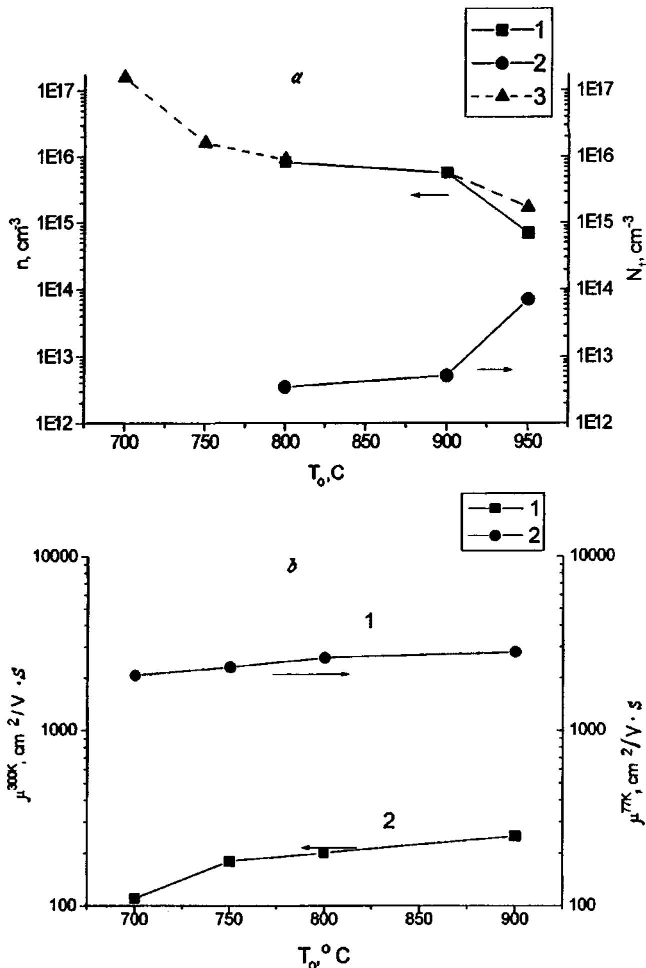

FIG. 1. a — Concentration of free electrons (n) determined by C–V measurements (*1*) and the Hall effect (*2*), and also of deep-level defects in undoped epitaxial n-layers of GaP as a function of the crystallization initiation temperature T_0; b — electron mobility in undoped epitaxial n-layers of GaP determined at liquid-nitrogen (n^{77K}) (*1*) and room temperature (n^{300K}) (*2*) as a function of crystallization initiation temperature T_0.

these samples revealed a low concentration of deep-level defects. The lowest concentration N_t was observed at $T_0=800$ °C and was 3.5×10^{12} cm^{-3} (Fig. 1a). Over the entire temperature range of the DLTS measurements, the DLTS spectrum for the sample with $T_0=800$ °C comprised a continuous wide band, attributed to the majority carriers, in which no levels could be isolated. When T_0 increased to 900 °C, the concentration of deep-level defects increased (Fig. 1a). Two separate peaks associated with hole traps could be identified in the DLTS spectra (Fig. 2). The level parameters were respectively FH1=290 meV, $\sigma_p=6.1\times10^{-17}$ cm^2 and FH2=649 meV, $\sigma_p=3.0\times10^{-11}$ cm^2. At $T_0=950$ °C, a further increase in the concentration of minority carrier traps was observed (Fig. 1a). As in the previous case, two peaks associated with hole traps could be identified in the DLTS spectrum (Fig. 2) but with different parameters: FH3=106 meV, $\sigma_p=3.7\times10^{-21}$ cm^2 and FH4=807 meV, $\sigma_p=4.8\times10^{-13}$ cm^2. The FH2 and FH4 hole traps were similar to the H3 and H7 levels, respectively, which were observed previously in GaP grown by liquid-phase epitaxy,[5] but their nature was not established. It is noted in Ref. 5 that no electron traps were observed, which is typical of GaP grown from a phosphorus-gallium flux. For the n^+–n^0–p^+ structure obtained at $T_0=800$ °C we measured the forward voltage drops across the diode as a function of temperature during passage of a direct current (100 mA) in the range between 191 and ~600 °C. Figure 3 shows that the thermometric characteristic of the diode when forward biased is linear over the entire temperature range studied.

We shall now discuss the results of our studies of the concentration of electrons and deep-level defects as a function of the crystallization initiation temperature. The electron concentration in the undoped layers decreases as the crystallization initiation temperature increases and their mobility increases accordingly. A probable reason for the observed changes is that the majority residual impurities in GaP are shallow volatile S, Se, and Te donors. The high concentration of electrons in the layers obtained at comparatively low growth temperatures may be attributed to the incomplete purification of the flux from volatile impurities. As T_0 increases further, the conditions for removal of these impurities improve and the concentration of free electrons in the epitaxial

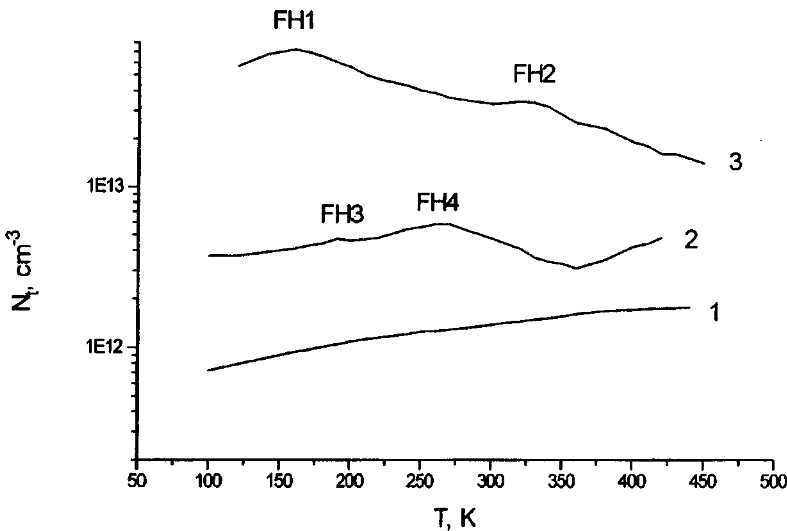

FIG. 2. DLTS spectra of undoped epitaxial n-layers of GaP grown at crystallization initiation temperatures of 800 °C (*1*), 900 °C (*2*), and 950 °C (*3*).

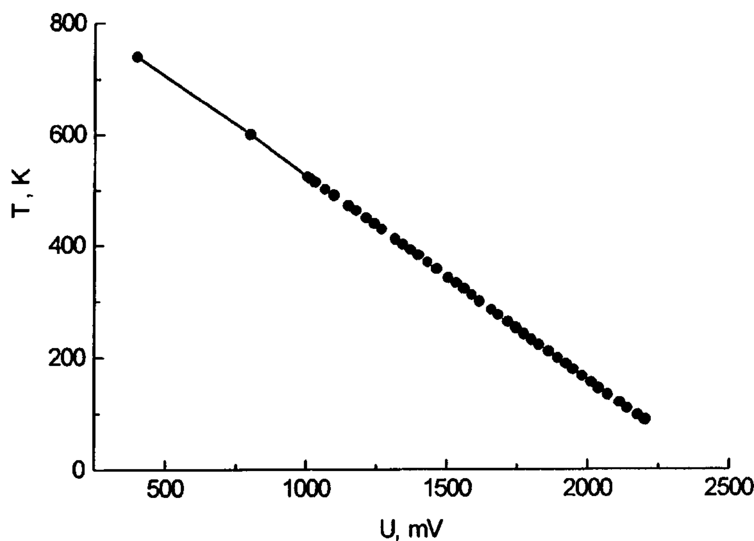

FIG. 3. Forward voltage drops across GaP diode versus temperature during passage of a direct current (100 mA).

GaP layers decreases. The observed increase in the concentration of hole traps (Fig. 1b) with increasing crystallization initiation temperature in the epitaxial GaP layers is consistent with the results of theoretical estimates of the heats of defect formation.[6] These estimates show that as T_0 increases during growth of GaP from a P-Ga flux, the GaP composition shows an increasing shift from stoichiometry in favor of Ga, which should increase the concentration of V_p and Ga_p defects or their vacancy complex $V_pGa_pV_p$.

To sum up, the results of our investigations show that GaP layers grown by liquid-phase epitaxy may form the basis for devices operating at extremely high temperatures, up to 600 °C, which cannot be achieved by using conventional materials such as Si and GaAs. These characteristics of GaP are determined by the low concentration of background impurities and deep-level defects which ensured that the diode had a linear thermometric characteristic when forward biased over the entire temperature range studied.

[1] Th. E. Zipperian, R. J. Chaffin, and L. R. Dawson, IEEE Trans. Ind. Electron. **IE-29**, 129 (1982).
[2] W. H. Weichold, Solid-State Electron. **28**, 957 (1985).
[3] R. F. Brunwin, P. J. Dean, B. Hamilton, J. Holdgkinson, and A. R. Peaker, Solid-State Electron. **24**, 249 (1981).
[4] V. M. Andreev, L. M. Dolginov, and D. N. Tret'yakov, *Liquid-Phase Epitaxy in the Technology of Semiconductor Devices* [in Russian], Sovetskoe Radio, Moscow (1975).
[5] P. M. Monney, T. A. Kennedy, and M. B. Small, Physica B & C **116**, 431 (1983).
[6] J. A. Van Vechten, *Handbook on Semiconductors. Materials, Properties, and Preparation*, Vol. 3, edited by T. S. Moss and S. P. Keller (North–Holland, Amsterdam, 1980), pp. 1–11.

Translated by R. M. Durham
Edited by David L. Book

Permittivity of strontium titanate film in a $SrTiO_3/Al_2O_3$ structure

A. M. Prudan, E. K. Gol'man, A. B. Kozyrev, A. A. Kozlov, and V. L. Loginov

St. Petersburg Electrotechnical University

(Submitted September 23, 1997)
Pis'ma Zh. Tekh. Fiz. **24**, 8–12 (May 12, 1998)

It is shown that strontium titanate film has the same Curie temperature as the single crystal. The minimum temperature above which the permittivities are the same is determined. The dielectric nonlinearity is investigated over a wide range of field strengths. © *1998 American Institute of Physics.* [S1063-7850(98)00205-5]

Multilayer structures containing strontium titanate film synthesized on the surface of dielectrics (Al_2O_3, $LaAlO_3$, $NbGaO_3$) by various methods are interesting for practical applications in microwave electronics. In most cases, the films have a perovskite $SrTiO_3$ structure.[1–3] However, the possibility of obtaining more complicated compounds of the SrO type $(SrTiO_3)_n$ during the synthesis process cannot be discounted.[4]

A review of the published literature draws attention to the following fact. In most cases, $SrTiO_3$ films have a perovskite crystal lattice but the values of the permittivity (ε_F) at room temperature cover a wide range: $\varepsilon_F \in$ 90–350 (Refs. 1–4). For comparison the permittivity of a $SrTiO_3$ single crystal at $T \approx$ 300 K is 340–360. In addition, no studies have been carried out to identify the film material from the standpoint of the $\varepsilon_F(T)$ dependence typical of a ferroelectric. The aim of the present study is to confirm the correspondence between the perovskite crystal structure of the film material and the known permittivity of a $SrTiO_3$ single crystal.

The film was deposited by magnetron sputtering of a ceramic $SrTiO_3$ target on a single-crystal Al_2O_3 (r-cut) wafer ($12.0\times12.0\times0.5$ mm) whose surface contained a set of planar platinum electrodes. The sputtering was carried out in a gas mixture ($0.7O_2+0.3$ Ar) at pressure $P\sim4$ Pa and substrate temperature $T=700$°C. The film thickness was $h=0.8\,\mu$m.

X-ray structural analysis of the multilayer system ($SrTiO_3/Pt/Al_2O_3$) showed that the film has a perovskite crystal lattice preferentially oriented in the (100) direction relative to the substrate surface. In the [100] direction the unit cell was lengthened ($a=0.3941$ nm) compared with the single crystal ($a_0=0.3902$ nm). The results of an x-ray diffraction analysis revealed a fine-grained structure. An examination of the surface using electron force microscopy also revealed cavities up to 100 nm in diameter.

A four-probe method (using an E7-12 meter) at 1 MHz was employed to investigate the temperature behavior of the capacitance $C(T)$ of planar capacitors having a multilayer $SrTiO_3$/Pt(capacitor electrodes)/Al_2O_3 structure. The gap between the electrodes in the capacitor was $3\,\mu$m. The temperature dependence of the capacitance $C(T)$ was measured without an electric field, $C(0,T)$, and with control voltages U_i applied to the capacitor electrodes for which the dependence $C(U_i,T)$ revealed a maximum in the range $T>78$ K. The capacitance–voltage characteristics $C(U,T_i)$ were measured at two temperatures ($T_i=78$ and 290 K) in the voltage range $U=0$–200 V. The capacitors typically exhibited the following relative changes in the total capacitance:

$$C(0,78\text{ K})/C(0,290\text{ K})\cong1.9,$$

$$C(0,78\text{ K})/C(200\text{ V},78\text{ K})\cong2.7,$$

$$C(0,290\text{ K})/C(200\text{ V},290\text{ K})\cong1.4.$$

The interelectrode gap in a planar capacitor has an inhomogeneous dielectric filling (air, substrate, film) and it is reasonable to assume that the $SrTiO_3$ film also possesses nonuniform permittivity. This nonuniformity may be caused by the presence of air inclusions (cavities) and by the appearance of boundary conditions for the polarization vector at the surface of the crystallites.[5] In simplified terms, the total capacitance C of the capacitor may be represented by an equivalent circuit containing three components C_S, C_L, and C_F of which two (C_L and C_F) are connected in series. Each component characterizes the energy of the electric field in air and the substrate C_S, in regions of the film with low permittivity C_L, and in regions of the film with ferroelectric filling C_F. In this case, the required permittivity of the ferroelectric material may be determined from

$$\varepsilon_F=\frac{1}{\varepsilon_0 F_F}\left(\frac{1}{C-C_S}-\frac{1}{C_L}\right)^{-1}, \tag{1}$$

where F_F is the form factor of the capacitance C_F and $\varepsilon_0=8.85\times10^{-12}$ F/m is the dielectric constant.

The values of C, C_S, C_L, and F_F on the right-hand side of Eq. (1) can be measured. The capacitance C_S is determined by analyzing the correspondence between the dependence $C(0,T)$ and a Curie-type function $C(0,T)=A/(T-T_0)$ (Ref. 6). The component C_L is determined using a relation which links the permittivities with the control field, $\varepsilon_F(E_i,T_m)$, and without it, $\varepsilon_F(0,T_m)$, at the temperature T_m for which $\varepsilon_F(E_i,T)$ has a maximum. An analysis of the dependence $C_F(0,T)$ yielded the Curie temperature characteristic of a $SrTiO_3$ single crystal. Using the Curie constant (C_C) as the true constant for a ferroelectric allowed us to determine the form factor

 © 1998 American Institute of Physics

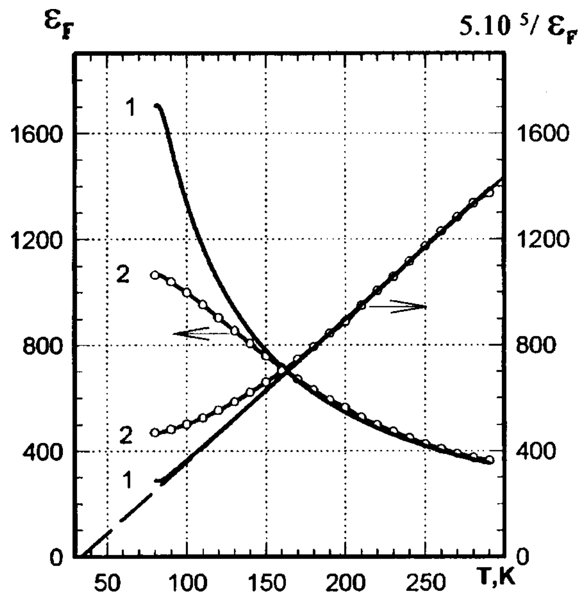

FIG. 1. Temperature dependence of the permittivity (ε_F): *1* — single-crystal strontium titanate and *2* — strontium titanate film on an Al_2O_3 (r-cut) surface with zero ($E=0$) bias field. Film thickness $h=0.8\mu$m.

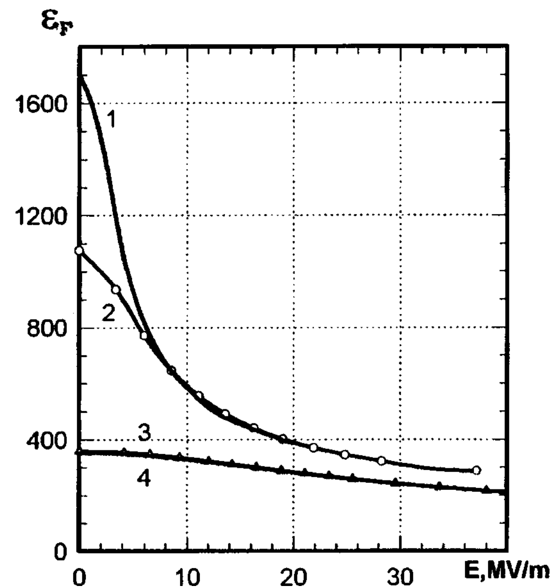

FIG. 2. Permittivity of single crystal strontium titanate (*1*, *3*) and strontium titanate film (*2*, *4*) versus external electric field strength at $T=78$ K (*1*, *2*) and $T=290$ K (*3*, *4*).

$$F_F=\frac{1}{\varepsilon_0 C_C}\,\frac{d(1/(C-C_S))}{dT}. \qquad (2)$$

For one of the capacitors we obtained the following values: $C(0.78\ \text{K})=1.44$ pF, $C_S=0.14$ pF, $C_L=2.71$ pF, and $F_F=1.37\times10^{-4}$ m.

The results of analysis of the raw data $C(U,T)$ using this algorithm are plotted in Figs. 1 and 2. The $SrTiO_3$ film has a Curie temperature (Fig. 1) corresponding to that of single-crystal strontium titanate ($T_C=38$ K). In the range 180 K $<T<$ 300 K, the film material and the $SrTiO_3$ crystal are indistinguishable in terms of permittivity and temperature behavior, although some departure from the Curie law is observed (Fig. 1) at a higher temperature ($T\cong180$K) than that for the crystal ($T\cong100$ K).

The design of the capacitor allowed us to investigate the dielectric nonlinearity of $SrTiO_3$ over a wide range (up to $E\sim10^8$ V/m) of electric field strengths (Fig. 2). The permittivity varies substantially under the action of the field, even at room temperature. A similar result was obtained for a control field oriented normal to the film.[3]

In the range $T>180$ K the absolute values and temperature dependence of the permittivity of strontium titanate film with a perovskite crystal lattice on the surface of an Al_2O_3 (r-cut) substrate are indistinguishable from those of a free $SrTiO_3$ crystal. The difference observed in the range $T<180$ K is probably caused by the mechanical action of the substrate on the film as a result of the mismatch between the temperature coefficients of linear expansion.[6]

[1] Yu. A. Boĭkov, I. P. Pronin, Z. G. Ivanov *et al.*, Fiz. Tverd. Tela (St. Petersburg) **38**, 133 (1996) [Phys. Solid State **38**, 72 (1996)].
[2] F. A. Miranda, C. H. Mueller, and G. A. Koepf, Supercond. Sci. Technol. **8**, 755 (1995).
[3] S. Komatsu and K. Abe, J. Appl. Phys. **34**, 3597 (1995).
[4] T. Hirano, M. Taga, and T. Kobayashi, J. Appl. Phys. **32**, L3597 (1993).
[5] O. G. Vendik, S. P. Zubko, and L. T. Ter-Martirosyan, Fiz. Tverd. Tela (St. Petersburg) **38**(12), 3654 (1996) [Phys. Solid State **38**, 1991 (1996)].
[6] A. M. Prudan, E. K. Gol'man, A. B. Kozyrev, R. N. Kyutt, and V. E. Loginov, Fiz. Tverd. Tela (St. Petersburg) **39**, 1024 (1997) [Phys. Solid State **39**, 920 (1997)].

Translated by R. M. Durham
Edited by David L. Book

Observation of carbon segregation and evolution of vacancy defects in a surface layer of iron exposed to a low-energy high-current electron beam

V. I. Lavrent'ev, A. D. Pogrebnyak, A. D. Mikhalev, N. A. Pogrebnyak, R. Shandrik, A. Zecca, and Yu. V. Tsvintarnaya

Sumy Institute of Surface Modification

(Submitted November 28, 1997)
Pis'ma Zh. Tekh. Fiz. **24**, 13–20 (May 12, 1998)

For the first time, Rutherford backscattering (RBS) and proton-induced x-ray emission (PIXE) using a proton microbeam and a slow positron beam were used to analyze (scan) the surface and near-surface layers of α-Fe after exposure to a low-energy high-current electron beam. Grain-boundary segregation of carbon and the formation of impurity complexes were observed. Proton microbeam scanning revealed regions of reduced local density which are sources of crater formation. © *1998 American Institute of Physics.* [S1063-7850(98)00305-X]

Beam technologies are now fairly widely used to modify the surface of metals and enhance their performance characteristics.[1–4] Electron-beam treatment is a typical representative of this type of treatment and is used to refine surface layers to the melting depth of the layers.[5]

Pulsed treatment by a low-energy high-current electron beam is accompanied by melting of the surface layer, which gives rise to high concentrations of point and linear defects.[6,7] Reliable data on the defects formed by pulsed treatment are required to study the nature of the energy absorption mechanisms. So far, few studies have been made of these mechanisms, mainly because of the limited capabilities of experimental methods to investigate thin (between a few nanometers and a micrometer thick) surface layers with a nonuniform distribution of defects over depth.[2]

Thus, our aim was to study characteristic features of the defect structure and the redistribution of carbon atoms in a surface layer of α-Fe exposed to a low-energy high-current electron beam, using a combination of modern nuclear-physical methods.

It should be noted that in a series of studies made by the authors, it was shown that an increase in the number of pulses during exposure to a low-energy high-current electron beam sharply reduces the number of craters on the surface,[5–8] which appreciably enhances the corrosion resistance, improves the dry-friction resistance, and increases the fatigue strength under cyclic loading.[5,8]

For the experiments we used samples 12 mm in diameter and around 2 mm thick, with a grain size of approximately 3 mm. The total impurity content was at most 0.01 wt.% and the initial dislocation density was 10^8 cm^{-2}. The samples were bombarded using a Nadezhda-2 electron source with an average energy varying between 6 and 20 keV, a pulse length of around 0.8 μs, and pulse energy density W between 2.5 and 5.2 J/cm^2 (Ref. 8). The defect structure (vacancy subsystem) was analyzed using a slow positron beam (Trento University, Italy[9]) by measuring the lifetime τ_p and the S-parameter of the Doppler broadening of the annihilation peak.[9] The positron lifetime was measured using a 12 μCi Na($\beta+\gamma$) positron source in a Mylar envelope. The positron lifetime in the source was described by two components: $\tau_1=250$ ns, $I_1=6.2\%$, $\tau_2=450$ ns, $I_2=2.5\%$ (Ref. 10).

A ^{207}Bi source was used for calibration. The distribution of elements along the surface of the sample was analyzed qualitatively using color maps of areas between 100×100 and 2500×2500 μm, obtained by RBS and PIXE as a result of scanning with a 3 MeV proton beam (Oxford University). The microbeam current was 100 pA and the diameter less than 1 μm. Figure 1 shows energy spectra of the S-parameter of the Doppler broadening of the annihilation peak of α-Fe samples before and after single bombardment by an electron beam with different energy density W. In fact, these curves

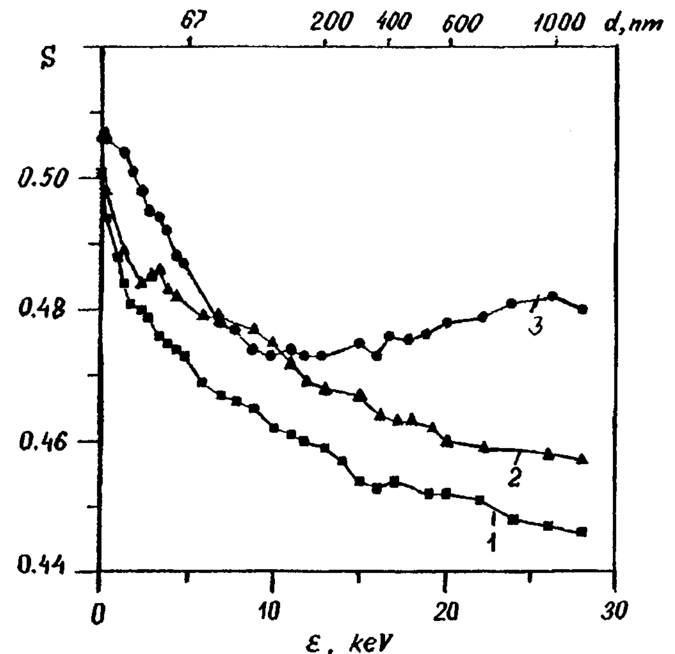

FIG. 1. S-parameter of the positron annihilation Doppler broadening curves, measured using a slow positron beam in α-Fe samples, as a function of layer depth (or positron energy): *1* — initial state, *2* — after exposure to a 2.5 J/cm^2 electron beam, and *3* — after exposure to a 4.2 J/cm^2 electron beam, $\tau=0.8$ μs.

 © 1998 American Institute of Physics

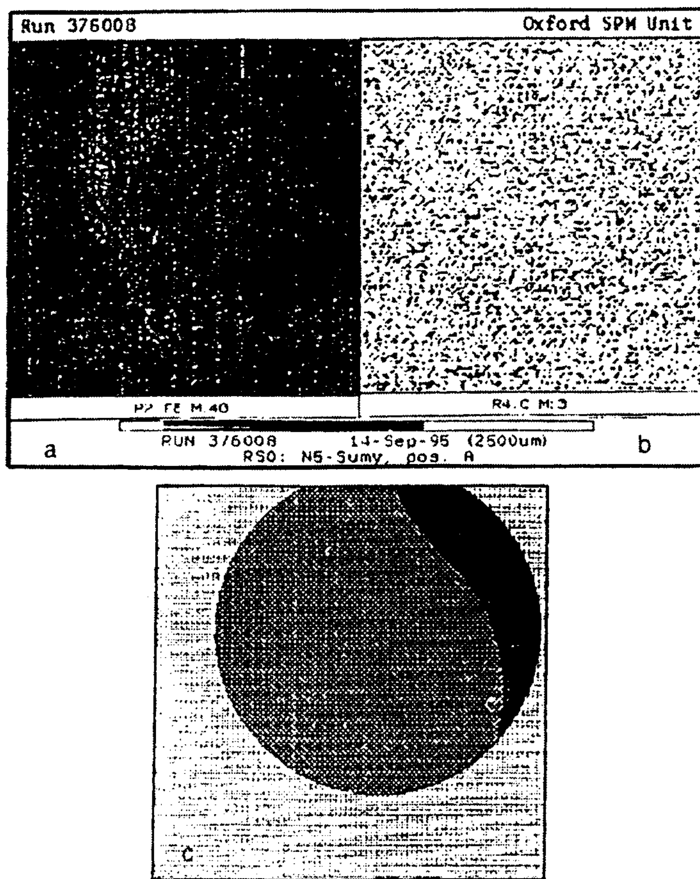

FIG. 2. Qualitative analysis of the distribution of elements in various surface microregions after exposure of an α-Fe sample to a 2.5 J/cm^2 electron beam using maps (color) of 2500×2500 μm areas: a — Fe, b — carbon, c — diagram of Fe surface distribution showing the distribution in Fig. 1a more clearly.

show the distribution of the vacancy defect concentration as a function of doping depth below the plane of the surface. The results indicate an increased vacancy concentration over the entire depth analyzed (up to 1.02 μm), starting at 20 nm. An increase in the energy flux density from 0.1 to 4.5 J/cm^2 increases the S parameter for the entire range of positron energies.

A further increase in W to 5.2 J/cm^2 is accompanied by a drop in the concentration of vacancy defects (S-parameter), especially in the near-surface layers (up to 400 nm).

A study of the distributions of the atomic composition of the surface of α-Fe samples exposed to low energy densities (W up to 3.5 J/cm^2) by RBS and PIXE by proton microbeam scanning revealed the presence of carbon impurities distributed comparatively uniformly in the regions studied with an average concentration of 10–15 at.% (Fig. 2b). No other impurities were observed in these experiments. However, the color maps which show the distribution of iron reveal characteristic ''shading,'' having a circular profile of around 2000 μm (Fig. 2a). The diagram in Fig. 2c gives a clearer picture of this iron distribution in black and white.

When the surface of the metal is exposed to a low-energy high-current electron beam at this energy, the depth profile with absorbed energy initially has the form of a Gaussian distribution with a maximum at a depth of around 1 μm.

Calculations made using a numerical solution of the one-dimensional heat conduction equation for α-Fe bombarded by a 6–20 keV electron beam (pulse length $\tau=0.8$ μs) showed that as W is increased from 2.3 to 5.2 J/cm^2, the thickness of the molten layer and its lifetime increase from 0.7 to 2.5 μm and from 0.5 to 3 μs, respectively.[8,11] The rate of cooling of the surface layer of α-Fe is 5×10^9 K/s and the velocity of the crystallization front varies between 2 and 5 m/s as a function of the cooling time and layer depth.[4]

The results of a simulation of the melting of the near-surface layers of α-Fe exposed to a pulsed electron beam indicate that at energy densities of at least 3 J/cm^2 the upper surface layer at a depth of around 1 μm undergoes quenching. At these high quenching rates of 5×10^9 K/s a high concentration of nonequilibrium vacancies forms (up to 10^{-3} at.%) (Ref. 12), which are confirmed by positron annihilation. The component $\tau_1=108$ ns of the lifetime obtained as a result of irradiation of α-Fe ($W=3.3$ J/cm^2) corresponds to the lifetime in a defect-free iron crystal lattice.[11] The second component $\tau_2=195$ ns is close to the lifetime of positrons captured by divacancies.[13] Thus, the nonequilibrium vacancies formed at low electron beam energy densities W mainly combine to form divacancies. The maximum concentration of divacancies is initially found at a depth of around 1 μm, which corresponds to the maximum absorbed energy. As the temperature rises and the heat becomes redistributed, the layers of material closer to the surface are heated faster because the rate of increase in temperature in the surface layers is greater than the rate of decrease inside the material (rate of heat removal).[12] As a result, most of the nonequilibrium vacancies (divacancies) tend toward the surface. The easiest

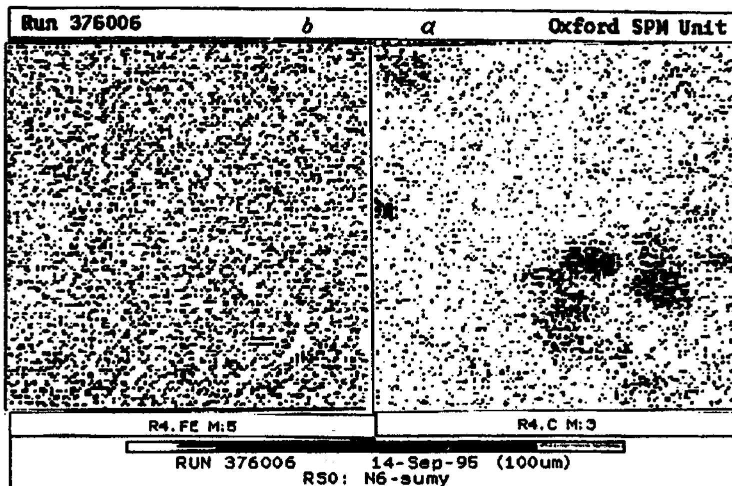

FIG. 3. Qualitative analysis of the distribution of elements in various surface microregions after exposure of an α-Fe sample to ten pulses of a 4.2 J/cm^2 electron beam using maps (color) of 100×100 μm areas: a — carbon distribution, b — Fe distribution.

paths for the migration of vacancies are along dislocations and grain boundaries.

Thus, the local density of material should decrease near these defects. This is precisely the effect observed in studies of the surface distribution of elements in an α-Fe sample exposed to an electron beam with low W (up to 3 J/cm^2), when the iron distribution patterns along the boundary of a region having the size of a grain reveal shading, which indicates a reduction in the local density of material at these points (Fig. 2c).

The migration of nonequilibrium vacancies toward the surface is confirmed by an increase in the S-parameter in the near-surface layers (Fig. 1). These regions of reduced local density are evidently sources of crater nucleation on the surface of a material exposed to a low-energy high-current electron beam with elevated energy densities.[14]

Measurements of the second component of the positron lifetime $\tau_2^1=165$ ns when the beam energy density is increased to $W=4.2$ J/cm^2 indicate that the nonequilibrium vacancies combine to vacancy–carbon atomic complexes.[15]

Under the action of the strain wave generated by the electron beam, carbon migrates into the material, which is responsible for the extended spatial distribution of carbon–vacancy complexes and the higher values of the S parameter in the deeper layers (Fig. 1).

As a result of redistribution, some of the vacancies annihilate with interstitial atoms, which causes the intensity of the second component to decrease with increasing W. In addition, in this last case a decrease in I_2 may be caused by the formation of ''vacancy 2–3 carbon atom'' complexes as a result of the increased carbon concentration. The binding energy of a positron with a vacancy in these complexes decreases sharply because the addition of carbon to vacancy–carbon atom complexes reduces the capacity of a positron to be trapped in the forming states.[15]

When the number of pulses is increased from 1 to 10 or more (at elevated energy densities around 4.2 J/cm^2), the region of localization decreases abruptly and the concentration of carbon in these regions increases (Fig. 3), i.e., carbon segregation is observed in regions of reduced density and craters form in these regions.

Thus, the use of nuclear physics method (RBS and PIXE, slow positron annihilation) has allowed us to study the evolution of vacancy defects in near-surface layers of α-Fe after exposure to a low-energy high-current electron and to observe the onset of carbon segregation as the number of pulses increases. It was observed that the absorption of energy deposited in the sample by the electron beam leads to the formation of regions of reduced local density at the surface of the sample near the initial grain boundary. Nonequilibrium vacancies expelled by the thermal front from the quenched upper-surface layer are concentrated in these regions. When the energy density or number of pulses are increased, these regions may form a source of crater nucleation. At the same time, an increase in the carbon concentration in local regions leads to the binding of nonequilibrium vacancies to form vacancy–carbon atom (or several carbon atoms) complexes.

The authors would like to thank colleagues in the group headed by Professor A. Zecca (Trento University) for assistance with the slow positron beam experiments and Dr. G. Grime for financial support of the Oxford experiments.

This work was partially financed by the Ukraine State Committee for Science and Technology, Project 07.05.04/73-93; 005K/95.

[1] N. N. Rykalin, A. A. Uglov, I. V. Zuev, and A. N Kokora, *Handbook of Laser and Electron Beam Processing of Materials* [in Russian], Mashinostroenie, Moscow (1985), p. 495.
[2] *Surface Modification and Alloying by Laser Ion and Electron Beams*, edited by J. M. Poate, G. Foti, and D. C. Jacobson (Plenum Press, New York, 1983; Mir, Moscow, 1987).
[3] A. D. Pogrebnjak, Phys. Status Solidi A **117**, 17 (1990).
[4] A. D. Pogrebnjak and D. I. Proskurovskii, Phys. Status Solidi **145**, 9 (1994).
[5] I. L. Pobol', Itogi Nauki i Tekhniki VINITI Ser. Metalloved. Term. Obrab. **24**, 99 (1990).
[6] V. I. Lavrent'ev, A. D. Pogrebnyak, and R. Shandrik, JETP Lett. **65**, 651 (1997).
[7] V. I. Lavrent'ev, Fiz. Tverd. Tela (St. Petersburg) **37**, 368 (1995) [Phys. Solid State **37**, 199 (1995)].

[8] Yu. F. Ivanov, V. I. Itin, S. V. Lykov, V. P. Rotshteĭn, and D. I. Proskurovskiĭ, Izv. Ross. Akad. Nauk Ser. Metall. No 3, 130 (1993).
[9] A. Zecca, R. S. Brusa, M. Duarte Naia, J. Paridaens, A. D. Pogrebnjak, A. B. Markov, G. E. Ozur, D. I. Proskurovskii, and V. P. Rotstein, Phys. Lett. A **175**, 443 (1993).
[10] O. G. Bakharev, A. D. Pogrebnyak, V. A. Martynenko, V. A. Rudenko, R. Brusa, A. Zekka, and A. I. Ryabchikov, Pis'ma Zh. Tekh. Fiz. **19**(1), 34 (1993) [Tech. Phys. Lett. **19**, 31 (1993)].
[11] A. D. Pogrebnyak, R. Oshner, A. Zecca, V. P. Rotshteĭn, and A. D. Mikhalev, Fiz. Khim. Obrab. Mater. **1**, 29 (1996).
[12] V. I. Lavrent'ev, Fiz. Tverd. Tela (St. Petersburg) **36**, 3563 (1994) [Phys. Solid State **36**, 1896 (1994)].
[13] M. J. Puska and R. M. Nieminen, J. Phys. F **13**, 333 (1983).
[14] I. M. Goncharenko, V. I. Itin, S. I. Isichenko, S. V. Lykov, A. B. Markov, O. I. Nalesnik, G. E. Ozur, D. I. Proskurovskiĭ, and V. P. Rotshteĭn, Zashch. Metall. **29**, 932 (1993).
[15] M. J. Puska and R. M. Nieminen, J. Phys. F **12**, L211 (1982).

Translated by R. M. Durham
Edited by David L. Book

Maximum rate of transition between boiling regimes

M. O. Lutset

S. S. Kutateladze Institute of Heat Physics, Siberian Branch of the Russian Academy of Sciences, Novosibirsk

(Submitted July 25, 1997)
Pis'ma Zh. Tekh. Fiz. **24**, 21–27 (May 12, 1998)

Similarity theory is used to study the transition from one boiling regime to another. An analysis is made of the rate of propagation of the interface between boiling regimes for a critical heat flux. © *1998 American Institute of Physics.* [S1063-7850(98)00405-4]

Liquid boiling crises are caused by a transition between boiling regimes with significantly different rates of heat exchange. As a result, the temperature of the heat-emitting surface either increases or decreases abruptly. The transition from one regime to another takes place in a finite time which is determined by the rate of propagation v of centers of the new regime and the linear scale L, which characterizes the average distance between the centers formed under the influence of variations in the flux of released heat, the heat-releasing surface, or various fluctuations. The transition time is an important parameter for the design of technical devices to prevent a crisis or which are controlled by a sharp change in temperature. Here exact results of similarity theory are used to analyze the rate of propagation of the heat-releasing interface between boiling regimes for a critical heat flux and an experimental investigation is reported.

The propagation of the heat-releasing interface between boiling regimes is controlled by the heat conduction equation with a source and suitable boundary conditions at the surface of the heater. Assuming that the heater body is sufficiently thin so that the temperature in the heater cross section perpendicular to the direction of propagation of the interface is constant, after integrating over this cross section, we obtain an equation for the temperature T per unit length of the heater:

$$SC(T)\partial T/\partial t=\nabla(S\lambda(T)\nabla T)+P(W-Q). \qquad (1)$$

Here $C(T)$ is the specific heat of the heater material calculated per unit volume, λ is its thermal conductivity, $W(T)$ and $Q(T)$ are the heat release and heat removal densities at the heater surface, and S and P are the area and the cooled perimeter of the cross section orthogonal to the direction of propagation. The analysis is confined to one-dimensional motion of the heat-releasing interface between the regimes. It is also assumed that L is fairly large so that simple boundary conditions can be set for Eq. (1). The temperature T is assumed to be a continuous function and its derivatives vanish at an infinite distance from the heat-releasing interface. The main nonlinearity in Eq. (1) is concentrated in the source $F(T)=W-Q$ which is determined by the heat exchange function $Q(T)$. From well known experiments[1,2] $Q(T)$ has the form shown in Fig. 1. Four regions with different heat exchange regimes are usually identified: natural convection (I), bubble boiling (II), transition boiling (III), and film boiling (IV). In regions (II)–(IV) the rate of heat exchange is governed by the temperature difference between the heat-releasing surface and the saturated liquid and is expressed in terms of the coefficient of heat exchange α in the form $Q(T)=\alpha(T)(T-T_s)$. Assuming that only critical effects taking place at the interfaces of the third region are considered, we shall subsequently neglect the heat transported by natural convection. The maximum heat flux q_{c1} on the heat exchange curve in the second region is usually called the first critical heat flux and the corresponding temperature T_{c1} the first critical temperature. Similarly, the second boiling crisis is achieved for the minimum heat flux in region (IV) with the coordinates q_{c2} and T_{c2}. For $q_{c2}\leqslant W\leqslant q_{c1}$ there are three homogeneous steady-state solutions of Eq. (1) which are determined by $F(T)=0$: $T=T_1$, $T=T_2$, $T=T_*$, $T_1\leqslant T_*\leqslant T_2$. Letting L tend to infinity, we can take the initial condition in the Cauchy problem for Eq. (1) in the form of a step function with values of T_1 and T_2 at $\pm\infty$. Some problems in biology and physics can be reduced to this Cauchy problem.[3–5] In the one-dimensional case, the solution of the Cauchy problem stabilizes with time and tends to a traveling-wave function $T(x,t)=T(\xi=x+vt)$ with the limiting values $T(-\infty)=T_1$, $T(+\infty)=T_2$ for the source $F(T)$ which satisfies the conditions[5]

$$F(T_1)=F(T_2)=0,\quad F(T)\leqslant 0 \text{ for } T_1<T<T_\alpha<T_2,$$

$$F(T)>0 \text{ for } T_\alpha<T<T_2, \qquad (2)$$

$$\int_{T_1}^{T_2} F\,dT\geqslant 0,\quad F(T)\leqslant 0 \text{ for } T_1<T<T_{\alpha 0}\leqslant T_\alpha,$$

$$F'(T_2)<0. \qquad (3)$$

We assume that conditions (2) and (3) are satisfied. Neglecting the stabilization time, we shall seek a solution in the form of a traveling wave $T(x,t)=T(\xi=x+vt)$ which satisfies the equation

$$d/d\xi(\lambda(T)dT/d\xi)-C(T)VdT/d\xi+F(T)/\alpha_0=0. \qquad (4)$$

Here the same notation with the subscript ''0'' is taken as the unit of measurement for λ, C, ξ, v, and α, where $\xi_0=(S\lambda_0/P\alpha_0)^{1/2}$, $v_0=v/V=(P\alpha_0\lambda_0/SC_0^2)^{1/2}$. The order of Eq. (4) can be reduced by changing the variables. Taking as

 © 1998 American Institute of Physics

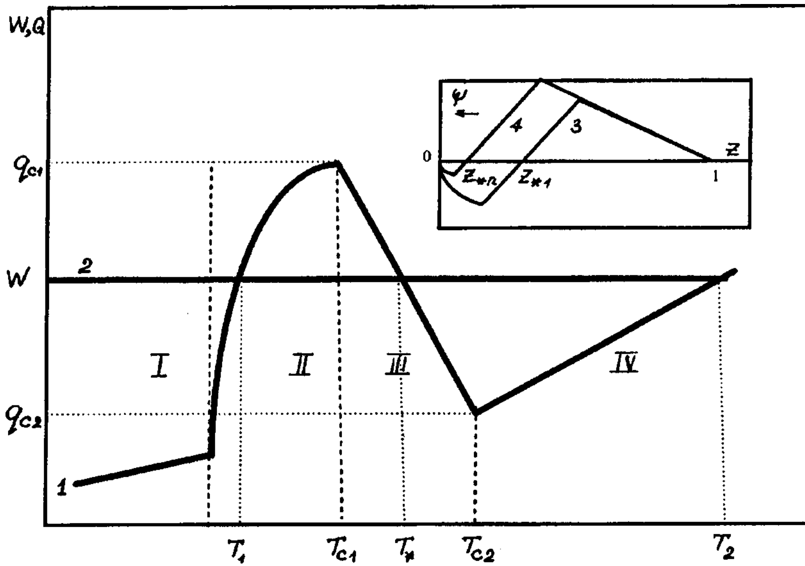

FIG. 1. Heat exchange versus heater temperature for steady-state regime and source function for constant heat release: *1* — $Q(T)$, *2* — $W(T)$. Heat exchange regimes: I — convection, II — bubble boiling, III — transition boiling, and IV — film boiling. The inset shows a fragment of $\psi(z)$ in the limiting regime $W \Rightarrow q_{c1}$, curves *3* and *4* correspond to z_{*1} and z_{*n}; $z_{*1} > z_{*n}$.

the unknown the derivative of the Kirchhoff substitution and the Goodman substitution as independent variables (see Refs. 6 and 7):

$$y = \{\lambda(T) dT/d\xi\} \Big/ \int_{T_1}^{T_2} C dT,$$

$$z = \int_{T_1}^{T} C dT \Big/ \int_{T_1}^{T_2} C dT, \tag{5}$$

we obtain an equation encountered in studies of the propagation of normal zones in a cooled current-carrying superconductor[7]

$$yy'_z - Vy + \psi(z) = 0,$$

$$\psi(z) = \lambda(z) F(z)/\alpha_0 C(z) \int_{T_1}^{T_2} C dT, \tag{6}$$

$$y(0) = y(1) = 0. \tag{7}$$

The two conditions (7) can be used to determine the solution $y(z)$ and the velocity V. These changes of variables transformed the range of temperature variation $[T_1, T_2]$ to the range of variation $z[0,1]$. It is easy to establish that for most known dependences $\lambda(T)$, $C(T)$, if $F(T)$ satisfies conditions (2) and (3), then for fairly large $W(T)$ $\psi(z)$ will also satisfy the same conditions for the range of variation $z[0,1]$. In this case, the following statements were proven in Ref. 5 for the problem (6) and (7): (*) For some $V \geqslant 0$ which can be determined uniquely, a solution of the problem (6), (7) exists uniquely and in addition $y(z) > 0$ holds for $0 < z < 1$.

Integrating Eq. (6) with allowance for Eq. (7), we have

$$V = \int_0^1 \psi dz \Big/ \int_0^1 y dz = \int_0^1 (\psi/y) dz. \tag{8}$$

It follows from Eq. (8) and the fact that y is positive that the signs of V and the integral of ψ are the same. For a negative integral of the source $F(T)$ it is sufficient to replace T with $T_2 - T$ and x with $-x$ in Eq. (1). After making this substitution, we obtain the Cauchy problem for the equation which satisfies conditions (2) and (3), where the role of T_1 and T_2 will be played by 0 and $T_2 - T_1$. Thus, the solution of the Cauchy problem stabilizes in this case, as was observed experimentally.[9–11] For negative V we shall seek a traveling-wave solution $T = T(\xi = x - vt)$ using the variable $\xi = 1 - z$ instead of z in the substitution (5). Ultimately, instead of Eq. (6), we have

$$yy'_\xi - |V|y + \chi(\zeta) = 0, \quad \chi(\zeta) = -\psi(1-\zeta),$$

$$\zeta = \int_T^{T_2} C dT \Big/ \int_{T_1}^{T_2} C dT. \tag{6'}$$

Apart from the notation, this equation is the same as Eq. (6). For fairly small $W(T)$ the integral of $\chi(\zeta)$ is positive and thus the statements (*) are valid for $V < 0$.

Then, using the qualitative theory of differential equations (see, for example, Ref. 8) we obtain information on the change in v in two limiting cases, when $W(T_1) \Rightarrow q_{c1}$ or $W(T_2) \Rightarrow q_{c2}$. Note that we cannot use the results of Refs. 3 and 4. For example, for $W(T_1) \Rightarrow q_{c1}$ we have $T_* \Rightarrow T_1$ and $F(T) \Rightarrow F_*(T)$, which is not differentiable at the point T_1, since the derivative has different limits for calculations in the regions $T_1 < T < T_*$ or $T_* < T < T_2$. Equations (6) and (6′) have three singular points in the plane (z,y) either (z,y): (0,0), $(z_*,0)$, (1,0), or (0,0), $(\zeta_*,0)$, (1,0). Let us consider Eq. (6). The roots of its characteristic equation are $\rho_{1,2}(z) = 0{,}5V \pm [0.25V^2 - \Psi'_z(z)]^{0.5}$. For $\psi'(0) < 0$ the singular point (0,0) is a saddle and the only direction of the integral curve which satisfies (*) is the positive direction $\rho_1(0)$. Similarly, the saddle point (1,0) only has the negative direction of the integral curve $\rho_2(1)$. At the third singular point $(z_*,0)$ we find $\psi'_z(z_*) \geqslant 0$. The evolution of the first crisis for the maximum thermal load takes place for $W(T_1) \Rightarrow q_{c1}$. If $\psi(z_*) = 0$ is the only solution in the range $0 < z_* < 1$, this passage to the limit is equivalent to $z_* \Rightarrow 0$. For small z_*, in accordance with Eq. (7), the integral curve enters the vicinity of the singular point $(z_*,0)$ where, if $V^2 \geqslant 4\psi'_z(z_*)$, then $(z_*,0)$ is a node and $y(z_*) = 0$, which is impossible according to the statement (*). Thus, we have $V^2 < 4\psi'_z(z_*)$ and

there is a focus at the point $(z_*,0)$. We construct the descending sequence $z_{*i}\Rightarrow 0$ for $i\Rightarrow\infty$. According to the statement (*), each value of z_{*i} corresponds to a value of V_i where $0\leqslant V_i<4\psi_z'(z_{*i})$. Suppose that $\lim V_i=V_{(1)}$. Going to the limit, we have

$$0\leqslant V_{(1)}\leqslant 2\sqrt{\psi_z'(+0)}. \tag{9}$$

Equality can be achieved at the upper boundary $V_{(1)}$ if condition (7) is satisfied. It was shown in Ref. 7 that for a convex limit function $\psi(z)$, $V_{(1)}$ in the limit attains a bifurcation value of the velocity $2\sqrt{\psi_z'(+0)}$ with an infinite derivative of $V_{(1)}$ with respect to z_*. Similarly, considering $W(T_2)\Rightarrow q_{c2}$, we obtain for the limiting negative velocity $V_{(2}$:

$$0\leqslant -V_{(2)}\leqslant 2\sqrt{\chi_\zeta'(+0)}, \tag{10}$$

where a bifurcation value is achieved with an infinite derivative of $V_{(2)}$ with respect to ζ_* for the convex limit function $\chi(\zeta)$. If there is a smooth transition at the boundaries of region III rather than a kink of $Q(T)$, the limiting bifurcation values are zero. Going to the limit in this case, we obtain from Eqs. (9) and (10) that either $V_{(1)}$ or $V_{(2)}$ tends to zero, which implies degenerate boiling crises, i.e., a smooth transition from one regime to another controlled by a change in the heat release. Similar degeneracy was observed experimentally.[11] Generally, we can make the bifurcation value of the velocity go to zero by selecting $F(T)$, i.e., nuclei of the new regime can be stabilized as far as the limiting heat fluxes by controlling the thermal load. Thus, in the limiting cases, the rate of propagation of the heat-releasing interface between boiling regimes is determined by a narrow region of transition boiling q_{c1}, q_{c2}. This influence severely limits the freedom of modeling the heat exchange in region III. However, no experimental data are available on the structure of $Q(T)$ near the points (q_{c1}, T_{c1}) and (q_{c2}, T_{c2}) for the moving interface between boiling regimes. In our view, this problem may be solved by means of an experimental investigation which is planned for the very near future.

The author would like to thank V. Yu. Chekhovich and A. N. Pavlenko for discussions.

This work was carried out as part of the Russian Fund for Fundamental Research Project No. 96-02-19401.

[1] R. F. Gertner, Teploperedacha No. 1, 20 (1965) [Translation of R. F. Gaertner, Trans. ASME C **87**, No. 1]

[2] S. S. Kutateladze, *Fundamentals of Heat Transfer*, Nauka, Novosibirsk (1970); 2nd ed. transl. Academic Press, New York (1963).

[3] A. N. Kolmogorov, I. G. Petrovskiĭ, and N. S. Piskunov, Byul. Mosk. Gos. Univ. A **1**, 1 (1937).

[4] Ya. B. Zel'dovich, Zh. Fiz. Khim. **22**, 27 (1948).

[5] Ya. I. Kanel', Mat. Sborn. **59**, Suppl., 245 (1962).

[6] L. A. Kozdoba, *Methods of Solution for Nonlinear Heat Conduction Problems* [in Russian], Moscow (1975), 227 pp.

[7] Yu. M. L'vovskiĭ, Zh. Tekh. Fiz. **54**, 1663 (1984) [Sov. Phys. Tech. Phys. **29**, 1984 (1984)].

[8] S. Lefschetz, *Differential Equations: Geometric Theory*, 2nd ed. (Interscience, New York, 1963 [Russ. transl. of 1st ed., IL, Moscow 1961, 387 pp.].

[9] S. A. Zukov, V. V. Barelko, and A. G. Merzhanov, Int. J. Heat Mass Transf. **24**, 47 (1980).

[10] A. N. Pavlenko, V. Yu. Chechovich, and I. P. Starodubtseva, Russ. J. Eng. Thermophys. **4**, 323 (1994).

[11] B. I. Verkin, Yu. A. Kirichenko, N. M. Levchenko, and K. V. Rusanov, Cryogenics No. **1,** 49 (1979).

Translated by R. M. Durham
Edited by David L. Book

Dynamic recrystallization in a near-eutectic Pb–Sn–Ag alloy under thermal cycling

S. A. Atroshenko, D. R. Lyu, and I. Sh. Pao

Institute of Problems in Mechanical Engineering, Russian Academy of Sciences, St. Petersburg; Ford Research Laboratory, Detroit

(Submitted October 10, 1997)
Pis'ma Zh. Tekh. Fiz. **24**, 28–31 (May 12, 1998)

An analysis is made of the behavior of solders under thermal cycling. Dynamic recrystallization can be used to explain the evolution of the microstructure of soldered joints during operation. © *1998 American Institute of Physics.* [S1063-7850(98)00505-9]

The reliability of soldered joints in electronic circuits is an important factor. Solders undergo cyclic strain caused by thermal cycling of the circuits during operation and created by the large difference between the coefficients of thermal expansion of the components. The thermal changes take place at high homologous temperatures for these alloys, which may lead to dynamic recrystallization.

Experiments were carried out to study the evolution of the solder microstructure. The material used for the study was an alloy containing 62% Sn, 36% Pb, and 2% Ag. The soldered joints were subjected to cycling between −40 and 100 °C (air–air) with a 5 min pause and 25 min holding time. After every 250 cycles, the circuits were removed from the thermal chamber and the samples were cut into polished sections to assess the change in the microstructure using optical and scanning electron microscopy and an image analyzer. The evolution of the microstructure and damage to the solders was examined from transverse polished microsections using a Nikon optical microscope and a JSM 840A scanning electron microscope. The microstructure dimensions were measured using an image analyzer. The image analyzer was a Nikon microscope connected to an Image-Pro Plus computer program which can automatically calculate various parameters of the microstructure such as the area, perimeter, diameter, and so on, which can be represented numerically, statistically, or graphically.

Figure 1 gives the grain size d of the lead phase as a function of the number of thermal cycles N. It can be seen that the dependence is nonmonotonic with a maximum observed for 500 thermal cycles. Figure 2 shows photographs of the microstructure in the initial state and after thermal cycling. It can be seen that after 250 thermal cycles, the size of the lead phase (unshaded) is slightly reduced, after 500 cycles it increases, then decreases up to 750 cycles, and begins to increase again. After 250 cycles the structure exhibits porosity and after 500 cycles microcracks begin to appear. After 750 cycles the large grains break down into smaller ones and after 1000 cycles fairly large cracks are observed. In general, the behavior of the microstructure reflects the dependence of the grain size on the number of thermal cycles.

Dynamic recrystallization is an efficient mechanism for local rearrangement of the microstructure in many metals. It reduces the grain size at high strain rates and moderately high temperature and also leads to grain growth at strain rates below 10 s^{-1}, particularly when the deformation takes place at relatively high temperatures.[1,2]

These conditions are usually associated with superplasticity: a temperature around half the absolute melting point (or above), diffusion-controlled structural changes induced by strain, or as a possible alternative, a fine-grained structure.[3] Some superplastic alloys are resistant to static re-

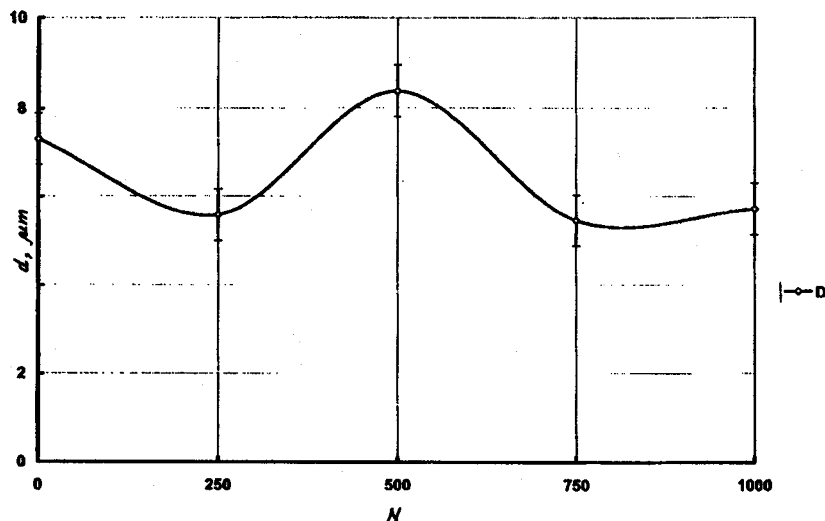

FIG. 1. Grain size of lead phase versus number of thermal cycles.

 © 1998 American Institute of Physics

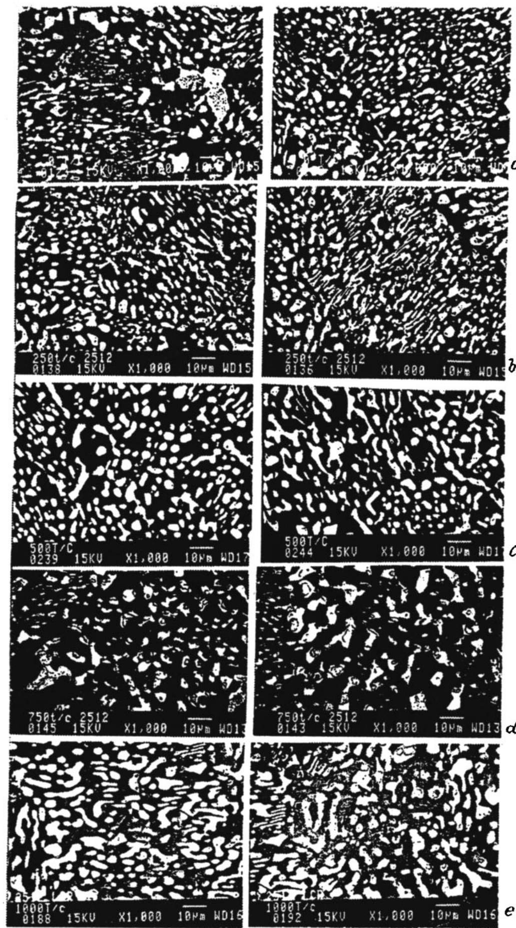

FIG. 2. Microstructure of 62Sn–36Pb–2Ag alloy in initial state (a) and after thermal cycling for 250 (b), 500 (c), 750 (d), and 1000 (e) cycles.

crystallization and undergo dynamic recrystallization.[4] Superplasticity was observed in Pb–Sn alloys under high-temperature strain (20–170 °C) at strain rates of 10^7–10^2 s^{-1} over a wide range of grain sizes.[5] Since even 25 °C is a high homologous temperature for a solder, dynamic recrystallization may take place, since the metal is in the strained state.

Eutectic solders have been extensively studied because of their widespread application in electronic devices. This is the first attempt to explain the evolution of the microstructure of these alloys on the basis of dynamic recrystallization. The behavior of eutectics varies substantially as a function of their morphology. Soldered joints undergo heterogeneous strain. Shear strains are concentrated at sites of structural coarseness. The accumulated strains lead to cracking at these sites and the joint ultimately ruptures. An understanding and simulation of the microstructure evolution using the experimentally determined parameters can improve the operating life of electronic joints.

[1] T. Sakai and J. J. Jonas, Acta Metall. **32**, 189 (1984).
[2] J. J. Jonas, Mater. Sci. Eng., A **184**, 155 (1994).
[3] A. H. Chokshi and M. A. Meyers, Scripta Metall. **24**, 605 (1990).
[4] F. J. Humphreys and M. Hatherly, *Recrystallization and Related Annealing Phenomena* (Pergamon Press, Oxford, 1995).
[5] B. P. Kashyap and G. S. Murty, Mater. Sci. Eng. **50**, 205 (1981).

Translated by R. M. Durham
Edited by David L. Book

Alternation of nonequilibrium carrier states in *n*-GaAs

P. N. Gorleĭ, P. P. Gorleĭ, and P. M. Tomchuk

Chernovtsy State University;
Institute of Physics, Ukrainian National Academy of Sciences, Kiev
(Submitted July 24, 1997)
Pis'ma Zh. Tekh. Fiz. **24**, 32–37 (May 12, 1998)

Numerical methods are used to demonstrate the alternation between stable and chaotic states of a time-dependent system of nonequilibrium carriers in a semiconductor with parameters similar to n-GaAs, under conditions suitable for the Gunn effect to occur. Changes in the quantitative characteristics of evolution of the phase variables (maximum Lyapunov exponent and Hausdorff dimension) are also studied as a function of the external field. © *1998 American Institute of Physics.* [S1063-7850(98)00605-3]

Self-organization and dynamic chaos effects in semiconductors in strong electric fields in the presence of various types of nonlinearities have recently been actively studied (see, for example, Refs. 1 and 2). In particular, a similar problem was studied experimentally for semi-insulating GaAs in Ref. 3 and theoretically for n-GaAs in Ref. 4, where numerical methods were used to demonstrate the transition from current oscillations to a chaotic state of the electronic system in a semiconductor subject to the Gunn effect. However, these studies did not consider the scenario for this transition and its characteristics such as the transformation of the phase portrait, the dependence of the Hausdorff dimension on the control parameter, and other factors. A knowledge of this behavior would provide a better understanding of the physics of nonequilibrium processes and would allow recommendations to be proposed as to possible methods of controlling these processes.

Here we examine this problem.

We shall take as our starting point the one-dimensional field model of the Gunn effect in semiconductors. In the presence of an ac electric field $E(x,t)$, the corresponding equation for an n-type semiconductor has the form[4]

$$\frac{\partial E}{\partial t}=D\frac{\partial^2 E}{\partial x^2}+v(E)\frac{\partial E}{\partial x}-\frac{en_0}{\varepsilon\varepsilon_0}v(E)+\frac{j_0(t)}{\varepsilon\varepsilon_0}. \quad (1)$$

Here n_0 is the equilibrium electron concentration, D is the diffusion coefficient, which does not depend on the coordinate or the electric field, e is the absolute electron charge, ε_0 and ε are the static permittivities of vacuum and the semiconductor material, respectively, and $j_0(t)$ is the integration constant. The dependence of the carrier drift velocity on the electric field $v(E)$ is usually described by the following formula:[5]

$$v(E)=\frac{u_1E+v_s(E/E_a)^\gamma}{1+(E/E_a)^\gamma}, \quad (2)$$

where u_1 is the carrier drift velocity in weak electric fields, and v_sE_a and γ are adjustable parameters.

Using a standard method, we seek a solution of Eq. (1) as a Fourier series expansion of $E(x,t)$ near the uniform electric field distribution $E_0(t)$ along the sample:[4]

$$E(x,t)=E_0(t)+\sum_{m\neq 0}E_m(t)\exp(imk_0x). \quad (3)$$

Here $E_m(t)=E_{mr}(t)+iE_{mi}(t)$ is the complex amplitude of the mth harmonic of the oscillations, $k_0=2\pi/L$, where L is the characteristic wavelength in the crystal, which is a parameter of the problem. Confining ourselves in Eq. (3) to $m=\pm 1,\pm 2$ and converting to the dimensionless variables $y_1=E_{1r}/E_0$, $y_2=E_{1i}/E_0$, $y_3=E_{2r}/E_0$, $y_4=E_{2i}/E_0$, $x=\omega_0 t$, Eq. (1) can be rewritten as the system

$$\frac{\partial y_i}{\partial x}=a_iy_i+c_iB_i+b_i\sum_{s=2}^{4}\frac{1}{s!}A_{si}\Psi_s \quad (i=1,2,3,4). \quad (4)$$

Here ω_0 is the characteristic oscillation frequency in the crystal, a_i, b_i, and c_i are dimensionless quantities which depend on the parameters of the problem, A_{si} and B are complicated nonlinear functions of y_i, and

$$\Psi_s(\gamma,E_0/E_s,v_s/u_1E_a)=\frac{E_0^{s-1}}{u_1}\frac{\partial^s v}{\partial E^s}\bigg|_{E=E_0} \quad (5)$$

is also a complex function of its parameters. Because of their cumbersome nature, these functions cannot be given here.

The strength of the external electric field was taken as the control parameter. The system (4) was solved for the parameters of n-GaAs given in Ref. 4. In this case, unlike Ref. 4, the carrier drift velocity $v(E)$ was expanded as a Maclaurin series up to and including the fourth power of the deviation $\Delta E=E(x,t)-E_0(t)$.

 © 1998 American Institute of Physics

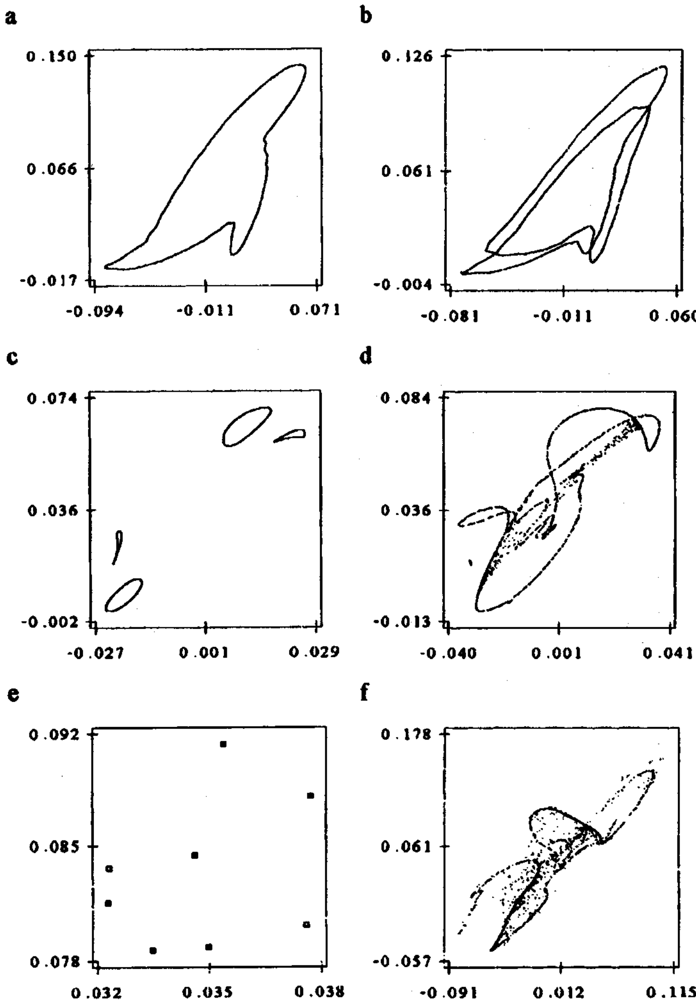

FIG. 1. Evolution of the phase portrait projected on the y_2y_4 plane and values of its numerical characteristics as a function of the control parameter E_0: a — $E_0=4.12578\times10^5$ V/m, $\lambda=0.6$, $D_H=2.07$; b — $E_0=4.12728\times10^5$ V/m, $\lambda=0.65$, $D_H=2.26$; c — $E_0=4.1316\times10^5$ V/m, $\lambda=-0.2134$, $D_H=1.62$; d — $E_0=4.13298\times10^5$ V/m, $\lambda=10.21$, $D_H=2.25$; e — $E_0=4.1361\times10^5$ V/m, $\lambda=-0.5309$, $D_H=1.0$; f — $E_0=4.13916\times10^5$ V/m, $\lambda=28.44$, $D_H=2.49$.

In the steady state $\partial y_i/\partial x=0$, in addition to the trivial solution $y_i=0$, the system of equations (4) has solutions which cannot be determined analytically. It is found that to analyze the states of such a system, it is sufficient to restrict attention to a cross section of regions of possible solutions of Eqs. (4), for example, in the plane $y_1=y_2=0$. If $\Psi_4=0$ is also assumed, the solutions of Eqs. (4) will be

$$\begin{cases} Y_3=\pm y_4, \\ y_4=\pm\{-4a[1\pm(b/a\Psi_1+d)]/(\Psi_2\pm b\Psi_3)\}^{1/2}, \end{cases} \quad (6)$$

where a, b, and d are coefficients which depend on the parameters of the problem.

It follows from (6) that subject to the assumptions made, the system can have four or eight nontrivial solutions or none at all, depending on the ratio between the parameters of the problem. In all probability, the authors of Ref. 4 investigated that range of parameters for which there are no additional steady-state solutions of system (4). In the four-dimensional solution space $y_i\neq0$, the set of possible solutions of system (4) can only be greater than the case studied.

A numerical integration of system (4) was performed by the fourth-order Runge–Kutta method while the maximum Lyapunov exponent λ and the Hausdorff dimension D_H were calculated using a procedure developed in Ref. 2.

These results showed that variation of the external electric field E_0 as the control parameter in a small range between 4.11×10^5 and 4.14×10^5 V/m appreciably transforms the phase portraits of the system (Fig. 1) and their numerical characteristics (Fig. 2).

It is found that the transformation of the states of the nonsteady system begins with a transition from the equilibrium focus ($E_0<4.11204\times10^5$ V/m, $D_H=0$, $\lambda<0$) to the limit cycle (Fig. 1a) and then, by means of period doubling (Fig. 1b), leads to the formation of four new limit cycles (Fig. 1c). A further increase in the control parameter increases the linear dimensions of the limit cycles, causing them to initially merge in pairs and then form a randomized structure—a strange attractor (Fig. 1d). The strange attractor is then abruptly destroyed, and this is followed by the formation of a stable system first with one, then with two, four, and eight discrete states (Fig. 1e), which is consistent with the analysis of system (4) described above. A further increase in the control parameter is accompanied by rapid randomization of the system (Fig. 1f) after which it becomes generally incompatible.

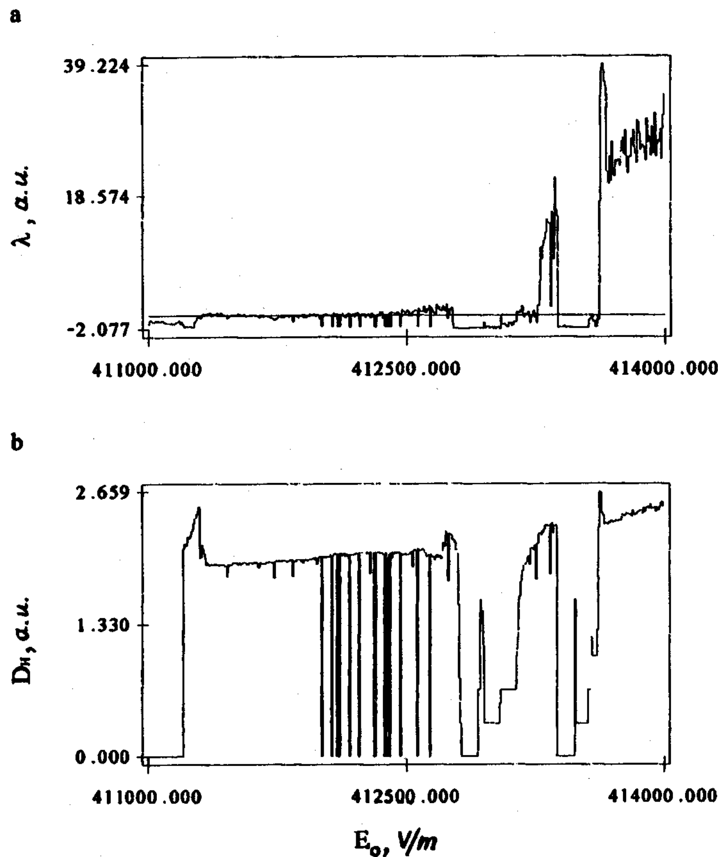

FIG. 2. Evolution of the numerical characteristics of the phase portrait as a function of the control parameter E_0: a — maximum Lyapunov exponent and b — Hausdorff dimension.

The results of these investigations have shown for the first time that in the presence of the Gunn effect, a time-dependent system of nonequilibrium carriers in a semiconductor having the parameters of n-GaAs is characterized by complex dynamics of alternating state transitions. It can also be seen from Fig. 2 that ranges of values of the control parameter for which the system is stable (when $\lambda > 0$) exist and may be used for practical applications.

This work was partially financed by the Ukraine Ministry of Science and Technology (Grant No. 2.4/745).

[1] A. G. Deryagin, V. I. Kuchinskiĭ, and G. S. Sokolovskiĭ, Pis'ma Zh. Tekh. Fiz. **22**(7), 44 (1996) [Tech. Phys. Lett. **22**, 286 (1996)].
[2] P. N. Gorley, P. P. Horley, and P. M. Tomchuk, Pis'ma Zh. Tekh. Fiz. **22**(20), 82 (1996) [Tech. Phys. Lett. **22**, 857 (1996)].
[3] F. Piazza, P. C. M. Christianen, and J. C. Maan, Acta Phys. Pol. A **88**, 865 (1995).
[4] J. Zongfu and M. Benkun, Phys. Rev. B **44**, 11072 (1991).
[5] M. I. D'yakonov, M. E. Levinshteĭn, and G. S. Simin, Fiz. Tekh. Poluprovodn. **15** (11), 2116 (1981) [Sov. Phys. Semicond. **15**, 1229 (1981)].

Translated by R. M. Durham
Edited by David L. Book

Electron dynamics during laser neutralization of negative ions

A. R. Karimov

Institute of High Temperatures, Russian Academy of Sciences, Moscow
(Submitted July 17, 1997)
Pis'ma Zh. Tekh. Fiz. **24**, 38–42 (May 12, 1998)

A hydrodynamic approach is used to study the electron dynamics when laser radiation acts on a negative ion beam. An analytic solution of the problem is obtained. © *1998 American Institute of Physics.* [S1063-7850(98)00705-8]

Atomic fluxes may be obtained by photoionization of negative ion beams.[1–4] The divergence of the neutral beam is specifically caused by the action of the ion beam space charge whose magnitude is determined by the photoionization rate and the drift of electrons from the bulk of the beam. The product electrons can initiate an optical discharge in the beam and the negative ions may be converted into atoms and positive ions. In order to allow for these effects, an analysis is made of the electron dynamics when laser radiation acts on a negative ion beam.

The transverse electron motion relative to the beam in a two-dimensional geometry is analyzed, neglecting the transverse motion of the ions. The electron drift allowing for photoionization in an electromagnetic field of frequency ω and intensity I under the action of the self-induced Coulomb field of the beam E is described by

$$\frac{\partial n_e}{\partial t}+\frac{\partial(n_e u_e)}{\partial x}=\frac{n_b}{\tau_{\mathrm{ph}}}, \tag{1}$$

$$\frac{\partial u_e}{\partial t}+u_e\frac{\partial u_e}{\partial x}=-\frac{e}{m_e}E, \tag{2}$$

$$\frac{\partial E}{\partial x}=-4\pi e(n_e+n_b), \tag{3}$$

$$\frac{dn_b}{dt}=-\frac{n_b}{\tau_{\mathrm{ph}}}, \tag{4}$$

where n_e and u_e are the electron density and velocity, n_b is the ion density, e is the ion and electron charge, m_e is the electron mass, $\tau_{\mathrm{ph}}^{-1}=\sigma_{\mathrm{ph}}I/\hbar\omega$, and σ_{ph} is the photoionization cross section.

In Eqs. (1)–(4), we go over from the densities to the total number of particles:

$$N_s(x,t)=\int_0^x n_s(\zeta,t)d\zeta, s=e,b. \tag{5}$$

Equation (4) then gives

$$N_b=N_{b0}\exp(-t/\tau_{\mathrm{ph}}). \tag{6}$$

If the density distribution over the beam cross section is uniform we have

$$N_{b0}=xn_0,$$

where n_0 is the initial ion density in the beam. Equations (1)–(3) in terms of the Lagrangian variables[5]

$$\tau=t,\quad \xi=x-\int_0^t u_e(\xi,t')dt', \tag{7}$$

where $x(\xi,t)$ satisfies the initial condition

$$x(\xi,0)=\xi,$$

reduce to

$$\frac{\partial N_e}{\partial\tau}=\frac{N_b}{\tau_{\mathrm{ph}}}, \tag{8}$$

$$\frac{\partial u_e}{\partial\tau}=\frac{4\pi e^2}{m_e}(N_e+N_b). \tag{9}$$

Differentiating Eq. (9) with respect to τ, using Eqs. (6), (8), and

$$u_e=\frac{\partial x}{\partial\tau}, \tag{10}$$

we obtain

$$\frac{\partial^2 u_e}{\partial\tau^2}=\frac{u_e}{\tau_b^2}\exp(-\tau/\tau_{\mathrm{ph}}), \tag{11}$$

where $\tau_b^{-1}=4\pi e^2 n_0/m_e$. The general solution of Eq. (11) may be written in the form

$$u_e=A(\xi)\exp\left[-\frac{\sqrt{2}\tau_{\mathrm{ph}}e^{-\tau/2\tau_{\mathrm{ph}}}}{\tau_b}\right]+B(\xi)\exp\left[\frac{\sqrt{2}\tau_{\mathrm{ph}}e^{-\tau/2\tau_{\mathrm{ph}}}}{\tau_b}\right]. \tag{12}$$

The solution (12) for $\tau_{\mathrm{ph}}\gg\tau$ should differ little from the accurate solution of Eqs. (1)–(4), which corresponds to $\tau_{\mathrm{ph}}=\infty$. We use this observation to determine the form of the constants $A(\xi)$ and $B(\xi)$. The accurate solution of Eqs. (1)–(4) for $\tau_{\mathrm{ph}}=\infty$ is

$$u_e=U_0(\xi)+\frac{\xi\tau}{\tau_b^2}. \tag{13}$$

Confining ourselves to linear terms in the expansion of the exponential function in terms of the small parameter τ/τ_{ph} (12), we obtain

 © 1998 American Institute of Physics

$$u_e = A_e^{-\sqrt{2}\tau_{ph}/\tau_b} + Be^{\sqrt{2}\tau_{ph}/\tau_b} + \frac{\tau}{\sqrt{2}\tau_b} \times [A_e^{-\sqrt{2}\tau_{ph}/\tau_b} - Be^{\sqrt{2}\tau_{ph}/\tau_b}] + \dots \quad (14)$$

We shall assume that the initial velocity distribution is

$U_0(\xi) = 0.$

Then, equating terms with the same powers of τ in Eqs. (13) and (14), we have

$$A = \frac{\xi}{\sqrt{2}\tau_b} e^{\sqrt{2}\tau_{ph}/\tau_b}, \quad B = -\frac{\xi}{\sqrt{2}\tau_b} e^{-\sqrt{2}\tau_{ph}/\tau_b},$$

so that Eq. (12) can be written as

$$u_e = \frac{\xi}{\sqrt{2}\tau_b}\left[\exp\left(\frac{\tau}{\sqrt{2}\tau_b}\right) - \exp\left(-\frac{\tau}{\sqrt{2}\tau_b}\right)\right]. \quad (15)$$

For $\tau > \tau_b$ the second term in Eq. (15) may be neglected. The approximate value of the coordinate $x(\tau,\xi)$ then has the form

$$x(\tau,\xi) = \xi \exp\left(\frac{\tau}{\sqrt{2}\tau_b}\right), \quad (16)$$

so that the solution (8) assuming $N_e(\tau=0,\xi)=0$ can then be written as

$$N_e = \frac{\sqrt{2}n_0\tau_b}{\tau_{ph} - \sqrt{2}\tau_b}\left[\exp\left(\frac{\tau_{ph} - \sqrt{2}\tau_b}{\sqrt{2}\tau_b\tau_{ph}}\tau\right) - 1\right]. \quad (17)$$

From

$$n_e = \frac{\partial N_e}{\partial \xi}\left[\frac{\partial x}{\partial \xi}\right]^{-1}$$

and Eqs. (16) and (17) we then obtain

$$n_e = \frac{\sqrt{2}n_0\tau_b}{\tau_{ph} - \sqrt{2}\tau_b}\left[\exp\left(-\frac{\tau}{\tau_{ph}}\right) - \exp\left(-\frac{\tau}{\sqrt{2}\tau_b}\right)\right]. \quad (18)$$

Equations (16) and (18) describe the production and space-time distribution of electrons when the negative ions undergo photoionization.

In particular, we can then obtain the necessary condition for the evolution of an optical discharge in a negative ion beam. Equation (16) can be used to find the characteristic electron residence time in the bulk of a beam having the transverse dimension $2b$:

$$\tau_{in} = \sqrt{2}\tau_b \ln\left(\frac{b}{\xi}\right). \quad (19)$$

Equation (18) can be used to obtain the time at which n_e reaches a maximum:

$$\tau_e = \frac{\sqrt{2}\tau_b\tau_{ph}}{\tau_{ph} - \sqrt{2}\tau_b}\ln\left(\frac{\tau_{ph}}{\sqrt{2}\tau_b}\right). \quad (20)$$

Favorable conditions for the evolution of a discharge are evidently established when $\tau_e \leqslant \tau_{in}$ holds, which will be achieved for

$$\frac{\tau_{ph}}{\tau_{ph} - \sqrt{2}\tau_b}\ln\left(\frac{\tau_{ph}}{\sqrt{2}\tau_b}\right) \leqslant \ln\left(\frac{b}{\xi}\right). \quad (21)$$

This relation defines the system parameters for which an optical discharge may develop.

[1] A. Y. Wong, J. M. Dawson, W. Gekelman, and Z. Lucky, Appl. Phys. Lett. **25**, 57 (1974).

[2] J. H. Fink, W. L. Barr, and G. W. Hamilton, IEEE Trans. Plasma Sci. **PS-7**, 21 (1979).

[3] J. H. Fink, in *Proceedings of the Third International Symposium on the Production and Neutralization of Negative Ions and Beams* (AIP Press, New York, 1983), p. 347.

[4] A. R. Karimov and A. A. Postel'nikov, Pis'ma Zh. Tekh. Fiz. **18**(7), 50 (1992) [Sov. Tech. Phys. Lett. **18**, 225 (1992)].

[5] Ch. Sack and H. Schamel, Phys. Rep. **156**, 313 (1987).

Translated by R. M. Durham

Edited by David L. Book

New channels for mechanical twinning

V. S. Savenko

Mozyr State Pedagogical Institute
(Submitted August 27, 1997)
Pis'ma Zh. Tekh. Fiz. **24**, 43–49 (May 12, 1998)

The creation of twins at twinning wedge boundaries in bismuth single crystals whose surface is deformed by a concentrated load, has been observed and explained for the first time.
© *1998 American Institute of Physics.* [S1063-7850(98)00805-2]

Although twinning is one of the main types of deformation in crystals, unlike glide, this type of plastic deformation has not been studied in detail. This is evidenced by the very small number of publications concerned with twinning. However, experimental investigations of twinning suggest that such studies are desirable, as has been confirmed by discoveries of new phenomena accompanying this type of plastic deformation. In Refs. 1–3, for example, it was established that dislocation processes accompanying crystal twinning are intensified when high-density electric current pulses (of the order of hundreds of amperes per square millimeter) are passed through the crystals. In Ref. 4 twinning of bismuth single crystals was investigated when superposed electric and magnetic fields were applied to the sample. It was observed that the twinned volume of material was increased appreciably compared with that when the twinning plastic deformation process takes place in the absence of any external energy influences. This suggests that in principle, it may be possible to control plastic deformation by twinning under conditions where external energy influences are applied.

In the present study it was observed that intensive stimulation of dislocation processes accompanying crystal twinning by external energy influences and also in some cases, without these influences, leads to the establishment of new channels for plastic deformation of crystals by twinning which is observed as ''twin branching.''

When the (111) cleavage plane of a bismuth single crystal is deformed by a concentrated load, which usually[1–4] takes the form of the diamond pyramid of a standard PMT-3 microhardness meter, it is comparatively easy to obtain an ensemble of wedge-shaped twins of the form $\{101\}\langle 001\rangle$ (Fig. 1) consisting of between five and eight twins, which are usually created at dislocation pile-ups. Twinning was investigated by means of electron microscopy.

It was shown in Refs. 5 and 6 that internal stresses only relax as a result of the evolution of glide, for example, in regions of the crystal adjacent to twinning boundaries. However, it was observed in the present study that internal stresses in bismuth single crystals deformed by a concentrated load can relax as a result of the formation and evolution of twins. Moreover, the twins are formed not only at pile-ups of complete dislocations but also at interfaces between twinning layers, i.e., at pile-ups of twinning dislocations (Figs. 1–3).

In the absence of external energy influences, ''branching'' twins are frequently created at twinning boundaries with a low degree of coherence (Fig. 1). Curving of twinning boundaries is caused by an excess concentration of twinning dislocations at these boundaries. An enhanced density of dislocations at a twinning boundary has the result that the internal stresses created by the twinning dislocations become localized at this boundary. In this event, stresses comparable to

FIG. 1. Formation of a twin at a twinning boundary with a low degree of coherence.

 © 1998 American Institute of Physics

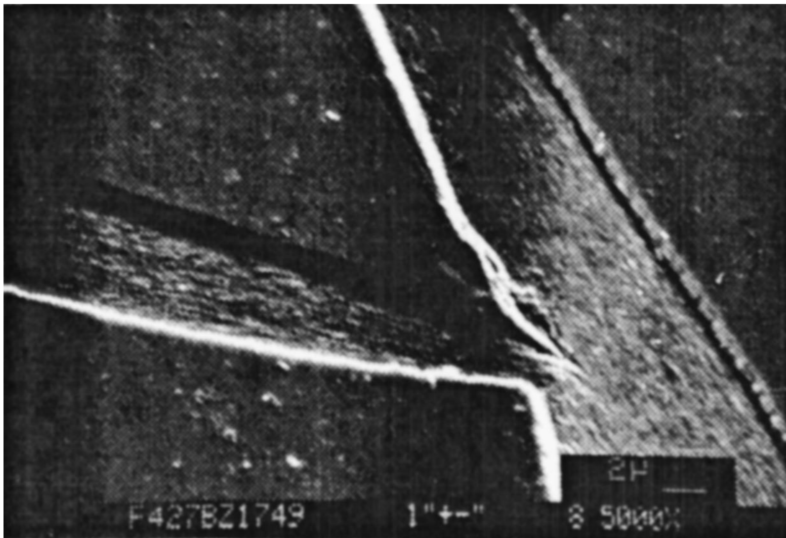

FIG. 2. Twin branching at an obstacle.

the threshold for the formation of a wedge-shaped twin may be created at dislocation pile-up sites. These stresses relax by creating a new twin at the twinning boundary, which develops in a new energetically favored direction (Fig. 1).

Note that in a bismuth single crystal whose (111) cleavage plane is deformed by a concentrated load, twins may develop in three directions [101], $[\bar{1}01]$, and $[10\bar{1}]$ (Schmidt factor 0.48). Thus, if the ''parent'' twin evolves in the [101] direction, the ''daughter'' twin can only develop in the $[\bar{1}01]$ or $[10\bar{1}]$ direction.

An excess concentration of partial twinning dislocations at certain sections of twinning boundaries may be caused by obstacles in the form of structural irregularities in the crystal lattice or a pile-up of complete dislocations (Fig. 2). In this last case, the ''daughter twin'' may be formed as a result of splitting of complete dislocations into partial twinning ones.

Figure 3 shows the case where branching of a twin was caused by an obstacle in the translational path of the twinning dislocations. This is evidenced by the blunt shape of the twin tip. To explain this case, we use the stress field pattern near a wedge-shaped twin (Fig. 4) which was obtained assuming that the twinning boundary consists of complete[7–9] rather than partial dislocations. The stress field around a wedge-shaped pile-up of these dislocations may be calculated using the formula:

$$\sigma_{xy}=\frac{Gb}{2\pi(1-\nu)}\left\{\sum_{n=0}^{N_1}\frac{(x+nd)[(x+nd)^2-(y+nh)^2]}{[(x+nd)^2+(y+nh)^2]^2}+\sum_{n=1}^{N_2}\frac{(x+nd)[(x+nd)^2-(y-nh)^2]}{[(x+nd)^2+(y-nh)^2]^2}\right\}, \tag{1}$$

where σ_{xy} are the cleavage stresses,[10] b is the magnitude of the Burgers vector, G is the shear modulus, ν is the Poisson ratio, n is the summation index, and N_1 and N_2 are the numbers of dislocations at the twinning boundaries. In our case, it was assumed that $N_2=N_1=10$ to obtain the computer plot of the curves shown in Fig. 4.

It can be seen from Fig. 4 that the stresses increase with increasing proximity to the twinning boundary, and at the tip of the twin they are of the same order of magnitude as those in the immediate vicinity of the twinning boundary, but at a

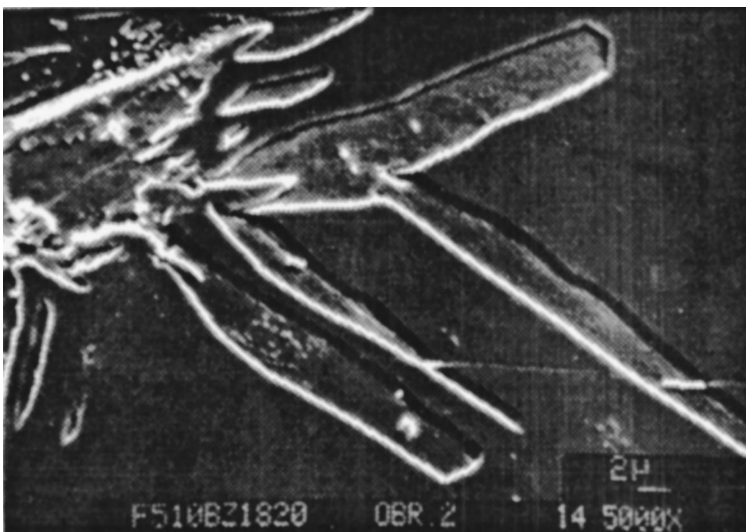

FIG. 3. Twin branching caused by an obstacle in the translation path of twinning dislocations.

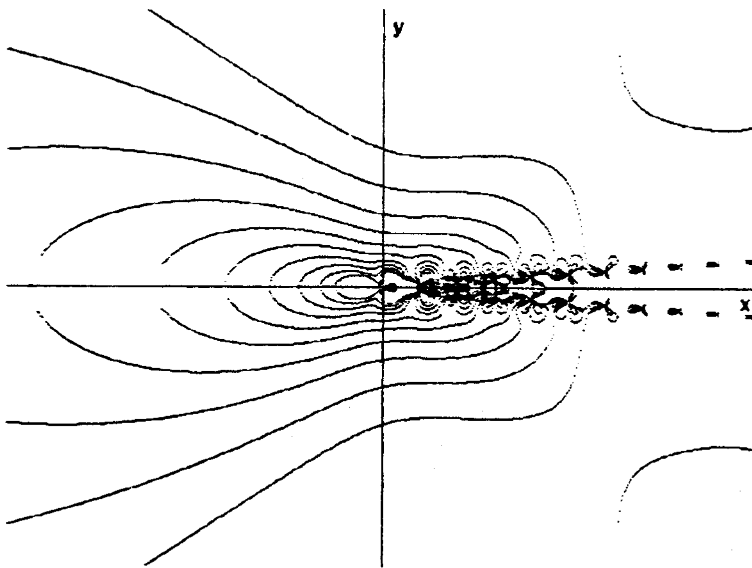

FIG. 4. Stress field at a wedge-shaped twin.

distance two or three orders of magnitude greater. As a result, when obstacles are present in the path of the wedge-shaped twin, the stresses at its tip become redistributed so that their projections on the new twinning direction are comparable with the threshold for the formation of a twin.

Dislocation processes accompanying twinning may be stimulated by passing electric current pulses through crystals.[1–5] As the pulse current density increases, the processes involved in the generation of twinning dislocations are intensified. In this case, a group of twinning dislocations migrating along twinning boundaries may not only interact with an obstacle to form a new twin but may also overcome the resistance of the stopped dislocations to form a second tip.

The stimulation of twin branching by electric current pulses can also be attributed to the increased internal stresses in the crystal as a result of the pinch effect. The appearance of additional stresses in the crystal increases the probability of a second twin tip being formed.

To sum up, electron microscopy and computer construction of the stress fields around a wedge-shaped twin have been used to establish that the internal stresses in bismuth single crystals may relax by twinning as a result of twin branching. In this case, a new twin tip is created at partial twinning dislocations rather than at complete dislocations.

I would like to thank O. M. Ostrikov for his interest in this work, for calculations of the stress fields at a wedge-shaped twin, and for discussions of the results.

[1] V. S. Savenko and M. S. Tsedrik, Izv. Akad. Nauk BSSR Ser. Fiz.-Mat. Nauk No. 1, 105 (1980).
[2] V. I. Bashmakov and V. S. Savenko, Izv. Vyssh. Uchebn. Zaved. Fiz. No. **7,** 29 (1980).
[3] V. S. Savenko, in *Physical Properties of Gases and Solids* [in Russian], Minsk (1978), pp. 129–135.
[4] V. S. Savenko, A. I. Pinchuk, V. V. Ponaryadov, and V. B. Zlotnik, Vestn. BGU Ser. 1. No. 2, 27 (1995).
[5] V. S. Savenko, V. I. Spitsyn, and O. A. Troitskiĭ, Dokl. Akad. Nauk SSSR **283**, 1181 (1985) [Sov. Phys. Dokl. **30**, 716 (1985)].
[6] A. M. Roshchupkin and I. L. Bataronov, Izv. Vyssh. Uchebn. Zaved. Fiz. No. **3,** 57 (1996).
[7] A. M. Kosevich and V. S. Boĭko, Usp. Fiz. Nauk **104**, 201 (1971) [Sov. Phys. Usp. **14**, 286 (1971)].
[8] V. S. Savenko and O. M. Ostrikov, Izv. Akad. Nauk Belarus Ser. Fiz.-Mat. Nauk (1997), VINITI deposited Paper No. 327-B97.
[9] V. S. Savenko and O. M. Ostrikov, Abstracts of Papers presented at the Fourth International Conference on ''Action of Electromagnetic Fields on Plasticity and Strength of Materials,'' Voronezh, 1996 [in Russian], p. 20.
[10] L. D. Landau and E. M. Lifshitz, *Theory of Elasticity*, 3rd English ed. (Pergamon Press, Oxford, 1986) [Russ. original, 4th ed., Nauka, Moscow, 1987].

Translated by R. M. Durham
Edited by David L. Book

Operating characteristics and their anisotropy in a high-power laser (1.5 W, 300 K) with a quantum-dot active region

Yu. M. Shernyakov, A. Yu. Egorov, B. V. Volovik, A. E. Zhukov, A. R. Kovsh, A. V. Lunev, N. N. Ledentsov, M. V. Maksimov, A. V. Sakharov, V. M. Ustinov, Zhen Zhao, P. S. Kop'ev, Zh. I. Alferov, and D. Bimberg

A. F. Ioffe Physicotechnical Institute, Russian Academy of Sciences, St. Petersburg; Technical University, Berlin, Germany

(Submitted January 6, 1998)
Pis'ma Zh. Tekh. Fiz. **24**, 50–55 (May 12, 1998)

Continuous-wave lasing has been demonstrated in a vertically coupled quantum-dot laser with a high output power (1.5 W) at room temperature. It was shown that anisotropy of the quantum dot profile leads to anisotropy of the laser operating characteristics. © *1998 American Institute of Physics.* [S1063-7850(98)00905-7]

Considerable success has recently been achieved in the technology, physics, and instrumental applications of semiconductor heterostructures with self-organizing quantum dots fabricated by self-organization during growth. Lasing via quantum-dot states has been demonstrated in these structures using optical[1] and injection[2,3] pumping. Quantum-dot lasers have now almost reached a level where they are suitable for commercial applications. In Ref. 4 we reported cw lasing in a vertically coupled quantum-dot structure with an output power of ~1 W at room temperature. Surface-emitting quantum-dot lasers having characteristics as good as the best values for vertical quantum-well lasers of similar geometry were demonstrated in Ref. 5.

Here we report further improvements in the operating characteristics of quantum-dot lasers and the attainment of a high cw output power of 1.5 W at room temperature. The laser structure was grown on a GaAs(100) substrate in a standard distributed-feedback double-heterostructure geometry with a graded-index waveguide.[6] The active region, an array of vertically coupled quantum dots, was deposited at the center of a 0.2 μm thick GaAs layer bounded on either

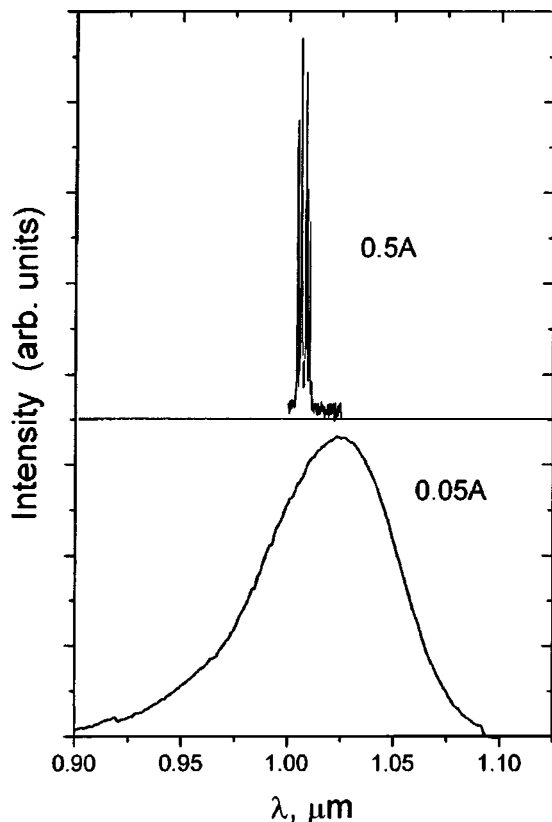

FIG. 1. Electroluminescence and lasing spectra for a quantum-dot laser structure at 300 K. Stripe length 900 μm and width 100 μm.

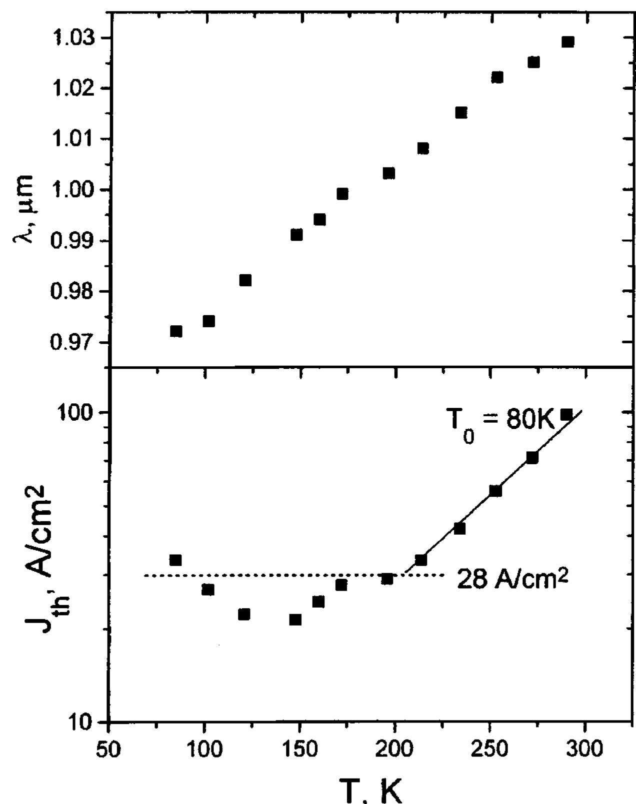

FIG. 2. Threshold current density and lasing wavelength versus temperature for a quadruply cleaved sample.

 © 1998 American Institute of Physics

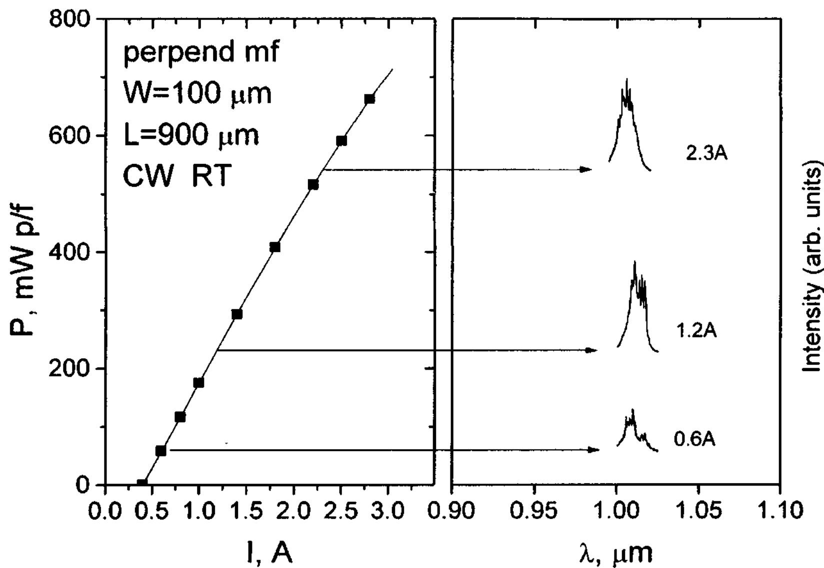

FIG. 3. Current–voltage characteristic and lasing spectra for several pump currents. Stripe length 900 μm and width 100 μm.

side by short-period AlAs(20 Å)/GaAs(20 Å)/10 superlattices. The formation process, structure, and optical properties of (In,Ga)As–GaAs vertically coupled quantum dots were described by us in detail in Ref. 7. An array of vertically coupled quantum dots was formed by four-cycle deposition of 30 Å thick $In_{0.4}Ga_{0.6}As$ layers separated by 50 Å $Al_{0.15}Ga_{0.85}As$ intermediate layers.

The substrate temperature for the deposition of the active layer and the 100 Å thick AlGaAs coating layer was 480 °C and for the growth of the remaining structure, it was −600 °C. The lasers were fabricated in a stripe geometry with a stripe width of 100 μm (shallow mesa structure). We investigated stripes fabricated parallel and perpendicular to the [0–11] direction. We also investigated samples with four cleaved faces where the output losses were negligible, i.e., the case of an ''infinitely long'' stripe. No insulating coatings were deposited on the mirrors.

Figure 1 shows the lasing and electroluminescence spectra of this laser structure at 300 K. The spectral position of the lasing line coincides with the electroluminescence peak obtained at low excitation density. Thus, for the quadruply cleaved samples and long stripes, lasing takes place via the ground state of the vertically coupled quantum dots. The threshold current density J_{th} at room temperature for the quadruply cleaved samples is 100 A/cm^{-2} and for the stripes perpendicular to the [0–11] direction it is 330 A/cm^{-2} (stripe length 900 μm). An interesting fact is that for stripes parallel to the [0–11] direction, the threshold density is higher, 550 A/cm^{-2}. For stripes perpendicular to the [0–11] direction, the internal quantum efficiency, determined from the dependence of the reciprocal differential efficiency on the stripe length, was 83%; for parallel stripes this efficiency was slightly lower, 61%. The dependence of the parameters of quantum-dot lasers on the stripe orientation is attributed to the anisotropy of the wave function at the dots which is caused by the anisotropy of their profile.[8] The internal losses for both orientations were approximately the same, around 13 cm^{-1}. Thus, the dependence of J_{th} on the stripe orientation cannot be attributed to the light scattering anisotropy in the waveguide.

Figure 2a gives the threshold current density as a function of temperature for a quadruply cleaved sample. In the range 80–150 K the threshold density decreases with increasing temperature. This type of behavior is caused by redistribution of carriers between dots with different localization energies and is typical of quantum-dot lasers.[9] It is interesting to note that in the range 80–200 K the threshold current density does not exceed 27 A/cm^{-2}. The temperature dependence of the lasing wavelength (Fig. 2b) is approximately the same as that of the GaAs band gap. Thus, an increase in temperature is not accompanied by any abrupt change in the lasing mechanism (hopping to excited states or wetting-layer states).

Figure 3a gives the current–voltage characteristic of the laser at room temperature and Fig. 3b gives the lasing spectra at certain fixed pump currents. The maximum lasing power at both mirrors was around 1.5 W at room temperature.

To sum up, we have demonstrated that vertically coupled quantum-dot structures are potentially useful for lasers with high output powers and we have shown that the operating characteristics of quantum-dot lasers depend strongly on the stripe orientation.

[1] N. N. Ledentsov, V. M. Ustinov, A. Yu. Egorov, A. E. Zhukov, M. V. Maximov, I. G. Tabatadze, and P. S. Kop'ev, Fiz. Tekh. Poluprovodn. **28**, 1484 (1994) [Semiconductors **28**, 832 (1994)].

[2] A. Yu. Egorov, A. E. Zhukov, P. S. Kop'ev, N. N. Ledentsov, M. V. Maksimov, and V. M. Ustinov, Fiz. Tekh. Poluprovodn. **28**, 1439 (1994) [Semiconductors **28**, 809 (1994)].

[3] N. Kirstaedter, N. N. Ledentsov, M. Grundmann, D. Bimberg, U. Richter, S. S. Ruvimov, P. Werner, J. Heydenreich, V. M. Ustinov, M. V. Maximov, P. S. Kop'ev, and Zh. I. Alferov, Electron. Lett. **30**, 1416 (1994).

[4] M. V. Maximov, Yu. M. Shernyakov, N. N. Ledentsov, A. F. Tsatsul'nikov, Zhen Zhao, A. V. Lunev, A. V. Sakharov, V. M. Ustinov, A. Yu. Egorov, A. E. Zhukov, A. R. Kovsh, S. V. Zaitsev, N. Yu. Gordeev, P. S. Kop'ev, Zh. I. Alferov, and D. Bimberg, Extended Abstracts of the Annual International Symposium ''Nanostructures: Physics and Technology,'' St. Petersburg, 1997, pp. 202–205.

[5] J. A. Lott, N. N. Ledentsov, V. M. Ustinov, A. Yu. Egorov, A. E. Zhukov, P. S. Kop'ev, Zh. I. Alferov, and D. Bimberg, Electron. Lett. **33**, 1150 (1997).

[6] Zh. I. Alferov, N. Yu. Gordeev, S. V. Zaitsev, P. S. Kop'ev, I. V. Kochnev, V. V. Komin, I. L. Krestnikov, N. N. Ledentsov, A. V. Lunev, M. V. Maximov, S. S. Ruvimov, A. V. Sakharov, A. F. Tsatsul'nikov, Yu. M. Shernyakov, and D. Bimberg, Fiz. Tekh. Poluprovodn. **30**, 357 (1996) [Semiconductors **30**, 197 (1996)].

[7] N. N. Ledentsov, V. A. Shchukin, M. Grundmann, N. Kirstaedter, J. Böhrer, O. Schmidt, D. Bimberg, V. M. Ustinov, A. Yu. Egorov, A. E. Zhukov, P. S. Kop'ev, S. V. Zaitsev, N. Yu. Gordeev, Zh. I. Alferov, A. I. Borovkov, A. O. Kosogov, S. S. Ruvimov, P. Werner, U. Gösele, and J. Heydenreich, Phys. Rev. B **54**, 8743 (1996).

[8] A. F. Tsatsul'nikov, N. N. Ledentsov, M. V. Maximov, A. Yu. Egorov, A. E. Zhukov, S. S. Ruvimov, V. M. Ustinov, V. V. Komin, I. V. Kochnev, P. S. Kop'ev, Zh. I. Alferov, and D. Bimberg, Fiz. Tekh. Poluprovodn. **30**, 1793 (1996) [Semiconductors **30**, 938 (1996)].

[9] A. E. Zhukov, V. M. Ustinov, A. Yu. Egorov, A. R. Kovsh, A. F. Tsatsul'nikov, N. N. Ledentsov, S. V. Zaitsev, N. Yu. Gordeev, P. S. Kop'ev, and Zh. I. Alferov, International Symposium on *Formation, Physics and Device Application of Quantum Dot Structures,* Sapporo, Japan, Jpn. J. Appl. Phys., **36**, Part 1, 4216 (1997).

Translated by R. M. Durham
Edited by David L. Book

New method for measurement of the concentration of acceptor centers in photorefractive crystals

M. P. Petrov, V. M. Petrov, and P. M. Karavaev

A. F. Ioffe Physicotechnical Institute, Russian Academy of Sciences, St. Petersburg

(Submitted December 22, 1997)
Pis'ma Zh. Tekh. Fiz. **24**, 56–60 (May 12, 1998)

A new method for measurement of the concentration of deep traps is proposed and confirmed theoretically and experimentally. The method involves measuring the intensities of the signals formed by the first and second harmonics of a holographic grating. © *1998 American Institute of Physics.* [S1063-7850(98)01005-2]

The concentration N_A of acceptor centers (deep traps) is one of the most important parameters of photorefractive media, and its measurements are of major interest for the physics of photorefractive materials and semiconductors. Here we propose a new way of measuring this concentration.

As was described in detail in Ref. 1, a nonlinear recording regime may be established when holograms are recorded in photorefractive media using a high-contrast interference pattern. In this case, not only is a hologram (refractive index grating) recorded with the wave vector K_g corresponding to that of the interference pattern but gratings are also recorded with multiple ($2K_g$, $3K_g$, and so on) wave vectors. Moreover, if a thin hologram is considered, diffraction orders are observed not only from the fundamental-frequency ("linear") grating but also from higher harmonics ("nonlinear" gratings), known as non-Bragg diffraction orders.

If the intensity of the diffraction orders is measured using adaptive interferometry, where one of the recording beams is phase-modulated[1] (with the modulation amplitude θ and frequency Ω), the light intensity in the first non-Bragg order of a thin hologram (three-wave mixing) is described by[1]

$$I=I_{\mathrm{const}}-4\sqrt{I_R I_S \eta_0 \eta_{NL}}J_0(\theta)[J_1(\theta)\sin(\delta)\cos(\Omega t)+J_2(\theta)\cos(\delta)\cos(2\Omega t)]. \quad (1)$$

Here I_{const} is the constant component of the output intensity, I_R and I_S are the intensities of the phase-modulated and unmodulated beams, respectively, η_0 and η_{NL} are the diffraction efficiencies of the linear (K_g) and nonlinear ($2K_g$) gratings, J_0, J_1, and J_2 are Bessel functions of the zeroth, first, and second orders, respectively, and δ is the phase difference between the linear and nonlinear gratings. In previous studies δ was introduced empirically.

Here, we put forward an explanation for the phase shift δ and we demonstrate that measurements of this shift can be used to estimate the acceptor concentration, which is responsible for the photorefraction effect in light-sensitive materials.

It has been established[2] that a holographic grating has an initial phase shift Δ relative to the interference pattern. Provided that the drift recording mechanism predominates in the measurements, in accordance with Ref. 2, we have

$$\Delta=\arctan E_0/E_q \approx E_0/E_q, \quad (2)$$

where E_0 is the external field applied to the sample,

$$E_q=eN_A/K_g\varepsilon\varepsilon_0, \quad (3)$$

e is the electron charge, N_A is the concentration of acceptor centers (traps), ε is the permittivity of the medium, and ε_0 is the permittivity of vacuum. Since Δ is proportional to K_g, it is natural to assume that for a grating with $2K_g$, the phase shift relative to the interference pattern will be 2Δ, and thus the phase shift between the linear and nonlinear gratings is $\delta=\Delta$.

We consider the ratio of the amplitudes I^{Ω} of the first harmonic and $I^{2\Omega}$ of the second of the output signal, using Eq. (1):

$$\frac{I^{\Omega}}{I^{2\Omega}}=\frac{J_1(\theta)\sin(\delta)}{J_2(\theta)\cos(\delta)}\approx\frac{4}{\theta}\tan(\delta)\approx\frac{4}{\theta}\delta, \quad (4)$$

which yields

$$\frac{I^{\Omega}}{I^{2\Omega}}=\frac{4}{\theta}\frac{E_0}{E_q}. \quad (5)$$

It is clear from Eq. (5) that having measured the ratio of the harmonics I^{Ω} and $I^{2\Omega}$, we can find E_q and then the deep trap concentration N_A.

For the experiments we used holographic adaptive interferometry[1] and the following samples: $Bi_{12}SiO_{20}$ (BSO) in a "PRIZ" geometry[3,4] of thickness $T=0.8$ mm and $Bi_{12}TiO_{20}$ (BTO). The BTO crystal was 0.8 mm thick, (110) cut, the electric field was applied along the $[1\bar{1}0]$ axis, and the vector of the recorded grating was directed along $[1\bar{1}0]$. The light source was a 20 mW He–Ne laser ($\lambda=633$ nm) and the signal was recorded using a photodiode spectrum analyzer which allowed the first and second harmonics to be measured simultaneously. The measurements were made at frequencies ($\Omega/2\pi=180$ Hz (BSO), $\Omega/2\pi=8$ kHz (BTO)) far from the resonant frequencies of the photorefractive effect,[5] with the contrast $m=0.8$. The phase modulation amplitude was $\theta=0.2$ rad and an external field $E_0=1.8$ kV was applied to the samples. The ratio $I^{\Omega}/I^{2\Omega}$ was investigated as a function of E_0 and K_g.

 © 1998 American Institute of Physics

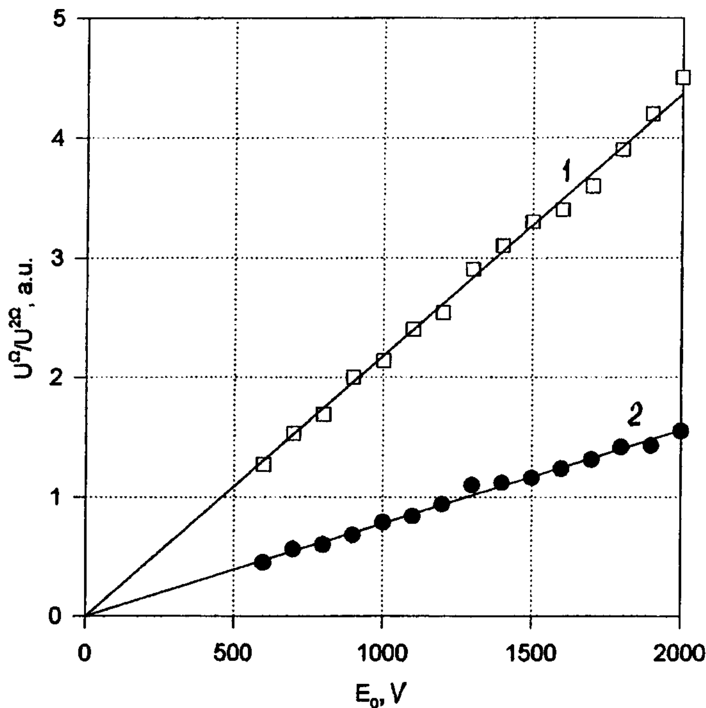

FIG. 1. Dependence of $U^{\Omega}/U^{2\Omega}$ on the external field E_0 for $K_g = K_{\rm eff} = 624\ \mathrm{mm}^{-1}$ for BTO (*1*) and BSO (*2*), respectively.

The experimental results are plotted in Figs. 1 and 2. It can be seen that the experimental curves show good agreement with the theory. In the calculations of N_A for BSO allowance was made for "clamping" of the field to the negative electrode (bottleneck effect[3]). In this case, the dependence for BSO is plotted as a function of $K_{\rm eff} = \sqrt{K_g^2 + K_z^2}$, where K_z is an empirical constant (fitting parameter). Good agreement with the theory (a linear dependence on $K_{\rm eff}$) is obtained for $K_z = 80\ \mathrm{mm}^{-1}$. The thickness of the charge layer near the negative electrode can then be estimated as $h \approx 2\pi/K_z = 12.5\ \mu$m.

These data were used to determine the trap concentrations for BSO: $N_A = 5.5 \times 10^{16}\ \mathrm{cm}^{-3}$ and for BTO: $N_A = 6.3 \times 10^{15}\ \mathrm{cm}^{-3}$. These figures show satisfactory qualitative agreement with estimates of N_A obtained by other methods: $N_A(\mathrm{BSO}) \cong 1.2 \times 10^{16}\ \mathrm{cm}^{-3}$ and $N_A(\mathrm{BTO}) = 2.3 \times 10^{15}\ \mathrm{cm}^{-3}$ (Refs. 5 and 6).

This method of comparing the first and second harmonics to determine Δ can also be used to record two-wave mixing.[1] Preliminary experiments were carried out using this technique and qualitative agreement was established with the data presented above.

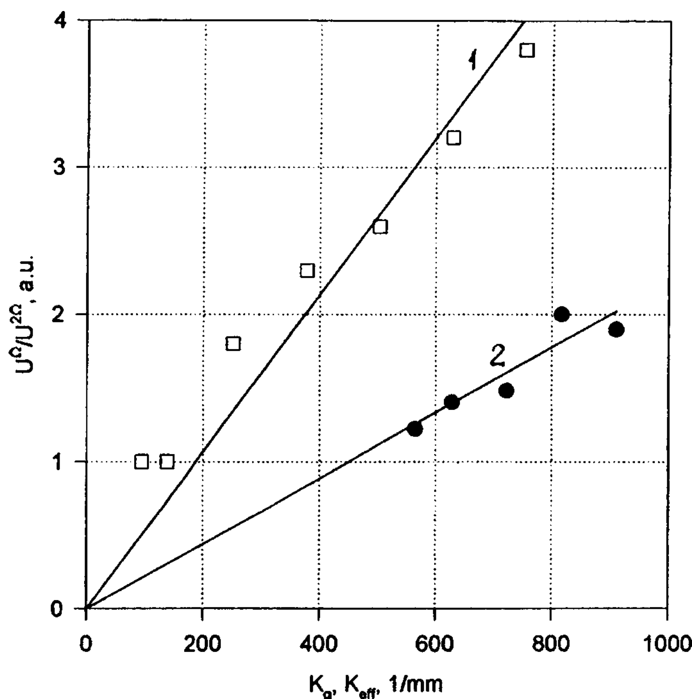

FIG. 2. Dependence of $U^{\Omega}/U^{2\Omega}$ on K_g (*1* — BTO) and $K_{\rm eff}$ (*2* — BSO); $E_0 = 6$ kV/cm for BTO and $E_0 = 22.5$ kV for BSO.

To sum up, a very simple and effective method of determining the concentration of deep traps in photorefractive crystals has been proposed for the first time.

This work was carried out under the Russian Fund for Fundamental Research, Project No. 98-02-18254.

[1] M. P. Petrov, V. M. Petrov, I. S. Zouboulis, L. P. Xu, Opt. Commun. **134**, 569 (1997).

[2] *Photorefractive Materials and Their Applications*, Parts I and II, edited by P. Günter and J. P. Huignard (Springer-Verlag, Berlin, 1998, 1989).

[3] M. P. Petrov, S. I. Stepanov, and A. V. Khomenko, *Photorefractive Crystals in Coherent Optical Systems* (Springer-Verlag, Berlin, 1991).

[4] V. M. Petrov and M. P. Petrov, Pis'ma Zh. Tekh. Fiz. **21**(11), 18 (1995) [Tech. Phys. Lett. **21**, 403 (1995)].

[5] M. P. Petrov, V. M. Petrov, V. V. Brycsin, I. S. Zouboulis, A. Gerwens, and E. Kratzig, Opt. Lett. **22**, 14 (1997).

[6] J. P. Huignard, J. P. Herriau, G. Rivert, and P. Gunter, Opt. Lett. **5**, 102 (1980).

Translated by R. M. Durham
Edited by David L. Book

Mechanism for the anomalously long range of a ''hard laminar flame''

G. A. Luk'yanov and Gr. O. Khanlarov

Institute of High-Performance Computation and Databases, St. Petersburg
(Submitted December 8, 1997)
Pis'ma Zh. Tekh. Fiz. **24**, 61–65 (May 12, 1998)

An explanation is given for the anomalously long range of a type of laminar flame which has been termed a ''hard laminar flame.'' A model of an isobaric laminar jet with a given bulk energy release is used to show that the unusual properties of the flame are determined by its two-layer structure. The outer hot sheath stabilizes the flow as a whole and creates conditions for extended axial flow of the cold gas mixture. © *1998 American Institute of Physics.* [S1063-7850(98)01105-7]

In Refs. 1 and 2 the structure, properties, and conditions are described for the existence of a previously unknown type of burning, laminar jet referred to by the author as a ''hard laminar flame.'' This type of jet flow exhibits unusually high stability and range. No explanation of the physical nature of the anomalous properties of a hard laminar flame is given in the literature. Laminar flow is conserved in this type of flame up to Reynolds numbers Re (determined from the parameters at the nozzle edge and the nozzle diameter d) of the order of 3×10^4. The length of the flame reaches $(200–400)d$. A hard laminar flame is created when a mixture of fuel (natural) gas and air with an excess air coefficient $0.2<n\leqslant0.6$ flows into air from a circular nozzle ($d=2–4$ mm) and an ignitor is positioned near the nozzle ($x/d<3$). The diameter of this hard laminar flame at a distance of 150 mm from the nozzle is $(1.5–4)d$ depending on n and the gas flow rate. In a narrow axial zone of length $L\approx(60–80)d$ the temperature, gas composition, and dynamic pressure remain almost constant. The thickness of the burning sheath surrounding the cold axial zone is 0.4–1 mm.

In gas jets (without combustion), laminar flow at a nozzle edge is maintained for Reynolds numbers $\mathrm{Re}_*\leqslant2300$ and the region of laminar flow in the jet (before the cross section where a transition to turbulence takes place) has length l, which is determined by the number $\mathrm{Re}_l=\rho u_m l/\mu=2\times10^4$, where ρ is the density, u_m is the flow rate on the axis of the jet in the transition cross section, and μ is the viscosity.[3] The range L of laminar jets (the distance from the nozzle at which the axial flow rate u or the dynamic pressure $p_D=\rho u^2/2$ decreases to a specific value, such as $u/u_0=0.9$ or $p_D/p_{D_0}=0.9$) is proportional to the number Re, although its value has an upper limit imposed by the condition $L<l$. The range $L_{0.9}$ of laminar jets is at most $(10–20)d$ (Ref. 3).

The flow in a laminar flame (burning jet) differs substantially from that in isothermal and fuel gas jets without combustion. This difference is caused by their different hydrodynamic structure. Unlike an inert jet, a flame has two clearly defined flow regions: an axial zone of cold gas flow and a peripheral zone of heated gas flow, separated by a relatively thin combustion zone.

Heating of the gas in the combustion zone, and the reduction in density and increase in the viscosity of the gas which accompany the heating, sharply increase the role of viscosity forces (reduce the effective Reynolds number). Thus, unlike the jet flow of an inert gas, in a laminar flame the Reynolds number at the nozzle edge is not a parameter which determines the flow regime in the jet. The transition from laminar to turbulent flow in flames takes place at significantly higher numbers Re_*. In accordance with Ref. 4, for gas–air flames this number is $\mathrm{Re}_*=(3–9)\times10^3$. Data[1,2] for a hard laminar flame extend this range to $\mathrm{Re}_*\leqslant3\times10^4$.

In our view, the nature of the high stability of the flows in all types of laminar flames, including hard laminar flames, is the same and can be reduced to the stabilizing effect of a more viscous, less dense annular region of fuel gas. The unusual properties of a hard laminar flame can be explained by the characteristics of mixing and energy release in a flame of partially mixed gases for $0.2<n\leqslant0.6$, which give rise to an unusually extended annular combustion region while the axial flow of denser, less viscous cold gas is conserved. This two-layer flow structure with a substantially different ratio of inertial forces to viscosity forces in the outer and inner layers leads to the conservation of laminar flow and increases the range of the axial flow.

The determining role of the two-layer flow structure of a hard laminar flame in the mechanism responsible for its anomalously high range is confirmed by the results of mathematical modeling. A model of an isobaric laminar jet with a given law of bulk energy release was used to describe the flow in the flame. The geometry of the region and the energy release parameters of this model approximately simulate the heat of combustion. This model is undoubtedly approximate but can be used to examine the influence of energy release on the flow in a jet from the most general viewpoint.

Figure 1 gives experimental data[2] (dashed curve) showing the variation of the dynamic pressure p_D (a) and the temperature T (b) along the axis of a hard laminar flame. Also plotted are the results of approximate modeling of the flame by a jet with a given uniform release of energy in a cylindrical layer of thickness $y/d\in[1;1.5]$ and length $x/d\in[0;50]$ (curve *1*) and $x/d\in[0;100]$ (curve *2*), where x and y are the longitudinal and transverse coordinates. The experi-

 © 1998 American Institute of Physics

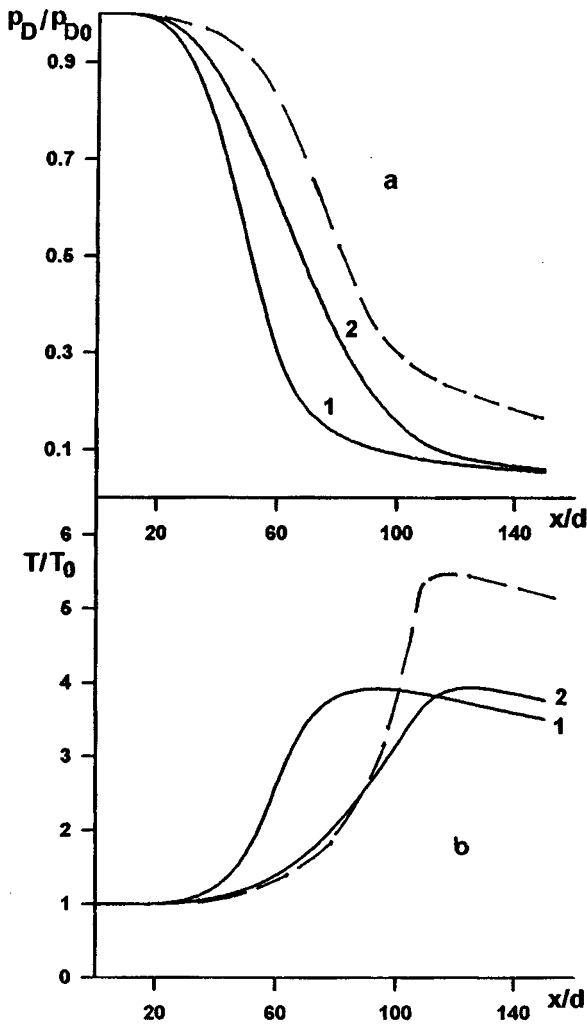

FIG. 1. Variation of the dynamic pressure p_D (a) and temperature T (b) along the axis of a laminar flame. The dashed curves give the experimental results[2] and the continuous curves give the calculations for the jet model with a given energy release in a cylindrical layer of length $x/d=50$ (*1*) and 100 (*2*).

mental data correspond to a flow rate of the gas–air mixture of 8.35×10^{-5} m^3/s, with $n=0.6$ for $d=4$ mm. The experiment and calculations were performed for $\mathrm{Re}=\rho_0 u_0 d/\mu_0 =2000$, $T_0/T_e=1$ (where T_0 and T_e are the temperature at the nozzle edge and in the surrounding medium). In the model calculations the total energy release in the jet per unit time, relative to the enthalpy flow at the nozzle edge, is assumed to be equal to the ratio of the heat of combustion of

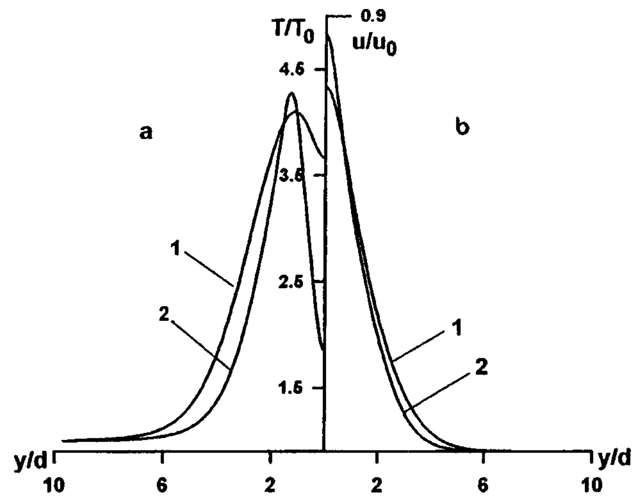

FIG. 2. Distributions of temperature T (a) and flow rate u (b) in the cross section ($x/d=75$) of the jet model of a flame. For notation see Fig. 1.

the fuel gas in the experiment.[2] Figure 2 gives the transverse profiles of T (a) and u (b) in the cross section $x/d=75$ for the flame model (curves *1* and *2*). An increase in the region of energy release increases the range and length (along the x axis) of the cold flame core. The results of the approximate modeling show good qualitative agreement with the experimental data. The anomalously long range of a hard laminar flame is in fact attributable to the two-layer structure. The outer hot sheath stabilizes the flow as a whole and creates conditions for long-range axial flow of the cold gas mixture. The mechanism for this effect is of major interest as a method of controlling jets and other flows with a bulk energy supply (such as flows with electric discharges, absorption of laser radiation, and so on).

The authors are grateful to M. Kh. Strel'ets for assistance with selection of the mathematical model and the numerical scheme.

This work was supported by the Russian Fund for Fundamental Research (Grant No. 97-01-00235).

[1] G. T. Tsygankov, Fiz. Goreniya Vzryva No. **6,** 78 (1990).
[2] G. T. Tsygankov, Fiz. Goreniya Vzryva No. **3,** 54 (1991).
[3] G. N. Abramovich, S. Yu. Krasheninnikov, I. P. Sekundov, and I. P. Smirnova, *Turbulent Mixing of Gas Jets* [in Russian], Nauka, Moscow (1974).
[4] B. Lewis and G. von Elbe, *Combustion, Flames, and Explosions of Gases* (Academic Press, New York, 1961; Mir, Moscow, 1968).

Translated by R. M. Durham
Edited by David L. Book

Optical limitation effect in a cholesteric liquid crystal–fullerene system

V. V. Danilov, A. G. Kalintsev, N. V. Kamanina, and S. A. Tul'skiĭ

Scientific-Research Institute of Laser Physics, "S. I. Vavilov State Optical Institute" All-Russia Scientific Center, St. Petersburg

(Submitted November 6, 1997)
Pis'ma Zh. Tekh. Fiz. **24**, 66–69 (May 12, 1998)

An investigation is made of optical limitation in nematochiral liquid crystal composites with added fullerene C_{70} under conditions such that diffraction suppresses absorption. It is shown that these systems have the lowest energy threshold for nonlinearity yet recorded. A qualitative explanation of the results is put forward. © *1998 American Institute of Physics.*
[S1063-7850(98)01205-1]

Optical limiters which utilize fast Kerr nonlinearity in distributed-feedback systems were proposed in Refs. 1 and 2. The optical limitation effect in this system was demonstrated experimentally using a chiral liquid crystal with an added ketocyanine dye (known as Borrmann cells).[2] However, the use of fullerene solutions for optical limitation has attracted considerable attention among researchers. In these solutions, a successful combination of photodynamic parameters, i.e., a short-lived S_1 state, a high rate of interconversion to the triplet state and long-lived triplet state, and cross sections for absorption from excited singlet and triplet states exceeding those for the ground state, can produce intensive absorption via triplet and excited singlet states in a medium having a high initial transparency.[3]

Here we report the results of an investigation of the optical limitation effect in a structure which combines the characteristics of both these types of limiter and comprises a Borrmann cell where fullerene C_{70} is used as a resonant absorbing impurity.

The Borrmann cell was a planar quartz capillary filled with a planar-oriented nematochiral composite consisting of benzonitriles and cyanobiphenyls with a phase-transition temperature $T_{n-c}\sim 47$ °C and a selective reflection band at $\lambda\sim 545$ nm. The gap was 20μm thick. The initial planar orientation was created by mechanically rubbing the substrate surface which had been precoated with a polyimide film orientant. The C_{70} concentration in the working liquid-crystal composite was 0.22–0.24 abbr.%. The homogeneity of the working solution was monitored under a microscope. The cell was filled in vacuum in a previously evacuated and outgassed chamber at a temperature of ~ 60 °C.

The system was excited in the absorption band of the impurity (fullerene) by linearly polarized second-harmonic radiation from a single-pulse yttrium aluminum garnet laser ($\tau_{\rm puls}\sim 15$ ns, $E_{\rm puls}$ up to 0.5 J). The radiation intensity was varied by means of calibrated light filters. The output signal energy was measured using an ILD device with a lower sensitivity limit of $\sim 10^{-9}$ J.

In all cases, the exciting radiation fell within the region of overlap of the absorption and selective reflection bands.

Experimental investigation of the operation of Borrmann cells as optical limiters involved studying their optical transmission (the radiation intensity at the cell exit $I_{\rm out}$) as a function of the input intensity $I_{\rm in}$.

These dependences are plotted in Fig. 1 (curves *1* and *4*). Also plotted are similar dependences for a solution of C_{70} in a nematic (curve *3*) and for a nematochiral composite without an absorbing component (curve *2*). A comparison between curves *1* and *3* reveals that in addition to the usual limiting effect characteristic of fullerene solutions, the Borrmann cell also exhibits a region of limiting at appreciably lower intensity levels. For C_{70} this intensity region coincides with the region in which dynamic hysteresis is observed experimentally in similar Borrmann systems (10^{-6}–10^{-3} J/cm^2), where dyes as used as absorbing impurities.[2–4] Excitation in the spectral range where the diffraction suppression of absorption is observed (Borrmann effect) leads to an abrupt change in the two states: transmission and reflection. This is because when the critical intensity is reached, the

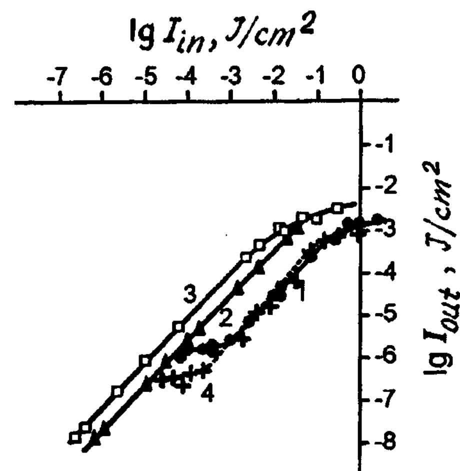

FIG. 1. Optical limitation effect in a liquid-crystal composite with fullerene C_{70}: *1*, *4* — fullerene C_{70} in a Borrmann cell: *1* — 22°, *4* — 30 °C; *2* — $I_{\rm out}$ versus input intensity $I_{\rm in}$ for a pure chiral system; *3* — fullerene C_{70} in a nematic.

 © 1998 American Institute of Physics

change in the refractive index (as a result of resonance saturation of excited impurity molecules[2]) leads to a change in the operating wavelength in the medium. Unlike the systems described above, the critical threshold energy for limiting in this system is the lowest achieved so far ($E_{\rm thr} < 10^{-5}$) J/cm^2. However, it should be noted that this chiral system is extremely sensitive to the temperature conditions of the experiment (curves *1* and *4*).

We would like to conclude by thanking V. P. Budtov for supplying the fullerene C_{70}.

[1] V. V. Danilov, V. A. Smirnov, and S. V. Fedorov, Abstracts of Papers presented at the Third International Workshop ''Fullerenes and Atomic Clusters,'' IWFAC'97, St. Petersburg, 1997, p. 156.
[2] M. V. Gryaznova, V. V. Danilov, N. V. Kamanina, V. A. Smirnov, and S. V. Fedorov, Opt. Zh. **64**(10), 115 (1997) [J. Opt. Technol. **64**, 987 (1997)].
[3] J. R. Heflin, S. D. Wang, D. Marein *et al.*, Proc. SPIE **2530**, 176 (1995).
[4] L. Zagainova, G. Klimusheva, L. Yatsenko, and V. Danilov, Mol. Cryst. Liq. Cryst. **192**, 279 (1992).

Translated by R. M. Durham
Edited by David L. Book

Influence of substrate thickness on plasma resonance in a semiconductor heterostructure with a two-dimensional electron gas

V. V. Popov and G. M. Tsymbalov

Institute of Radio Engineering and Electronics, Russian Academy of Sciences (Saratov Branch)

(Submitted November 21, 1997)
Pis'ma Zh. Tekh. Fiz. **24**, 70–74 (May 12, 1998)

A strict electrodynamic approach is used to analyze the excitation of oscillations of a two-dimensional electron plasma by an external plane electromagnetic wave in a semiconductor heterostructure with a grating coupling element. An analysis is made of the influence of the substrate thickness on the resonance magnitude and the profile of the resonance curve.
© *1998 American Institute of Physics.* [S1063-7850(98)01305-6]

An investigation of resonant absorption of electromagnetic waves by two-dimensional plasmons can provide useful information of the properties of two-dimensional space charge layers in GaAs/AlGaAs heterojunctions. To excite the two-dimensional plasmons, a metal grating with the period $L \ll \lambda$ is formed on the surface of the heterostructure, where λ is the electromagnetic wavelength.[1,2] An external plane electromagnetic wave incident normally on the surface of a heterostructure with a grating coupling element excites two-dimensional plasmons with the wave vectors $K_n = 2\pi n/L$ ($n = 1,2,3,\dots$). To achieve the most efficient coupling, the grating is positioned at a distance $d \ll L$ from the two-dimensional space charge layer and is isolated from this by a layer of wide-gap AlGaAs semiconductor, for which the grating coverage W/L is close to unity, where W is the width of the metal stripes.

Experimental investigations are usually made of the frequency dependences (spectra) of $\Delta T = (T_0 - T)/T_0$, where T is the coefficient of (power) transmission of an electromagnetic wave through the structure in a given frequency range, which includes the plasma resonant frequency, and T_0 is the transmission coefficient of the reference signal. This reference signal is usually the transmission spectrum of the electromagnetic wave through the same structure, but with different external parameters (gate electrode voltage, static magnetic field) which change the properties (conductivity) of the two-dimensional electron gas. These parameters are selected so that the reference signal spectrum contains no resonance characteristics caused by the excitation of two-dimensional plasma oscillations in this frequency range.

The resonant frequency and the profile of the resonance curve clearly depend not only on the properties of the two-dimensional electron plasma in the heterojunction but also on other electrophysical and geometric parameters of the structure and the grating coupling element. These factors may have a very substantial influence and this must be taken into account in the interpretation of experimental results. For instance, it was shown in Ref. 3 that the radiative damping of plasmons caused by their scattering at a grating coupling element may be comparable with the dissipative damping of two-dimensional plasmons which is determined by the finite relaxation time τ of the electron momentum in the two-dimensional plasma layer. Additional allowance for the dielectric losses (introducing the complex permittivity $\varepsilon = \varepsilon' - i\varepsilon''$) in the layers of material forming the heterostructure, as well as allowance for the electron relaxation and radiative damping, could quantitatively explain[4] the width of the plasma resonance line observed experimentally in Ref. 1. The results presented in Refs. 3 and 4 were obtained using a strict electrodynamic approach developed in Refs. 5 and 6.

Here, the approach developed in Refs. 5 and 6 is used to study the influence of the substrate thickness (semi-insulating GaAs) on the profile of the plasma resonance curve in a semiconducting GaAs/AlGaAs heterostructure with a two-dimensional electron gas. The calculations were made for the parameters of the structure used in the experiments:[1] $L = 8.7 \times 10^{-5}$ cm, $d = 8 \times 10^{-6}$ cm, $W/L = 0.90$, $\varepsilon'_{\mathrm{GaAs}} = 12.8$, $\varepsilon'_{\mathrm{AlGaAs}} = 11$, and surface electron concentration in heterojunction $N_s = 6.7 \times 10^{11}$ cm^{-2}.

Figure 1 shows calculated frequency dependences of the transmission coefficients of the investigated and reference signals, obtained neglecting dissipation ($\tau \to \infty$, $\varepsilon'' = 0$) for the substrate thickness $h = 300$ μm. The reference signal was the transmission spectrum of the electromagnetic wave

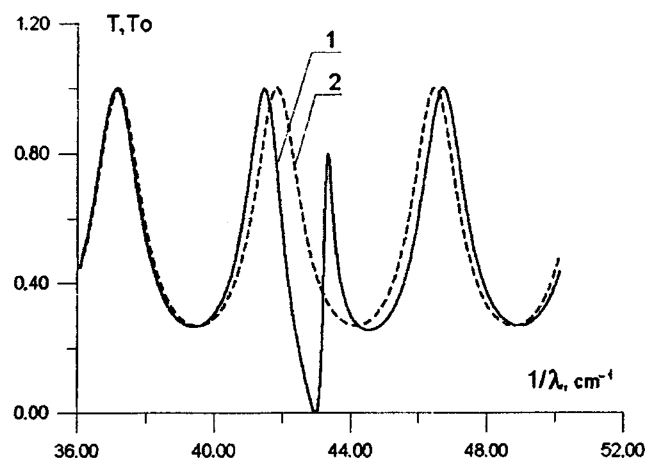

FIG. 1. Transmission spectra of investigated (curve *1*) and reference (curve *2*) signals.

 © 1998 American Institute of Physics

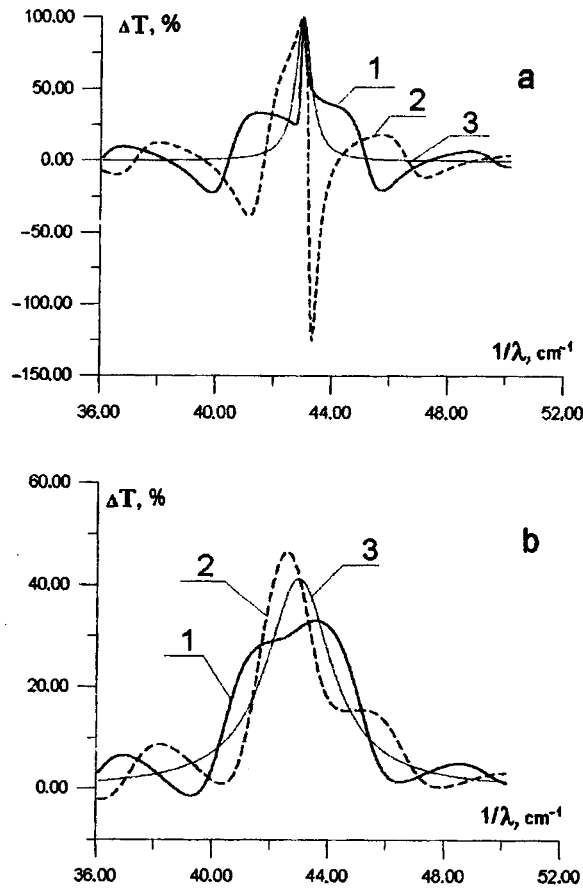

FIG. 2. Resonance curves for various substrate thicknesses h: *1* — 310 μm, *2* — 300 μm, *3* — $h \rightarrow \infty$; a — neglecting dissipation, b — allowing for dissipation ($\tau = 7 \times 10^{-12}$ s, $\varepsilon'' = 0.37$).

through the structure without an electron plasma layer ($N_s = 0$). At the plasma resonance frequency ($1/\lambda = 1/\lambda_R = 43$ cm^{-1}), the transmission coefficient T decreases to zero, i.e., the electromagnetic wave is completely reflected from the structure. The situation here is similar to the reflection of a wave in a long line by a load in the form of a series oscillatory circuit under conditions where voltage resonance exists in the circuit.[7] The values of T off resonance and T_0 vary periodically with frequency as a result of electromagnetic wave interference in the substrate. The small shift of the investigated and reference spectra in Fig. 1 is caused by the influence of the finite (purely reactive in the absence of losses) conductivity of the two-dimensional plasma layer on the effective optical thickness of the substrate.

The behavior of ΔT calculated using the spectra of T and T_0 is plotted as a function of frequency in Fig. 2 for different layer thicknesses h. Interference effects in the substrate distort the profile of the resonance curve compared with the case $h \rightarrow \infty$. The oscillations of ΔT off-resonance are attributable to the shift of the spectra of the investigated and reference signals (Fig. 1). In the absence of dissipation, the value of ΔT at resonance naturally reaches 100% regardless of the substrate thickness (Fig. 2a). With allowance for dissipation (Fig. 2b), the height of the resonance curve depends on the substrate thickness and for selected parameters of the structure may vary between 30 and 50%. In this case, the highest resonance value, i.e., the most effective excitation of two-dimensional plasmons, is achieved for $h = n\lambda_R/2\sqrt{\varepsilon_{\mathrm{GaAs}}}$ ($n = 1,2,3\ldots$), i.e., when plasma resonance occurs at the maximum of the interference curve (Fig. 1).

Interference effects in the substrate are usually considered by experimentalists as undesirable and the substrate is specially made non-plane-parallel to eliminate these effects.[1,2] Such experimental conditions are closest to the case of a semi-infinite substrate. In fact, curve *3* in Fig. 2b is closest to the experimental resonance curve.[1] We have shown here that by specially selecting the substrate thickness we can substantially improve the efficiency of excitation of two-dimensional plasmons by an external electromagnetic wave.

This work was financed by the Russian Fund for Fundamental Research (Project Code 96-02-19211a).

[1] E. Batke, P. Heitmann, and C. W. Tu, Phys. Rev. **34**, 6951 (1986).
[2] P. Heitmann, Surf. Sci. **170**, 332 (1986).
[3] O. R. Matov, O. V. Polishchuk, and V. V. Popov, Pis'ma Zh. Tekh. Fiz. **18**(16), 86 (1992) [Sov. Tech. Phys. Lett. **18**, 545 (1992)].
[4] O. R. Matov, O. V. Polishchuk, and V. V. Popov, Pis'ma Zh. Tekh. Fiz. **19**(17), 37 (1993) [Tech. Phys. Lett. **19**, 545 (1993)].
[5] O. R. Matov, O. V. Polishchuk, and V. V. Popov, Radiotekh. Elektron. **37**, 2242 (1992).
[6] O. R. Matov, O. V. Polischuk, and V. V. Popov, Int. J. Infrared Millim. Waves **14**, 1455 (1993).
[7] O. I. Fal'kovskiĭ, *Technical Electrodynamics* [in Russian], Svyaz', Moscow (1978).

Translated by R. M. Durham
Edited by David L. Book

Dielectric properties of triglycine sulfate crystals with a periodic stratified impurity distribution

I. F. Kashevich

Institute of Technical Acoustics, Belarus Academy of Sciences, Vitebsk
(Submitted November 24, 1997)
Pis'ma Zh. Tekh. Fiz. **24**, 75–80 (May 12, 1998)

Problems associated with the influence of a nonuniform impurity distribution on the properties of ferroelectric water-soluble crystals are studied. Triglycine sulfate crystals with a specially created periodically stratified distribution of chromium impurity ions are used to show that the properties of these crystals (permittivity, spontaneous polarization, pyrocoefficient) differ from those of triglycine sulfate crystals with randomly distributed impurities and also depend on the period of the structure of the inhomogeneous crystals. © *1998 American Institute of Physics.* [S1063-7850(98)01405-0]

The properties of ferroelectric crystals and their application as piezo-active and pyro-active elements depend strongly on their degree of unipolarity and on conserving the stability of this state. In turn, a nonuniform impurity distribution must play an important role in the establishment of unipolarity and in the fixing of a specific domain structure in doped ferroelectric crystals.[1,2] For instance, it is known that the domain structure of some ferroelectric crystals is in many respects the same as the configuration of the growth layers.[3,4] In this context, it is interesting to study the properties of ferroelectric crystals with a specifically formed regularly nonuniform impurity distribution. The present paper reports results of a study of the dielectric properties of triglycine sulfate (TGS) crystals with a periodic stratified distribution of Cr^{3+} chromium impurity ions as a function of the number of layers with the same impurity concentration (period).

Triglycine sulfate crystals with a periodic stratified distribution of Cr^{3+} impurity ions were obtained by periodically applying low-frequency oscillations (vibrations) having an amplitude of 3 mm and frequency 20 Hz during growth of the crystals from impurity-containing solutions. These oscillations increase the growth rate by a factor of 3–4 (Refs. 5 and 6). Since the impurity distribution coefficient for TGS is less than unity, the concentration of impurities in the crystal decreases as the growth rate increases.[7] By periodically applying vibrations to the growing crystal, the growth rate and thus the concentration of impurities in the crystal varied periodically. The impurity concentration between layers varied negligibly, approximately by $0.5–0.8\times10^{-3}$ wt.%. The period was determined by the time of crystal growth in a specific regime, dynamic or static. Inhomogeneous crystals were grown with a period between 30 and 250 μm.

While these inhomogeneous banded crystals were growing, the same solutions were also used to grow control crystals with randomly distributed impurities in static (with no vibrations applied) and dynamic regimes (with vibrations applied continuously). From these as-grown inhomogeneous and control TGS crystals containing chromium impurity ions, wafers were then cut perpendicular to the polar c axis and aluminum electrodes were deposited on these wafers such that the polarization vector was perpendicular to layers with different impurity concentrations. The temperature dependences of the permittivity ε were investigated using an E7-8 bridge and the spontaneous polarization P_s and coefficient of unipolarity k were determined by measurements of the hysteresis loop. Pyroelectric measurements were made by a dynamic method at a frequency of 20 Hz. Wafers of single-domain TGS containing L-α-alanine with known properties were used as the reference pyrodetector.

Characteristic curves of $\varepsilon(T)$ and $P_s(T)$ for as-grown crystals are plotted in Fig. 1. Curves *1*, *1'* and *2*, *2'* refer to the control crystals grown with continuously applied vibrations and in the static regime, respectively. It can be seen from Fig. 1 that the properties of the crystals with a periodic stratified impurity distribution depend on the period. For inhomogeneous crystals with a period between 60 and 150 μm the values of P_s and $\varepsilon_{\max}$ decreased at $T_{\varepsilon\max}$, the dielectric peak became broader, $T_{\varepsilon\max}$ was shifted toward higher temperatures by 1.5–3 °C, and the range of existence of the ferroelectric state also increased (Fig. 1, curves *4* and *4'*). The curves of $\varepsilon(T)$ and $P_s(T)$ for samples with layers of regular structure greater than 150 μm (Fig. 1, curves *5* and *5'*) were similar to those for control crystals grown under static conditions. These curves also showed a decrease in $\varepsilon_{\max}$, but $T_{\varepsilon\max}$ was shifted toward lower temperatures by 0.5–1 °C.

Since few impurities entered the crystal and the structure was more homogeneous,[6] the curves of $\varepsilon(T)$ and $P_s(T)$ for the control crystals grown with continuously applied vibrations and for inhomogeneous crystals with a period less than 60 μm (Fig. 1, curves *3* and *3'*) were almost the same as those for pure TGS crystals. Some difference in the properties of the inhomogeneous and control crystals clearly arises because inhomogeneous crystals with a periodic gradually varying impurity concentration have some regular impurity gradient which creates appreciable internal fields in the crystal in the direction of this gradient.[8] In these crystals this factor is stronger than the structural damage caused by the

 © 1998 American Institute of Physics

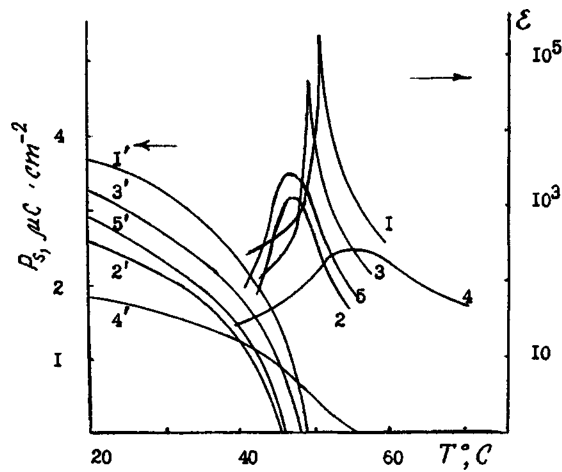

FIG. 1. Temperature dependence of the permittivity and spontaneous polarization of triglycine sulfate crystals with a periodic stratified distribution of chromium impurity ions with different periods (*3*, *3'* — less than 60 μm, *5*, *5'* — greater than 150 μm, *4*, *4'* — between 60 and 150 μm) and control crystals grown with continuously applied vibrations (*1*, *1'*) and under static conditions (*2*, *2'*).

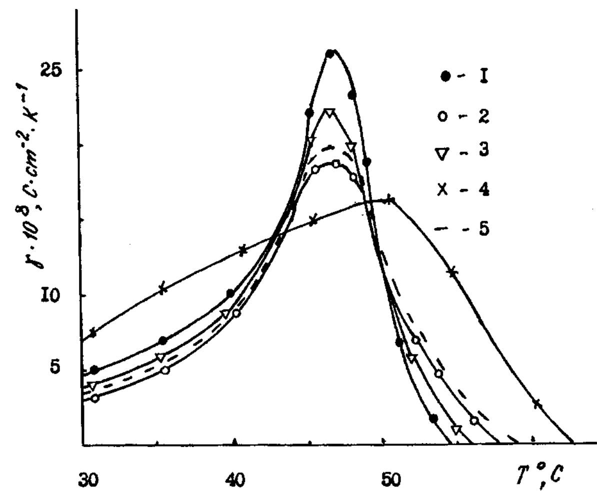

FIG. 2. Temperature dependence of the pyrocoefficient of triglycine sulfate crystals with a periodically stratified distribution of chromium impurity ions with different periods (*3* — less than 60 μm, *5* — greater than 150 μm, *4* — between 60 and 150 μm) and control crystals grown with continuously applied vibrations (*1*) and under static conditions (*2*).

incorporation of impurities and thus, the range of existence of the ferroelectric phase, i.e., $T_{\varepsilon\max}$, is shifted toward higher temperatures in inhomogeneous crystals[9] and the fraction of the volume undergoing polarization reversal is also reduced, i.e., P_s decreases.

Evidence of a stable unipolar state formed by the inhomogeneous incorporation of impurities is also provided by the fact that a series of heating (to 90 °C) and cooling cycles passing through the point T_c negligibly altered the coefficient of unipolarity of the inhomogeneous crystals whereas for the randomly doped crystals, k decreased abruptly.

The temperature dependence of the pyrocoefficient γ for crystals with a periodic stratified distribution of Cr^{3+} impurity ions with layers between 60 μm and 150 μm was similar to the $\gamma(T)$ curve for TGS crystals doped with L–α-alanine for which a stable unipolar state is achieved by means of a high internal bias field $E_{\rm in}$ created in the crystals by unidirectional irreversible glycine dipoles (Fig. 2). Heating the samples with an inhomogeneous impurity distribution above T_c did not significantly reduce the value of γ at 20 °C, whereas the control samples exhibited a sharp drop in γ at $T=20$ °C.

The fact that the properties of crystals with a periodic stratified impurity distribution depend on the period of the structure must be attributed to the influence of the defect structure on the domain structure. In our case, this influence was particularly effective when the dimensions of the layers with different impurity concentrations were comparable with the average domain sizes in the crystals (50–150 μm). In studies of the domain structure of inhomogeneous TGS crystals by the nematic liquid crystal method,[10] it was established that in samples for which the period of the structure along the axis is between 60 and 150 μm, a fairly ordered domain structure is formed corresponding to layers of different impurity concentration. Crystals having a period of less than 60 μm and greater than 200 μm and also the control crystals typically exhibited disordered lenticular domains with dimensions less than 30 μm.

Thus, the domain structure and properties of TGS crystals with a periodic stratified distribution of chromium impurity ions are determined in many respects by the period of the impurity structure.

[1] J. Eisner, Ferroelectrics **8**, 621 (1974).
[2] L. I. Dontsova, N. A. Tikhomirova, and L. G. Bulatova, Kristallografiya **33**, 450 (1988) [Sov. Phys. Crystallogr. **33**, 265 (1988)].
[3] A. L. Aleksandrovskiĭ, L. M. Kazaryan, and P. P. Rusyan, Izv. Akad. Nauk Arm. SSR, Fiz. **16**, 380 (1981).
[4] Ming Nai-Ben, Hong Jing-Fen, and Feng Duan, J. Mater. Sci. **17**, 1663 (1982).
[5] V. V. Klubovich, V. V. Mikhnevich, N. K. Tolochko, Kristallografiya **29**, 822 (1984) [Sov. Phys. Crystallogr. **29**, 488 (1984)].
[6] F. Jona and G. Shirane, *Ferroelectric Crystals* (Pergamon Press, Oxford, 1962; Mir, Moscow 1965).
[7] G. A. Andreev, Kristallografiya **12**, 104 (1967) [Sov. Phys. Crystallogr. **12**, 82 (1967)].
[8] V. V. Antipov, A. A. Blistanov, and N. G. Sorokin, Kristallografiya **30**, 734 (1985) [Sov. Phys. Crystallogr. **30**, 428 (1985)].
[9] E. T. Keve, K. L. Bye, P. W. Whipps, and A. D. Annis, Ferroelectrics **3**, 39 (1971).
[10] N. A. Tikhomirova, A. V. Ginzberg, L. I. Dontsova, S. P. Chumakova, and L. A. Shuvalov, Fiz. Tverd. Tela (St. Petersburg) **28**, 3055 (1986) [Sov. Phys. Solid State **28**, 1718 (1986)].

Translated by R. M. Durham
Edited by David L. Book

Enhancement of the luminescence yield of Er^{3+} ions at $\lambda = 1.54 \mu m$ in ZBLAN glass additionally doped with Eu^{3+} and Tb^{3+} and pumped in the range $\lambda = 0.975\ \mu m$

A. A. Andronov, I. A. Grishin, V. A. Gur'ev, V. V. Orekhovskiĭ, and A. P. Savikin

N. I. Lobachevskiĭ State University, Nizhniĭ Novgorod
(Submitted November 14, 1997)
Pis'ma Zh. Tekh. Fiz. **24**, 81–85 (May 12, 1998)

In fluorozirconate glasses the luminescence yield of Er_2^{3+} ions on the $^4I_{13/2}$–$^4I_{15/2}$ lasing transition was increased more than tenfold by additional doping with Yb^{3+} and Tb^{3+} ions.
© *1998 American Institute of Physics.* [S1063-7850(98)01505-5]

For fiber amplifiers of light in the 1.5 μm range ($^4I_{13/2} \rightarrow {}^4I_{15/2}$ transition in the Er^{3+} ion) it is preferable to use ZBLAN fluorozirconate glasses for which the magnitude and width of the gain profile are greater than those in other glasses.[1]

These characteristics are attributable to the low probability of nonradiative relaxation of the $^4I_{13/2}$ excited level of the Er^{3+} ion caused by the low phonon energy of ZBLAN glass ($E_0 \cong 575\ cm^{-1}$) and to the large ratio of the lasing-transition energy gap ($\Delta E \cong 6589\ cm^{-1}$) to the phonon energy.

However, for precisely this reason, nonradiative relaxation from the $^4I_{11/2}$ pumped level to the $^4I_{13/2}$ level is slowed.

A possible method of augmenting the population of the $^4I_{11/2}$ pumped level in ZBLAN with the long-lived $^4I_{13/2}$ level could involve additional doping of Er^{3+}-doped ZBLAN with other rare-earth elements.

It is known[2] that multicomponent doping of glasses with rare-earth elements may produce various cooperative effects involving different ions which may provide additional channels for relaxation in a system of Er^{3+} levels. We have already studied these cooperative effects in investigations of enhanced-frequency luminescence in multicomponent ZBLAN glasses doped with rare-earth elements.[3] Here we consider the influence of multicomponent doping on $\lambda = 1.54\ \mu m$ luminescence obtained by pumping diodes at $\lambda = 0.975\ \mu m$. In particular, we found that the additional doping of the ZBLAN glass with Eu^{3+} or Tb^{3+} ions appreciably increased the $\lambda = 1.54\ \mu m$ luminescence for the same level of Er^{3+} doping. This increase is evidently caused by cooperative effects in the system of rare-earth elements, although details of these effects have still to be explained.

TABLE I.

No.	Sample	I_1, a. u.	K	τ_1, ms	τ_2, ms
1	1% Er^{3+}	5	0.16	10.0	6.0
2	6% Er^{3+}	20	0.3	9.0	5.0
3	1% Er^{3+} + 3% Yb^{3+}	20	0.08	7.5	1.8
4	1% Er^{3+} + 1% Eu^{3+}	26	1.2	2.0	~0.3
5	1% Er^{3+} + 3% Yb^{3+} + 0.5% Tb^{3+}	100	3.0	4.0	0.6

Experimental measurements were made of the luminescence intensities of Er^{3+} ions for the $^4I_{13/2} \rightarrow {}^4I_{15/2}$ and $^4I_{11/2} \rightarrow {}^4I_{15/2}$ transitions, and the luminescence decay time under pulsed excitation was also measured.

The samples had the same thickness ($L \cong 2$ mm), but different compositions and concentrations of rare-earth elements.

An increase in the concentration of Er^{3+} ions (for single-component doping) from 1 to 6 mol.% was accompanied by

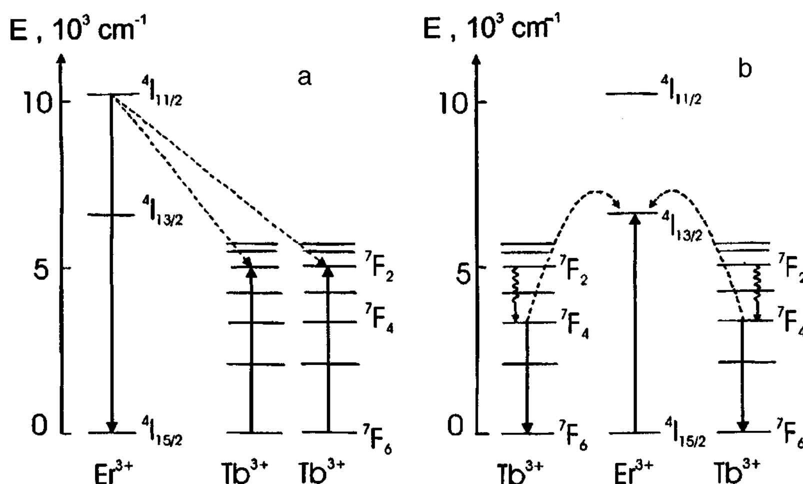

FIG. 1. a — Cross relaxation of Er^{3+} ion involving Tb^{3+} ions; b — cooperative filling of the $^4I_{13/2}$ level of the Er^{3+} ion.

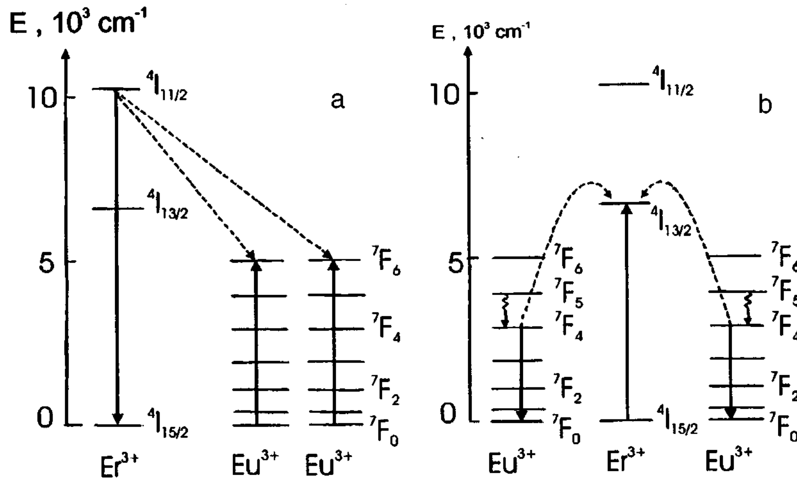

FIG. 2. a — Cross relaxation of Er^{3+} ion involving Eu^{3+} ions; b — cooperative filling of the $^4I_{13/2}$ level of the Er^{3+} ion.

an increase in the luminescence intensity in both bands. The intensities of the $\lambda=1.54$ μm and $\lambda=0.98$ μm luminescence are denoted by I_1 and I_2, respectively, with the ratio $K=I_1/I_2\cong 0.3$. The decay time of the $\lambda=0.98$ μm luminescence (τ_2) decreased from 6 to 5 ms, while that at $\lambda=1.54$ μm (τ_1) decreased from 10 to 9 ms (see Table I).

The addition of 3 mol.% Yb^{3+}, which is a donor, increased the intensity of the long-wavelength luminescence band to approximately the same level as that for 6% doping. However, most of the pump energy was re-emitted in the short-wavelength band.

In a sample containing 1% $Er^{3+}+1\%\,Eu^{3+}$, the intensity of the long-wavelength luminescence band began to predominate over the short-wavelength one ($K=1.2$).

The best results were obtained in a three-component system containing 1% $Er^{3+}+3\%\,Yb^{3+}+0.5\%\,Tb^{3+}$ with the ratio $K=3$. The decay time of the $\lambda=1.54$ μm emission decreased to $\tau_1=4$ ms. The decay time of the $\lambda=0.98$ μm luminescence decreased abruptly to $\tau_2=0.6$ ms (Figs. 1a and 2a).

According to the energy level diagram (Fig. 1), the states in which Tb^{3+} and Eu^{3+} ions can participate in interionic interactions have a lower energy than the Er^{3+} ion in the $^4I_{13/2}$ state. Thus, this state cannot be filled by a donor–acceptor scheme.

It is possible that ions accumulate in the $^5D_4$ metastable level as a result of cooperative pumping. Decay of this state involving Er^{3+} ions would lead to filling of the $^4I_{11/2}$ state, which would be accompanied by an increase in the lifetime of the Er^{3+} ions in this level.

In our experiments we observed a sharp drop in the decay time and a reduction in the luminescence intensity of the short-wavelength Er^{3+} band in samples Nos. 4 and 5 when Tb^{3+} ions and Eu^{3+} ions were incorporated. This indicates that the above mechanism does not take place. It is more likely that Er^{3+} ions undergo cross relaxation from the $^4I_{11/2}$ state with energy transfer to the $^7F_2$ and $^7F_6$ excited states of the Tb^{3+} or Eu^{3+} ions, respectively (Figs. 1a and 2a). The small energy gaps not exceeding 1000 cm^{-1} between the lower levels of these ions ensure intra-ionic transitions involving one or two matrix phonons to the $^7F_4$ and $^7F_5$ levels.

The subsequent summation of the energy of two ions in these states may result in cooperative excitation of a single Er^{3+} ion to the $^4I_{13/2}$ level (Figs. 1b and 2b).

The resonance relations are best satisfied for the $^4I_{13/2}$ levels of the Er^{3+} ion and the $^7F_4$ level of the Tb^{3+} ion, which may be responsible for the high luminescence yield at $\lambda=1.54$ μm in the sample having the composition 1% $Er^{3+}+3\%\,Yb^{3+}+0.5\%\,Tb^{3+}$.

The authors would like to than N. B. Zvonkov for supplying the semiconductor laser and for his cooperation.

This work on energy transfer processes in rare-earth-doped fluorozirconate glasses was supported by the Russian Fund for Fundamental Research (Grant No. 96-02-16996a).

[1] Y. Miyajima, T. Komukai, T. Sugawa, and T. Yamamoto, Opt. Fiber Technol. **1**(1), 35 (1994).
[2] F. E. Ozel', Proc. IEEE No. **6,** 87 (1973).
[3] I. A. Grishin, V. A. Gur'ev, V. L. Mart'yanov, and A. P. Savikin, Pis'ma Zh. Tekh. Fiz. **23**(2), 51 (1997) [Tech. Phys. Lett. **23**, 70 (1997)].

Translated by R. M. Durham
Edited by David L. Book

Influence of moisture on the properties of long streamers in air

N. L. Aleksandrov, É. M. Bazelyan, and D. A. Novitskiĭ

Moscow Physicotechnical Institute;
G. M. Krzhizhanovskiĭ Power Institute, Moscow
(Submitted November 21, 1997)
Pis'ma Zh. Tekh. Fiz. **24**, 86–91 (May 12, 1998)

A simulation has shown that the suppression of streamer propagation with increasing air moisture content discussed repeatedly in the literature is caused by accelerated electron–ion recombination rather than by the kinetics of the negative ions, as was previously assumed.
© *1998 American Institute of Physics.* [S1063-7850(98)01605-X]

Streamer propagation is an important discharge phase in the breakdown of long gas gaps. The question as to how the characteristics of streamers in air vary with changes in the moisture content has been addressed for several decades (see, for example, Ref. 1). This topic has recently attracted increased interest because of the use of streamer coronas and barrier discharges to remove oxides of nitrogen and sulfur from flue gases in which the water content may reach 20% (Ref. 2).

Experiments have shown that an increase in the moisture content in air impedes the evolution of streamers.[1,3,4] This takes the form of a reduction in the size of the streamer corona, a reduction in the electric charge transported by the streamers, and an increase in the average field required for a streamer corona to cover a gap of given length. The strength of this field has repeatedly been measured for various electrode configurations, interelectrode gaps, applied pulse profiles, air pressure, and moisture content (see, for example, Refs. 5 and 6).

According to current thinking, the main reason for the observed behavior is an enhanced loss of electrons in the process

$$e+O_2+M\rightarrow O_2^-+M, \quad (1)$$

which is assumed to be the main mechanism for their removal in the streamer channel. The rate constant of process (1) for $M=H_2O$ is approximately ten times higher than that for $M=O_2$ (Refs. 7 and 8). A decrease in the rate of electron detachment from negative ions in the streamer channel has also been indicated as a possible factor which impedes the evolution of streamers in moist air.[1,9]

Although this topic has been discussed repeatedly in the literature, so far no quantitative theoretical studies have been made. Thus, the assumptions put forward as to the mechanism responsible for the influence of moisture on the properties of streamers are merely hypotheses based only on rough qualitative estimates.

The aim of the present study was to make a numerical simulation of a long positive streamer in air under normal conditions as a function of its moisture content. To do this we used the 1.5-D streamer model, which assumes that the streamer channel has a constant radius, and we used a fairly detailed model of ion-molecular processes. These models were described for dry air in Refs. 10–12. The main difference between the present model and that used earlier is that it takes into account reactions involving components produced as a result of the presence of water vapor in the air. These include H_2O molecules, OH radicals, and $O_2^+ + H_2O$, H_2O^+, $H_3O^+(H_2O)_n$ $(n=0-3)$, $O_2^-(H_2O)_n$ $(n=1,2)$, and $OH^-(H_2O)_n$ $(n=0-2)$ ions. The additional processes include reaction (1) with $M=H_2O$, ion-molecular conversion reactions of positive and negative ions, decomposition of negative ions, and electron–ion and ion–ion recombination. The rate constants of these reactions were taken from Refs. 7, 8, 13, 14, 15, and 16. The rates of electron impact ionization of H_2O molecules and dissociative attachment of electrons to these molecules were assumed to be the same as for O_2 molecules. This is valid for the moderate H_2O concentrations considered here.

The calculations simulated a streamer directed toward the cathode in gaps with abruptly nonuniform and uniform electric field distributions. In the first case, an isolated spherical anode of radius 1 cm was used and the length of the gap covered by the streamer reached 20 cm. In the second case, the streamer was formed between planar electrodes. The situation was simulated where the streamer started from a short zone of locally intensified field which was created by a sphere of 0.1 cm radius, positioned 10 cm from the planar cathode. To this sphere we applied an additional positive voltage of 12 kV relative to the cathode (around 10% of the total voltage across the gap), so that the sphere functioned as the anode. Even when the channel was ∼0.5 cm long, the streamer left the section of the gap perturbed by the spheres and propagated into the region of external uniform field. The radius of the streamer channel was assumed to be 0.03 cm. This shows good agreement between the calculations and the measurements of the electric field required for streamers to cover long gaps in dry air.[17]

Figure 1 gives results of calculations of the average electric field required for a streamer to cover these gaps as a function of the water vapor partial pressure. Also plotted are experimental data[5] obtained under similar conditions for uniform gaps 9 cm long, which show good agreement with the results of other measurements (see, for example, Ref. 6). The agreement between the calculations and the experiment suggests that on the whole, the model used accurately takes into

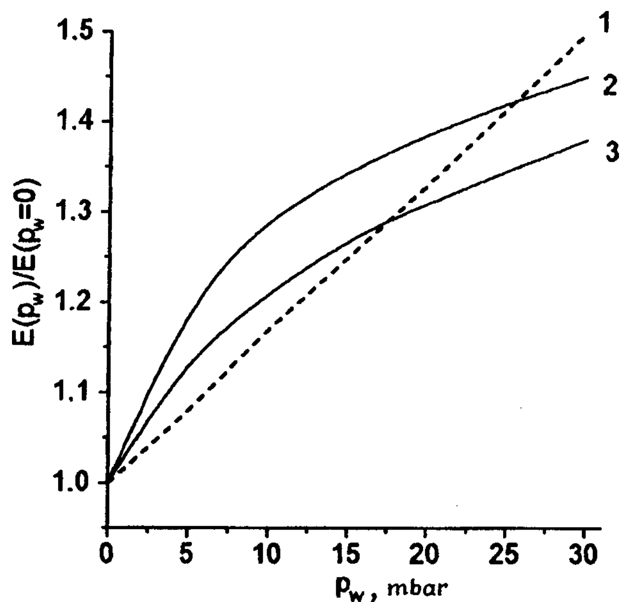

FIG. 1. Electric field required to cover discharge gap as a function of water vapor partial pressure in air: *1* — experiments reported in Ref. 5, *2* — calculations for a 10 cm long streamer in a uniform field, and *3* — calculations for a 20 cm long streamer in an abruptly uniform field.

account the main relationships associated with the increased air moisture and can be used to analyze the mechanism responsible for the influence of moisture on the properties of long streamers in air.

Figure 2 shows typical times dependences of the electron density n_e and the electron loss frequencies in the streamer channel. In this case, at a partial water pressure $p_w = 15$ mbar, the streamer started from a spherical anode of 1 cm radius at a voltage of 115 kV sufficient to form a channel 20 cm long. The calculation point was 5.7 cm from the anode. It can be seen from Fig. 2 that n_e and the conductivity of the streamer channel decreased mainly because of electron–ion recombination. An increase in moisture content is accompanied by an increase in the fraction of hydrated ions, for which the rate of electron recombination is higher than that for ions in dry air.[14–16] Thus, the conductivity of the streamer channel and the potential of the streamer head, where the ionization zone is situated, decrease more rapidly. As a result, the external field required for the streamer to cover the gap increases.

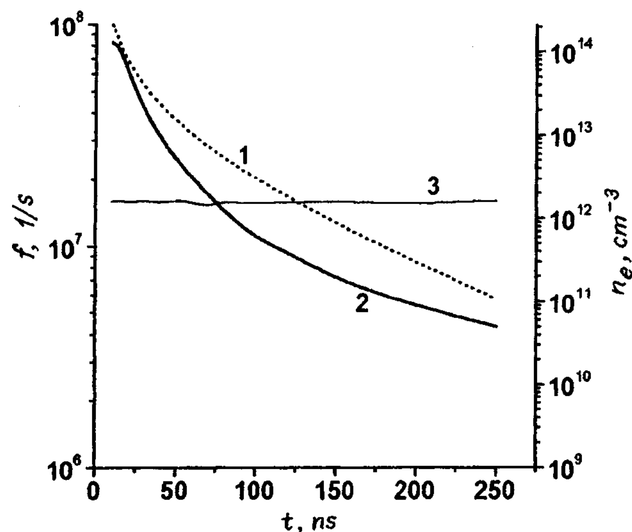

FIG. 2. Time dependence of the electron density (curve *1*), the electron loss frequency in the streamer channel as a result of dissociative recombination with hydrated ions (curve *2*), and process (1) with $M = H_2O$ (curve *3*).

The rate of process (1) also increases with increasing moisture content in the air. However, the calculations show that the formation of negative ions can only become an important factor at the later stages of streamer channel decay, by which time the density n_e and conductivity of the streamer channel can decrease by almost two orders of magnitude.

The importance of electron recombination with hydrated ions and the insignificance of attachment processes is indicated by the numerical experiments in which the calculation model completely eliminated either hydration reactions of positive ions or reaction (1) with $M = H_2O$. The first calculations almost completely negated the effect of moisture content, giving only a 6.5% increase in the average field compared with ideal dry air at a partial pressure of 15 mbar. In the second case, the effect of moisture remained almost the same, decreasing from 27% to 22%.

To sum up, the simulation performed here indicates that the frequently observed more rapid slowing of long streamers in moist air is not caused by the kinetics of the negative ions in the channel, as was previously assumed. It is attributable to the hydration of positive ions, which speeds up electron–ion recombination and the loss of conductivity of the streamer channel.

This work was supported by the State Committee for Higher Education of the Russian Federation (Grant No. 95-0-5.2-147).

[1] I. Gallimberti, J. Phys. (Paris) **40**, C7, 193 (1979).
[2] *Non-Thermal Plasma Techniques for Pollution Control*, edited by B. M. Penetrante and S. E. Schultheis, NATO ASI Series, Series G: Ecological Sciences, Vol. 34, Part B (Springer-Verlag, Berlin, 1993).
[3] Les Renardieres Group, Electra No. 53, 5 (1977).
[4] R. T. Waters, in *Electrical Breakdown in Gases*, edited by J. M. Meek and J. D. Craggs (Wiley, New York, 1978), pp. 385–532.
[5] C. T. Phelps and R. F. Griffiths, J. Appl. Phys. **47**(7), 2929 (1976).
[6] N. L. Allen and M. Boutlendj, Proc. IEEE **138**, 37 (1991).
[7] B. M. Smirnov, *Negative Ions* (Atomizdat, Moscow, 1978; McGraw–Hill, New York, 1982).
[8] N. L. Aleksandrov, Usp. Fiz. Nauk **154**, 177 (1988) [Sov. Phys. Usp. **31**, 101 (1988)].
[9] J. J. Lowke, J. Phys. D **25**, 202 (1992).
[10] A. É. Bazelyan and É. M. Bazelyan, Teplofiz. Vys. Temp. **31**, 867 (1993).
[11] N. L. Aleksandrov, A. É. Bazelyan, É. M. Bazelyan *et al.*, Fiz. Plazmy **21**, 60 (1995) [Plasma Phys. Rep. **21**, 57 (1995)].
[12] N. L. Aleksandrov and E. M. Bazelyan, J. Phys. D **29**, 740 (1996).
[13] M. J. McEwan and L. F. Phillips, *The Chemistry of the Atmosphere* (Halsted Press, New York, 1975; Mir, Moscow, 1978).
[14] B. M. Smirnov, *Cluster Ions and Van der Waals Molecules* (Nauka, Moscow, 1983; Gordon & Breach, Philadelphia, 1992).
[15] J. B. A. Mitchell, Phys. Rep. **186**, 215 (1990).
[16] R. Johnsen, J. Chem. Phys. **98**, 5390 (1993).
[17] N. L. Aleksandrov and E. M. Bazelyan, J. Phys. D **29**, 2873 (1996).

Translated by R. M. Durham
Edited by David L. Book

Influence of the ''matrix memory'' effect on the photodecay of dye molecules adsorbed in porous glass

V. N. Beger

St. Petersburg State Institute of Precision Mechanics and Optics (Technical University)

(Submitted September 16, 1997)
Pis'ma Zh. Tekh. Fiz. **24**, 92–95 (May 12, 1998)

Photodecay quantum yields were determined experimentally for several laser dyes adsorbed in porous silicate glass at various dye concentrations. It was observed that the efficiency of photodecay of the adsorbed molecules depends on the method of incorporating the dyes in the porous matrices, especially on the type of solvent used when introducing the dye into the porous glass from solution, with subsequent removal of the solvent. © *1998 American Institute of Physics.* [S1063-7850(98)01705-4]

The photostability of laser dyes in porous silicate glasses[1–4] is one of the most important parameters of these media and determines the potential usefulness of these dyes as solid-state active elements of tunable lasers. It was observed previously that the photodecay efficiency of dye adsorbates is frequently very sensitive to intermolecular interactions. In particular, the photodecay quantum yield of dye molecules adsorbed in porous glass exhibited a strong concentration dependence[4] which may indicate that inductive resonant interactions between adsorbed molecules have an appreciable influence on the intramolecular parameters responsible for the stability of a molecule under electronic excitation.

However, it is well known that the surface of the pores in porous glass is extremely inhomogeneous and as a result, the electronic spectra of dye adsorbates (many of which possess significant solvatochromism and solvatofluorochromism) in these matrices exhibit appreciable inhomogeneous broadening.[5] Since variations in the interactions between adsorbed molecules and adsorbent should not only influence the position of the energy levels of the adsorbed molecules but also their photostability, it is quite natural to assume that the experimentally determined photodecay quantum yields of dye molecules in porous glass reflect average values, which characterize an inhomogeneous ensemble of adsorbate molecules as a whole. At the same time, the actual photostability of individual molecules adsorbed on sections of surface with different properties (for instance, on sections with different local curvature) should vary appreciably.

It has also been observed that the distribution of adsorbed dye molecules over an inhomogeneous surface, obtained when dye solutions are introduced into porous glass, first depends very much on the solvent used and second, is frequently conserved after the solvent has been removed from the pores because of the very low diffusion mobility of dye molecules in ''dry'' matrices.[6,7] This long-lived conservation of a nonequilibrium distribution of adsorbed molecules on an inhomogeneous surface in ''dry'' matrices is responsible for the ''matrix memory'' effects observed earlier.[6,7] With this in mind, it is quite natural to assume that matrix memory effects should also be observed for the photodecay efficiency in an inhomogeneous ensemble of adsorbate molecules. Thus, the aim of the present study was to examine how the method of introducing dyes into porous glass influences the photostability of the adsorbates.

An investigation was made of the photostability of several laser dyes (oxazine 17, coumarin 7, and coumarin 30) introduced into porous glass from various solvents (heptane, toluene, ethanol) for various concentrations of dye molecules in the porous matrices. In order to determine the photodecay quantum yield q, the dye was ''burnt out'' by laser radiation at a wavelength in the absorption band of the dye and the dynamics of the optical density $D(t)$ of the samples measured as a function of time. Helium–neon laser radiation at 632.8 nm was used for oxazine 17 and 488.0 nm argon laser radiation for coumarin 7 and coumarin 30. In all cases the power density of the laser radiation incident on the samples wasless than 100 mW/cm^2. The results (values of q calculated using the $D(t)$ data by a method described in Ref. 4) are given in Table I. It can be seen that the photostability of the dye adsorbates depended on the method of introducing the dyes into the porous glass. The lowest photostability is exhibited by adsorbates obtained by introducing dyes into porous glass from solvents having the highest Henry constant for that particular dye (this constant characterizes the equilibrium ratio of concentrations of adsorbed molecules and molecules in the dye solution introduced into the matrix pores).

It was noted earlier,[6] that using dye solutions based on solvents with high Henry constants leads to the formation of adsorbates whose electronic spectra exhibit relatively weak inhomogeneous broadening and preferential adsorption of molecules on sections of the surface having the highest adsorption energy. Solutions with low Henry constants form more inhomogeneous ensembles of adsorbed molecules in porous glass, with dye molecules distributed over sections of the surface with both high and low adsorption energies. Note that sections of the pore surface with the maximum local curvature are the most effective for physical adsorption (which predominates for the dye molecules used in these

 © 1998 American Institute of Physics

TABLE I. Photodecay quantum yields of dye molecules adsorbed in porous glass as a function of method of incorporating dye into porous matrix.

Dye	Concentration of dye molecule in matrix, cm^{-3}	Incorporation of dye into matrix from following solutions:		
		Ethanol	Toluene	Heptane
Oxazine 17	5×10^{16}	8 ± 2	12 ± 3	15 ± 3
	10^{17}	15 ± 3	23 ± 4	30 ± 6
	2×10^{17}	36 ± 6	53 ± 6	70 ± 10
Coumarin 7	5×10^{16}	8 ± 2	10 ± 2	14 ± 3
	10^{17}	18 ± 4	25 ± 4	35 ± 6
	2×10^{17}	45 ± 8	60 ± 6	85 ± 10
Coumarin 30	5×10^{16}	9 ± 2	12 ± 3	15 ± 3
	10^{17}	20 ± 4	26 ± 4	30 ± 6
	2×10^{17}	45 ± 8	65 ± 8	75 ± 10

matrices). It is also possible that the adsorption of fairly large polyatomic molecules on these parts of the surface is accompanied by a particular type of molecular deformation, which not only reduces the fluorescence quantum yield[7] but also enhances the probability of molecular decay under electronic excitation.

Note that an increase in the concentration of adsorbed molecules not only increased the photodecay quantum yields of the adsorbate molecules (this effect was observed in Ref. 4) but also had the result that the photostability of the adsorbed molecules depended more strongly on their method of incorporation into the porous glass. It is quite likely that the use of different solvents produces different types of spatial distribution of the adsorbed molecules, which may have different fractal dimensions (it was observed earlier that the distribution of dye molecules in the bulk of porous glass is a fractal distribution, frequently with an extremely low fractal dimension).[8,9] An important factor is that for the same concentrations of adsorbed molecules but different fractal dimensions characterizing their spatial distribution in the bulk of the adsorbent, the probability of nonradiative transfer of electronic excitation energy differs. Thus, the probability of electronic excitation energy being transferred to the least stable molecules in an inhomogeneous ensemble is also different.

[1] G. B. Al'tshuler, E. G. Dul'neva, I. K. Meshkovskiĭ, and K. I. Krylov, Zh. Prikl. Spektrosk. **36**, 592 (1982).
[2] V. I. Zemskiĭ and I. K. Meshkovskiĭ, Pis'ma Zh. Tekh. Fiz. **9**, 1029 (1983) [Sov. Tech. Phys. Lett. **9**, 442 (1983)].
[3] K. K. Boyarskiĭ, A. Yu. Vorob'ev, V. I. Zemskiĭ, Yu. L. Kolesnikov, and I. K. Meshkovskiĭ, Opt. Spektrosk. **65**, 909 (1988) [Opt. Spectrosc. **65**, 536 (1988)].
[4] V. N. Beger, Pis'ma Zh. Tekh. Fiz. **18**(21), 29 (1992) [Sov. Tech. Phys. Lett. **18**, 700 (1992)].
[5] V. I. Zemskiĭ, A. V. Sechkarev, I. G. Stuklov, and G. B. Deĭneka, Opt. Spektrosk. **69**, 1024 (1990) [Opt. Spectrosc. (USSR) **69**, 607 (1990)].
[6] V. N. Beger and A. V. Sechkarev, Pis'ma Zh. Tekh. Fiz. **17**(19), 83 (1991) [Sov. Tech. Phys. Lett. **17**, 712 (1991)].
[7] V. N. Beger, Pis'ma Zh. Tekh. Fiz. **18**(11), 27 (1992) [Sov. Tech. Phys. Lett. **18**, 347 (1992)].
[8] V. N. Beger, V. I. Zemskiĭ, Yu. L. Kolesnikov, I. K. Meshkovskiĭ, and A. V. Sechkarev, Opt. Spektrosk. **66**(1), 120 (1989) [Opt. Spectrosc. **66**, 69 (1989)].
[9] A. V. Sechkarev and V. N. Beger, Izv. Ross. Akad. Nauk Ser. Khim. No. 7, 1284 (1995).

Translated by R. M. Durham
Edited by David L. Book

Interrelation between the resistance of Gunn diodes in weak electric fields and the characteristics of oscillators based on them

D. A. Usanov, A. V. Skripal', and A. V. Babayan

Saratov State University

(Submitted June 3, 1997; resubmitted January 9, 1998)
Pis'ma Zh. Tekh. Fiz. **24**, 1–7 (May 26, 1998)

A theoretical description is given of an experimentally established dependence which determines the interrelation between the resistance of a semiconductor structure in weak electric fields and the characteristics of Gunn oscillators. This experimentally established dependence is of considerable practical value since it can be used to predict the main characteristics of diode microwave oscillators using easily measured parameters of dc diodes. © *1998 American Institute of Physics.* [S1063-7850(98)01805-9]

It is known that the output power and long-term power and frequency instability of Gunn oscillators differ substantially when different Gunn diodes of the same type are used in the same oscillator design, with the same power supply. It has been established[1] that this difference is caused by a spread of the diode parameters in terms of their resistance in weak electric fields, which in turn may be caused by uncontrollable factors in the fabrication process of the diode structures. The experimental results also indicate that attempts to increase the output power of Gunn oscillators by using low-resistivity diodes substantially increase the long-term power and frequency instability of the oscillators. This experimentally determined dependence is of considerable practical value since it makes it possible to predict the main characteristics of diode microwave oscillators from easily measured dc parameters of diodes. However, no theoretical description has been put forward for the interrelation between the resistance of a semiconductor structure in weak electric fields and the characteristics of Gunn diode oscillators, which has made it difficult to understand the physical factors responsible for this behavior.

In order to understand this interrelation, the physical processes in a Gunn diode were analyzed by simultaneously solving the system of Kirchhoff equations[2] and the time-dependent heat balance equation, expressed in the form[3]

$$C_m \frac{dT}{dt} = i(U,T)U - \frac{T-T_0}{R_T},$$

where T and T_0 are the temperature of the diode crystal and the surrounding medium, respectively, R_T is the total thermal resistance of the device, and C_m is the specific heat of the semiconductor crystal. For the calculations we used the typical current–voltage characteristic $i(U,T)$ of a Gunn diode,[4] which was approximated by the expression[2,5]

$$i = R_0^{-1} \frac{d}{\mu(T)} \times \frac{\mu(T)(U+D)/d + V_s(T)[(U+D)/U_n]^4}{1+[(U+D)/U_n]^4},$$

where $R_0 = [qn_0\mu(T)S/d]^{-1}$ is the resistance of the semiconductor structure in weak electric fields, n_0 is the concentration of completely ionized donors, S and d are the effective cross-sectional area and length of the diode, respectively, $D=0$ for $U \leqslant U_n$, $D=2$ for $U > U_n$,

$$\mu(T) = 300\mu_0/T,$$

$$V_S(T) = V_0/[T(1-53\times10^{-4}T)].$$

This model was used to calculate the transient processes leading to the establishment of steady-state operation of a Gunn oscillator with allowance for self-heating. Figure 1 gives the output power P, the variation of the dc current Δi in the power supply to the Gunn diode, and the temperature of the diode crystal T as a function of the time t after application of a fixed bias for diodes with various values of the resistance R_0 and thermal resistance R_T. It can be seen from the results of the calculations plotted in Fig. 1 that the power generated by a Gunn diode and the variation of the dc current in the steady-state regime increase and the resistance R_0 and thermal resistance R_T decrease.

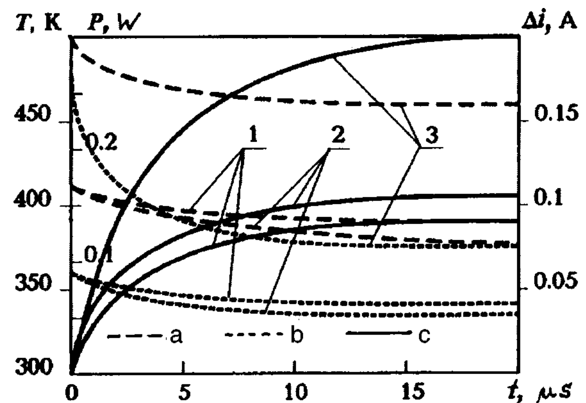

FIG. 1. Output power (a), variation of dc current in supply circuit to Gunn diode (b), and diode temperature (c) as a function of time t after application of a fixed bias for diodes with different resistances R_0 and thermal resistance R_T: *1*—$R_0=10\ \Omega$, $R_T=100$ deg/W, *2*—$R_0=10\ \Omega$, $R_T=150$ deg/W, *3*—$R_0=5\ \Omega$, $R_T=100$ deg/W.

 © 1998 American Institute of Physics

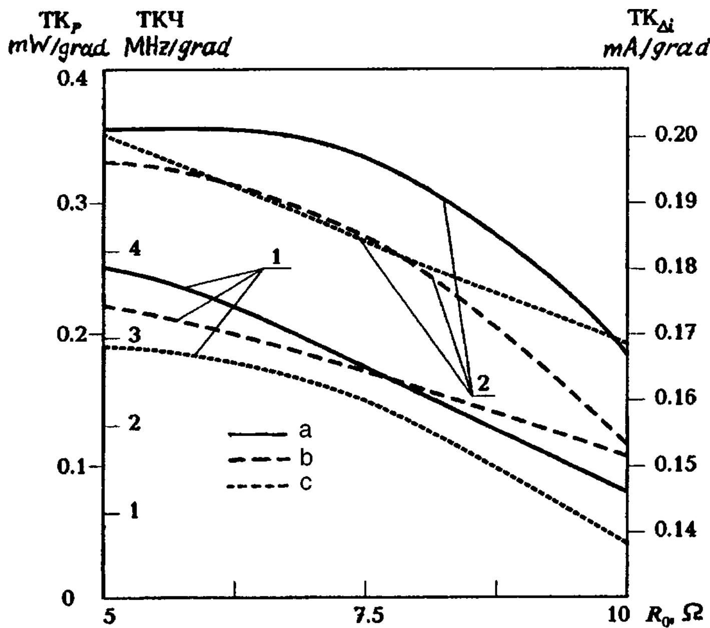

FIG. 2. Absolute values of TCF (a), TC_P (b), and TC_{Δ_i} (c) versus diode resistance R_0 for various values of the thermal resistance R_T: *1* — R_T= 150 deg/W, *2* — R_T= 100 deg/W.

Calculations of the temperature coefficients of frequency ($\mathrm{TCF}=\Delta f/\Delta T$), power ($\mathrm{TC}_P=\Delta P/\Delta T$), and current variation ($\mathrm{TC}_{\Delta i}=\Delta i/\Delta T$) showed that the absolute values of the long-term instability of the main characteristics, caused by changes in the temperature of the surrounding medium, decrease as the thermal resistance R_T and R_0 increase. Figure 2 gives the absolute values of TCF, TC_P, and $\mathrm{TC}_{\Delta i}$ as a function of the diode resistance R_0 for various values of the thermal resistance R_T.

In order to determine the long-term instability of the output signal characteristics of a Gunn oscillator caused by changes in the heat transfer conditions, we calculated the modulation sensitivity with respect to the thermal resistance of the frequency ($\Delta f/\Delta R_T$), the power ($\Delta P/\Delta R_T$), and the change in the dc current in the Gunn diode power supply ($\Delta i/\Delta R_T$), which showed that the absolute values of the oscillator modulation sensitivity with respect to the thermal resistance decrease as the ambient temperature and the diode resistance R_0 increase.

A comparison between the calculated data and the experimental results given in Ref. 1 reveals qualitative agreement. The results of the calculations indicate that quantitative agreement is achieved in determinations of the long-term instability of the oscillator characteristics if simultaneous allowance is made for the action of several destabilizing factors, taking into account their signs, such as changes in the heat transfer conditions R_T and the ambient temperature T_0. Determining the interrelation between these parameters in a real device is a separate, fairly complicated problem.

It should also be noted that the quantitative changes in the long-term instability of the characteristics of a Gunn oscillator depend on the factors responsible for the change of the diode resistance R_0. For example, a decrease in R_0 by a factor of two as a result of an increase in $\mu(T)$ doubles the instability of the output signal characteristics of the oscillator compared with a similar decrease in R_0 caused by an increase in S or n_0. The calculations show that this is because the self-heating of the diode crystal accompanying an increase in μ is less intensive than that caused by a similar increase in S or n_0. It should also be borne in mind that an increase in S or n_0 causes a more significant increase in the output power of the emitted radiation compared with an increase in $\mu(T)$.

The results of experimental investigations reported in Ref. 1 indicate that when a pulsed power supply is used, the oscillator output characteristics are less unstable than when the oscillator is supplied by a dc voltage source.

Results of calculations of the diode crystal temperature as a function of time when the diode is exposed to a rectan-

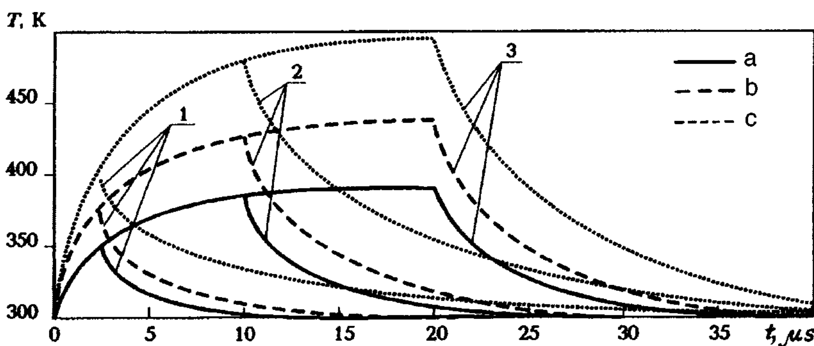

FIG. 3. Temperature of Gunn diode crystal versus time when the crystal is exposed to a rectangular supply pulse of different length τ_P, *1*—2.5 μs; *2*—10.0 μs; 3—20.0 μs. *a*—$n_0=1\times10^{15}$ cm^{-3}, R_T= 100 deg/W; *b*—$n_0=2\times10^{15}$ cm^{-3}, R_T= 100 deg/W; *c*—$n_0=2\times10^{15}$ cm^{-3}, R_T= 150 deg/W.

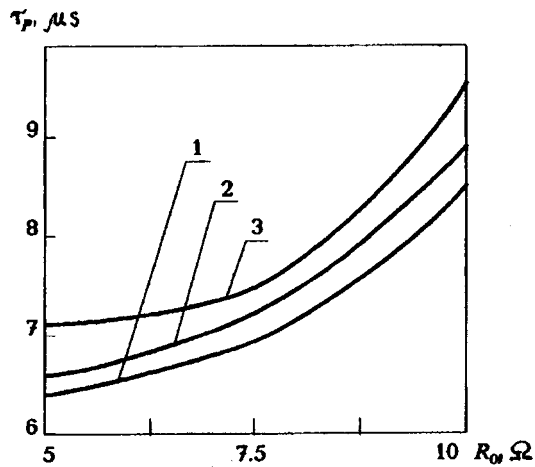

FIG. 4. Maximum length of supply pulse τ_P for which the output signal from the Gunn oscillator reaches a specific level of instability as a result of changes in the heat transfer conditions and the ambient temperature, as a function of the diode resistance R_0: *1* — $T_0=290$ K, *2* — $T_0=300$ K, and *3* — $T_0=310$ K.

gular supply pulse for various values of R_0 and R_T and pulse length τ_p are plotted in Fig. 3. The minimum pulse repetition period for which cooling takes place, increases with increasing pulse length. This dependence is appreciably stronger if τ_p is comparable with the cooling time.

As a result of the calculations, it was also established that the maximum supply pulse length τ_p, for which the instability of the output signal from a Gunn oscillator reaches a specific level as a result of changes in the heat transfer conditions and ambient temperature (Fig. 4), increases as the resistance of the semiconductor diode structure increases.

To sum up, the experimentally observed interrelation between the resistance of diodes in weak electric fields and the characteristics of microwave oscillators based on these diodes has been described by modeling the electrical and thermophysical parameters of Gunn diodes. This allows the main characteristics of diode microwave oscillators to be predicted from easily measured parameters of dc diodes.

The results indicate in particular that by using diodes with low R_0 consistent with τ_p, the maximum output power can be increased with the level of signal instability remaining the same.

[1] D. A. Usanov, A. V. Skripal', and A. A. Avdeev, Zh. Tekh. Fiz. **65**(10), 197 (1995) [Tech. Phys. **40**, 1084 (1995)].
[2] D. A. Usanov, A. V. Skripal', A. A. Avdeev, and A. V. Babayan, Radiotekh. Elektron. **46**, 1497 (1996).
[3] M. I. Bil'ko, A. K. Tomashevskiĭ, P. P. Sharov, and E. A. Baĭmuratov, *Microwave Power Measurements* [in Russian], Sovetskoe Radio, Moscow (1976).
[4] K. Murayama and T. Ohmi, Jpn. J. Appl. Phys. **12**, 1931 (1973).
[5] P. J. Mulmom, G. S. Hobson, and B. C. Taylor, *Transferred Electron Devices* (Academic Press, New York, 1972).

Translated by R. M. Durham
Edited by David L. Book

Influence of potassium and fluorine on the formation and properties of the high-temperature 2223 phase in a (Bi, Pb)-Sr-Ca-Cu-O system

V. V. Petrashko, N. D. Zhigadlo, B. V. Novysh, Yu. A. Semenenko, N. A. Prytkova, and V. P. Yarunichev

Institute of Solid-State and Semiconductor Physics, Belarus Academy of Sciences, Minsk

(Submitted November 11, 1997)
Pis'ma Zh. Tekh. Fiz. **24**, 8–15 (May 26, 1998)

An investigation was made of how the partial replacement of oxygen with fluorine and of strontium with potassium influences the formation and properties of the superconducting phases in a (Bi,Pb)–Sr–Ca–Cu–O system. It was established that simultaneous anion–cation substitutions have a positive influence, speeding up the formation of the 2223 high-temperature phase. © *1998 American Institute of Physics.* [S1063-7850(98)01905-3]

The fluorination of oxide superconductors in a (Bi, Pb)–Sr–Ca–Cu–O system promotes the formation of the 2223 high-temperature superconducting phase (see Ref. 1 and the literature cited), increases $T_c(R=0)$ (Refs. 1 and 2), and improves other physical properties.[3] However, the use of different fluorine-containing reagents leads to variations in the properties.[2,4,5] The technology required to produce superconducting materials with highly reproducible stable properties has not yet been developed.

We have already established that the addition of potassium to samples having the composition $Bi_{1.7}Pb_{0.3}Sr_2Ca_2Cu_3O_y$ helps to increase $T_c(R=0)$ and $j_c(77\ K)$ (Ref. 6). In Ref. 7 we obtained $T_c(R=0)=112.8$ K for samples having the composition $Bi_{1.6}Pb_{0.4}Sr_{1.98}K_{0.02}Ca_2Cu_3F_{0.8}O_y$.

Here we report an investigation of the influence of potassium and fluorine on the formation of superconducting phases in a bismuth system, and on the variation of its physical properties.

Samples having the nominal composition $Bi_{1.6}Pb_{0.4}Sr_{2-x}K_xCa_2Cu_3F_zO_{y-z}$ ($x=0$, 0.02, 0.05; $z=0$, 0.8) were prepared by solid-phase synthesis in air using a mixture of Bi_2O_3, PbO, $SrCO_3$, $CaCO_3$, CuO, K_2CO_3, and PbF_2 powder. The mixed and ground powder was calcined for 16 h at 750 °C. The calcined powder was crushed and pressed into pellets 12.8 mm in diameter which were initially annealed for 69.5 h at between 820 and 827 °C and then, after repeated crushing and pressing, the actual synthesis was performed at 838° for 190 h. The phase composition of the ground powder samples was investigated using a DRON-4-07 diffractometer, using CuK_α radiation. The superconducting properties of the samples were studied by measuring the resistive and current–voltage characteristics. The temperature dependence of the electrical resistivity and the critical current density at liquid nitrogen temperature was measured using a dc four-probe method. The criterion for the critical current was 1 μV/cm.

Figure 1 shows diffraction patterns obtained from ground pellets for samples synthesized for 69.5 h at temperatures between 820 and 827 °C and then cooled inside the furnace. For all samples, regardless of the fluorine and potassium content, the 2212 phase is the main superconducting phase. The 2201, Ca_2PbO_4, and $(Sr,Ca)_2CuO_3$ phases are detected as impurity phases, and negligible amounts of the 2223 phase are identified. It can be seen from Fig. 1 that under these synthesis conditions, partial replacement of oxygen with fluorine and strontium with potassium has no significant influence on the formation and growth of the 2212 superconducting phase, although the partial substitution of divalent strontium with monovalent potassium promotes accelerated growth of the Ca_2PbO_4 and $(Sr,Ca)_2CuO_3$ phases in samples having the stoichiometric composition $Bi_{1.6}Pb_{0.4}Sr_{2-x}K_xCa_2Cu_3F_{0.8}O_y$.

Figure 2 shows diffraction patterns of samples synthesized at 838 °C for 190 h. It can be seen that the samples have multiphase structures. The phase content depends on the type and amount of additive. The main phases are the superconducting 2223 (dominant) and 2212 phases. The relative volume fractions of these superconducting phases (neglecting other nonsuperconducting phases), determined from the intensities of the 002 diffraction peaks using the ratio $[H(002)\text{ or }L(002)]/[H(002)+L(002)]$, where H and L are the intensities of the high-temperature (2223) and low-temperature (2212) phases, respectively, are given in Table I. It can be seen from Table I and Fig. 2 that the volume fraction of the 2223 phase increases substantially, from 72% to 85%, when some of the oxygen in the initial sample is replaced with fluorine. An even greater increase in the volume fraction of the 2223 phase is observed when oxygen is partially replaced with fluorine, and strontium is replaced with potassium (Figs. 2c and 2d). As the potassium concentration is increased from $x=0.02$ to $x=0.05$, the volume fraction of the 2223 phase increases from 90 to 93% and the content of the 2212 phase decreases.

In addition to the main superconducting phases (2223 and 2212), all the samples contain the 2201 and Ca_2PbO_4 phases as impurities, but their content is much lower than that in samples synthesized at temperatures between 820 and 827 °C. The content of the Ca_2PbO_4 phase in samples containing fluorine and potassium is slightly lower than that in the initial sample containing no potassium or fluorine (Fig. 2). After synthesis at 838 °C, very small quantities of the

 © 1998 American Institute of Physics

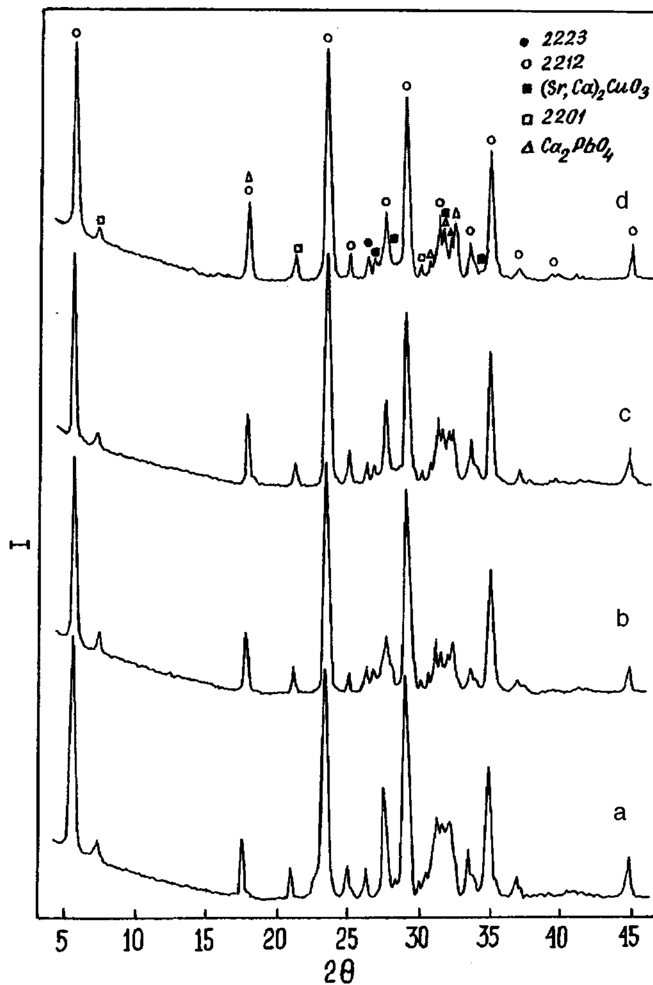

FIG. 1. Diffraction patterns of $Bi_{1.6}Pb_{0.4}Sr_{2-x}K_xCa_2Cu_3F_zO_{y-z}$ samples synthesized at temperatures between 820 and 827 °C for 69.5 h: a) $x=0$, $z=0$; b) $x=0$, $z=0.8$; c) $x=0.02$, $z=0.8$; d) $x=0.05$; $z=0.8$.

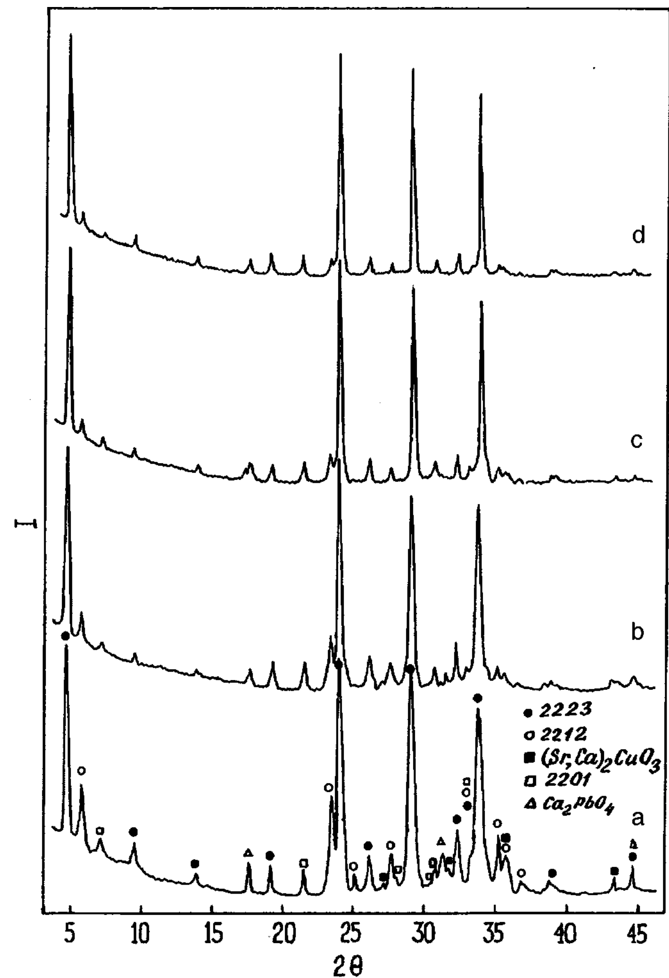

FIG. 2. Diffraction patterns of $Bi_{1.6}Pb_{0.4}Sr_{2-x}K_xCa_2Cu_3F_zO_{y-z}$ samples synthesized at 838 °C for 190 h: a) $x=0$, $z=0$; b) $x=0$, $z=0.8$; c) $x=0.02$, $z=0.8$; d) $x=0.05$; $z=0.8$.

$(Sr,Ca)_2CuO_3$ phase are only present in the initial sample but for samples with added F, or K and F, this phase is not identified on the diffraction patterns. Table I gives the lattice parameters of the 2223 phase determined from the diffraction patterns given in Fig. 2. It can be seen that the addition of F, or of K and F, reduces the lattice parameters. A greater reduction in the lattice parameters is observed for samples with both K and F added. The ratio of the unit cell volumes for samples with added F and with added K and F to the unit cell volume for samples with no additives was 0.9973 and 0.9913, respectively. A similar effect was observed[3,8] when 0.4 mole of CuF_2 was added instead of CuO to $Bi_{1.65}Pb_{0.35}Sr_2{}_-Ca_2Cu_3O_{10}$ samples. The samples with added K and F possessed greater hardness, which was observed during grinding of the pellets and may indicate that these additives have a positive influence on the mechanical properties.

The temperature dependence of the electrical resistivity of samples synthesized at 838 °C is plotted in Fig. 3a. The $R(T)R(200)$ curves for all the samples reveal a superconducting transition near 110 K which is attributable to the 2223 superconducting phase with a zero-resistivity temperature ($T_c(R=0)$) which depends on the composition of the samples (see Table I), and an almost constant transition temperature (Fig. 3). The addition of fluorine and of potassium and fluorine together during slow cooling of the samples reduced $T_c(R=0)$, although the x-ray data (Fig. 2 and Table I) show that these samples have a high content of the 2223 phase. This may be partly caused by a deterioration in the quality of the weak bonds at grain boundaries of the 2223 phase, as is evidenced by the lower critical current of the samples (see Table I). The samples synthesized at 838 °C were then annealed in air at the same temperature for 1 h and quenched by rapid removal from the furnace.

Figure 3b illustrates the influence of quenching on the temperature dependence of the electrical resistivity. For the sample with added fluorine $T_c(R=0)$ increases after quenching, whereas for the initial sample and those with both potassium and fluorine added this temperature decreases (see Table I and Fig. 3b). X-ray examinations do not reveal any substantial influence of quenching on the phase composition of samples synthesized for 190 h, with the 2223 phase dominating as before. The decreases in $T_c(R=0)$ for the initial sample (72% 2223 phase) may be attributed to the loss of oxygen caused by quenching, which is consistent with the published data (see, for example, Ref. 9). The increase in

TABLE I. Structural and superconducting characteristics of $Bi_{1.6}Pb_{0.4}Sr_{2-x}K_xCa_2Cu_3F_zO_{y-z}$ ($x=0$, 0.02, 0.05; $z=0$, 0.8) samples.

Quantity $K(x)$ $F(z)$	Phase 2223(%)	Phase 2212(%)	$T_c(R=0)$,* K	$j_c(77)$, A/cm^2	Lattice parameters** a, Å	c, Å
$x=0$; $z=0$	72	28	109.8(108.7)	27.6	5.411	37.115
$x=0$; $z=0.8$	85	15	109.9(110.8)	4.5	5.406	37.083
$x=0.02$; $z=0.8$	90	10	106.6(101.0)	4.7	5.399	37.019
$x=0.05$; $z=0.8$	93	7	105.6(99.4)	2.6	5.398	36.972

* Values of $T_c(R=0)$ in parentheses refer to quenched samples.
**Lattice parameters given for the 2223 phase.

$T_c(R=0)$ for the fluorine-containing sample agrees with the results of Ref. 4 in which it is assumed that in samples with added F, the carrier concentration should be above optimum to obtain maximum T_c and a reduction in the oxygen content after quenching should reduce the carrier concentration and thus increase $T_c(R=0)$. The existence of an optimum carrier concentration for maximum T_c in a bismuth system was noted in Refs. 9 and 10. According to this reasoning, our results whereby T_c decreases in samples with both K and F added may be interpreted as the result of a decrease in the concentration of carriers relative to the optimum in this case. However, the results for the fluorine-containing samples agree with the results of Ref. 4.

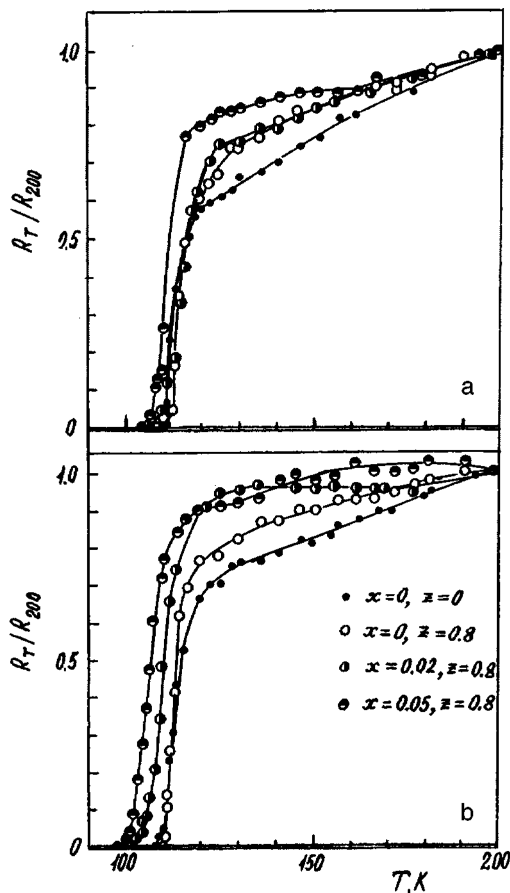

FIG. 3. Temperature dependence of the electrical resistivity of $Bi_{1.6}Pb_{0.4}Sr_{2-x}K_xCa_2Cu_3F_zO_{y-z}$ samples: a) synthesized at 838 °C for 190 h (cooled inside furnace) and b) after quenching from 838 °C.

A comparison of the data plotted in Figs. 1 and 2 indicates that in order to increase the volume fraction of the 2223 phase during synthesis at 838 °C, the maximum possible quantity of the 2212 phase and the intermediate Ca_2PbO_4 and $(Sr,Ca)_2CuO_3$ phases must be formed in the initial calcined materials at the preliminary synthesis stage at temperatures between 820 and 827 °C. Interaction mainly between these phases during synthesis at 838 °C gives a high yield of the 2223 phase (up to 93% for the sample with $x=0.05$ and $z=0.8$).

To sum up, it has been established as a result of these investigations that in a (Bi,Pb)–Sr–Ca–Cu–O system, the simultaneous partial substitution of oxygen with fluorine and strontium with calcium in samples having the nominal composition $Bi_{1.6}Pb_{0.4}Sr_2Ca_2Cu_3O_y$ substantially increases the formation of the 2223 superconducting phase during synthesis at 838 °C. Quenching from the synthesis temperature for fluorine-containing samples increases $T_c(R=0)$, whereas for samples with both F and K added this quenching reduces $T_c(R=0)$. Mixtures of the 2212, Ca_2PbO_4, and $(Sr,Ca)_2CuO_3$ are clearly efficient starting materials for the preparation of bulk samples with a high content of the 2223 high-temperature superconducting phase.

This work was financed by the Basic Research Fund of Belarus.

[1] E. E. Fadeeva, E. N. Ardashnikova, B. A. Popovkin *et al.*, Zh. Neorg. Khim. **38**, 389 (1993).
[2] Xiao-Hui Gao, Shu-Fen Jiang, De Gao *et al.*, Physica C **245**, 66 (1995).
[3] Xiao-Hui Gao, X. L. Wu, H. Yan, and Z. L. Yin, Mod. Phys. Lett. B **4**, 137 (1990).
[4] X.-G. Wang, P.-Y. Hu, Z.-M. Huang *et al.*, Physica C **233**, 327 (1994).
[5] Soo Young Lee, Shigeru Suchara, and Shigeo Horiuchi, Physica C **185–189**, 477 (1991).
[6] V. V. Petrashko, Yu. A. Semenenko, B. V. Novysh, D. M. Turtsevich, and V. P. Yarunichev, Sverkhprovodimost' (KIAE) **5**, 891 (1992).
[7] N. D. Zhigadlo, V. V. Petrashko, Yu. A. Semenenko, N. A. Prytkova, Pis'ma Zh. Tekh. Fiz. **23**(14), 30 (1997) [Tech. Phys. Lett. **23**, 548 (1997)].
[8] Xiao-Hui Gao, Xiao-Gang Wang, Shu-Fen Jiang *et al.*, Phys. Rev. B **50**, 1237 (1994).
[9] B.-F. Yang, H. Deng, X.-Y. Wang *et al.*, Chin. J. Low Temp. Phys. **14**, 283 (1992).
[10] M. Nagoshi, T. Suzuki, Y. Fukuda *et al.*, Phys. Rev. B **43**, 10 445 (1991).

Translated by R. M. Durham
Edited by David L. Book

Influence of a methane atmosphere on the temperature dependence of the conductivity of polycrystalline silicon films

V. N. Shabanov and D. V. Shengurov

N. I. Lobachevskiĭ State University, Nizhniĭ Novgorod
(Submitted November 14, 1997)
Pis'ma Zh. Tekh. Fiz. **24**, 16–19 (May 26, 1998)

The possibility of using polycrystalline silicon films in gas sensors is investigated. An analysis is made of the influence of a small quantity of methane admitted into the surrounding medium on the temperature dependence of the layer resistivity of films doped with acceptor impurities. It is established that the resistivity increases appreciably in the temperature range between 470 and 500°. © *1998 American Institute of Physics.* [S1063-7850(98)02005-9]

Polycrystalline semiconductor films are used as active elements in many solid-state gas sensors. These sensors operate on the principle that their electrical conductivity changes when gas molecules are adsorbed from the surrounding atmosphere. Films of metal oxide semiconductors such as ZnO, SnO_2, TiO_2, and so on, are used for this purpose. One of the mechanisms responsible for influencing the electrical conductivity of the films is a change in the band bending in the crystallites as a function of the species and quantity of adsorbed particles, which is caused by changes in the energy barriers at the grain boundaries and in the concentration of mobile carriers. This mechanism is observed most clearly when the density of biographical surface states is low.[1]

In this context, it is interesting to study the possibility of fabricating gas sensors using polycrystalline silicon films coated with a thin layer of silicon dioxide, where the density of biographical surface states is $<10^9-10^{10}$ cm^2 (Ref. 2).

Polycrystalline silicon films are also of interest for making gas sensors intelligent, since the fabrication technology for these films is compatible with integrated circuit technology.

Here we report results of studies on how a small quantity of methane admitted into the surrounding medium affects the temperature dependence of the layer resistivity of polycrystalline silicon films.

The polycrystalline silicon films were prepared by molecular beam deposition from subliming silicon sources using a technique described in Ref. 3. The sources were single-crystal silicon wafers doped with B, Ga and Al to concentrations of 6×10^{19} cm^{-3}, 6×10^{19} cm^{-3}, and 6×10^{18} cm^{-3}, respectively. The choice of sources with this dopant concentration was based on the need to obtain polycrystalline silicon films possessing fairly high conductivity.[4] The substrates were silicon wafers coated with thermally grown SiO_2 $\sim$0.5 μm thick. The residual gas pressure in the growth chamber during deposition of the films was $\sim10^{-5}$ Pa. The parameters of the films are given in Table I.

TABLE I. Parameters of polycrystalline silicon films.

Sample No.	Source	T_l, °C	Film thickness, μm	Maximum gas sensitivity, $(\Delta R/R)\times100\%$	Temperature at maximum gas sensitivity, °C
89	KDB−0.005	600	0.4	15	480
250	KDG−0.005	700	1.5	40	500
168	KDA−0.005	600	1.2	57	470

The gas sensitivity and the temperature dependence of the resistivity of these polycrystalline silicon films were measured in a vacuum system consisting of a working chamber and a VN-2MG roughing pump. The limiting vacuum was 1.5 Pa. Methane was admitted to the chamber from a cylinder via a flow regulator. In the presence of gas, the pressure in the working chamber was increased to 25–30 Pa, which corresponds to a concentration of methane molecules of $\sim3\times10^{15}$ cm^{-3}. The chamber contained a system of contact probes, a Chromel–Alumel thermocouple, and a heater. The resistivity of the sample was measured with a V7-41 multimeter.

The sample was placed in the vacuum chamber and evacuated. When the pressure reached $\sim$2 Pa, the heater was switched on and the sample was heated to 550–580°C. After the temperature, resistivity (R) of the sample, and pressure had stabilized, the working volume was valved off from the pump, a batch of methane was admitted, and the resistivity of the sample was measured. Figure 1 shows a plot of the

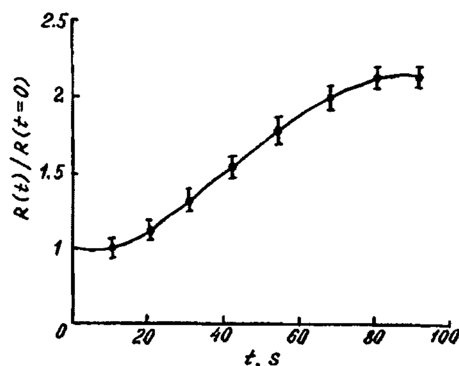

FIG. 1. Time dependence of the change in the resistivity of polycrystalline silicon films in a methane atmosphere.

 © 1998 American Institute of Physics

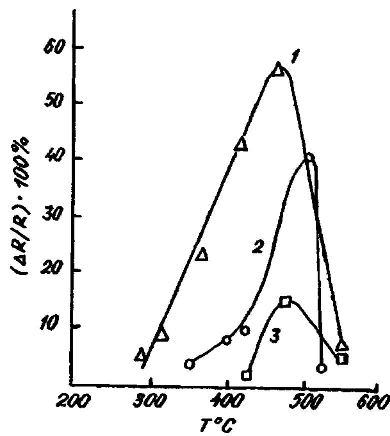

FIG. 2. Temperature dependences of the relative change in the resistivity of polycrystalline silicon films in a methane atmosphere: *1* — Al-doped film, *2* — Ga-doped film, and *3* — B-doped film.

change in resistivity as a function of time after the admission of gas. After the resistivity stabilized, the change in the resistivity ΔR was determined, the valve opened, and the chamber evacuated to its former pressure. In this case, the value of R generally recovered. The temperature was then reduced by 50–70°C and the entire measurement cycle was repeated. At the temperatures where the sensitivity was highest, the measurement cycles were repeated two or three times. The results showed good reproducibility.

The results of measurements of the gas sensitivity of the polycrystalline silicon films are plotted in Fig. 2, which gives the relative change in the resistivity $\Delta R/R$ as a function of temperature. The maximum value of $\Delta R/R$ when methane was admitted was 57% for sample No. 168 doped with Al.

We attribute the increased resistivity of the films during the admission of gas to an increase in the height of the potential barriers at the grain boundaries caused by the adsorption of methane. The bell-shaped temperature dependence of the gas sensitivity is typical of many semiconducting gas-sensitive elements. As yet, no definitive explanation can be put forward for this observation.

The results indicate that the resistivity of acceptor-doped polycrystalline silicon films increases appreciably in a methane atmosphere at sample temperatures of ~470–500°C. The dependence $\Delta R/R(T)$ is bell-shaped.

[1] I. A. Myasnikov, V. Ya. Sukharev, P. Yu. Kupriyanov, and S. A. Zav'yalov, *Semiconductor Sensors in Physicochemical Research* [in Russian], Nauka, Moscow (1991), p. 39.
[2] *VLSI Technology*, edited by S. M. Sze (McGraw-Hill, New York, 1983; Mir, Moscow, 1986).
[3] D. A. Pavlov, V. G. Shengurov, D. V. Shengurov, and A. F. Khokhlov, Fiz. Tekh. Poluprovodn. **29**, 286 (1995) [Semiconductors **29**, 142 (1995)].
[4] *Polycrystalline and Amorphous Thin Films and Devices*, edited by L. L. Kazmerski (Academic Press, New York 1980; Mir, Moscow, 1983).

Translated by R. M. Durham
Edited by David L. Book

A new method of producing thin films

M. A. Khodorkovskiĭ, A. L. Shakhmin, S. V. Murashov, A. M. Alekseev, Yu. A. Golod, and A. N. Fedorov

''Applied Chemistry'' Russian Scientific Center; St. Petersburg Joint Research Center

(Submitted October 10, 1997)
Pis'ma Zh. Tekh. Fiz. **24**, 20–23 (May 26, 1998)

A new method is proposed for the deposition of thin films using a pulsed supersonic molecular beam seeded with molecules of the material being deposited, and a comparison is made between this method and the conventional one. Taking as an example the unique properties of thin fullerene films obtained experimentally by this method, it is concluded that this method is potentially useful for depositing films of various materials. © *1998 American Institute of Physics.* [S1063-7850(98)02105-3]

Descriptions of adsorption processes available in the literature make very little allowance for the kinetic and vibrational–rotational energies of the impinging molecule. This factor is attributable to the methods of forming the vapor phase conventionally used in the deposition of thin films and epitaxial layers, where the energy of the adsorbed atoms and molecules is determined by the evaporation temperature of the initial materials and does not exceed 0.2–0.3 eV. However, the binding energy between adsorbed molecules and a surface and between the molecules themselves is in many respects determined by their energy parameters.[1] Methods of producing thin films are now beginning to be developed in which the kinetic energy of the adsorbed molecules may reach several tens of electron volts.[2] One of the most promising of these is the seeded supersonic molecular beam method.[3] In addition to having a high kinetic energy, the velocity distribution of the molecules in these beams will correspond to very low temperatures (down to $T=20$ K (Ref. 4)) as a result of gasdynamic cooling. This narrow velocity distribution in supersonic molecular beams of adsorbed particles is responsible for producing homogeneous bonds between the adsorbate and the surface and between the particles themselves. Unlike diffusion beams, the values of these parameters can easily be varied over a wide range by varying the conditions in the nozzle chamber (species and pressure of the carrier gas, temperature and nozzle geometry, and so on).

Here we report the development of a new method of seeding supersonic molecular beams by passing a stream of carrier gas from a supersonic nozzle through a gas cell containing molecules of the material being deposited. Separating the zones where the supersonic carrier-gas molecular beam is formed and seeded allows us to vary the parameters of the gas cell and the nozzle source independently. This means that our method can be used to deposit thin films of almost any materials. In addition, by varying the kinetic energy of the deposited molecules over a wide range (0.3–10.0 eV), it is possible to obtain not only films with new properties but also those with prescribed properties.

As far as we are aware, no applications of this method to deposit thin films have been described in the literature.

We used our method to deposit thin films of fullerenes (86% C_{60} + 14% C_{70}) and their properties were compared with those of thermally deposited films.

A conventional pulsed supersonic molecular beam system (see Fig. 1) was fitted with time-of-flight mass-spectrometric diagnostics which could be used to monitor the beam composition during the film deposition experiments. The carrier gas was helium at a pressure of up to 5 atm in the nozzle chamber. A Knudsen cell at a temperature of 400–600 °C was used to admit fullerene vapor into the flux of molecular helium. The working chamber was evacuated to a residual pressure of 10^{-8} Torr. Depending on the conditions in the nozzle chamber and the temperature in the Knudsen cell, the kinetic energy of the fullerene molecules was in the range 0.1–2.0 eV. The concentration of fullerene vapor in the flux could produce 200 nm thick films in 1 h.

The investigations revealed that the properties of these films differ substantially from those deposited by other methods, and specifically:

– the molecular structure of the fullerenes showed no

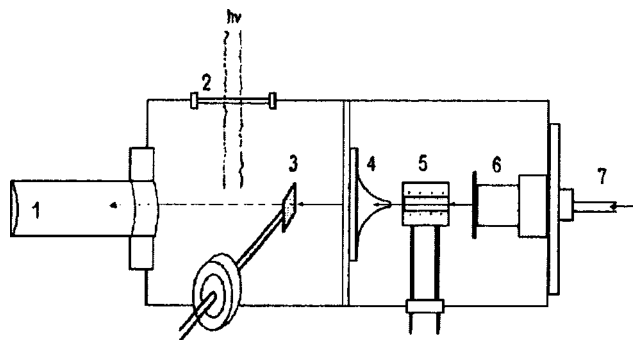

FIG. 1. Schematic of apparatus to form a supersonic molecular beam of carrier gas seeded with molecules of the material being deposited, with time-of-flight mass spectrometric diagnostics: *1* — entrance of drift tube of time-of-flight mass spectrometer, *2* — window for coupling in laser radiation, *3* — sample attached to rotating rod on sample manipulator, *4* — skimmer, *5* — vapor source of material to be deposited, *6* — supersonic pulsed nozzle, and *7* — carrier gas intake.

 © 1998 American Institute of Physics

degradation under laser irradiation until they evaporated, whereas conventional films started to deteriorate at laser power densities two orders of magnitude lower;

– the desorption temperatures were 500 °C, whereas those for thermally deposited films were 300 °C.

These properties are attributable to the formation of stronger bonds between the adsorbed molecules and the surface and between the molecules themselves. Thus, the capabilities of the method described above combined with the experimental results confirm the potential usefulness of this method for depositing thin films with new properties.

To conclude, the authors would like to thank S. G. Konnikov, V. Yu. Davydov, and A. A. Sitnikova (A. F. Ioffe Physicotechnical Institute) and E. E. B. Campbell (Max Born Institute) for assistance in studying the properties of the films, and also R. Naaman (Weizman Institute of Science) for useful discussions, and A. Ya. Vul' (A. F. Ioffe Physicotechnical Institute) for showing continuous interest in this work.

This work was financed by the ''Fund for Intellectual Collaboration'' under the program ''Fullerenes and Atomic Clusters,'' supported by the Russian Ministry of Science.

[1] Ch. Girard, Ph. Lambin, A. Dreux, and A. A. Lucas, Phys. Rev. B **49**, 11 425 (1994).

[2] E. Budrevich, B. Tsipinyuk, and E. Kolodney, J. Phys. Chem. **100**, 1475 (1996).

[3] J. D. Anderson, R. P. Andres, and J. B. Fenn, *Studies Using Molecular Beams*, in *Molecular Beams Produced Using Supersonic Nozzles*, Mir, Moscow (1969), pp. 299–345.

[4] M. A. Khodorkovskiĭ, A. A. Markov, A. I. Dolgin, Zh. Tekh. Fiz. **59**(8), 89 (1989) [Sov. Phys. Tech. Phys. **34**, 898 (1989)].

Translated by R. M. Durham
Edited by David L. Book

Investigation of the structure of thin layers of hexadecane on a metal substrate by infrared spectroscopy

V. I. Vettegren' and A. I. Tupitsyna

A. F. Ioffe Physicotechnical Institute, Russian Academy of Sciences, St. Petersburg;
Institute of Problems in Mechanical Engineering, Russian Academy of Sciences, St. Petersburg
(Submitted September 15, 1997)
Zh. Tekh. Fiz. **24**, 24–28 (May 26, 1998)

Infrared spectroscopy was used to analyze the structure of 0.5–10 μm thick layers of hexadecane on a metal substrate in the range 3000–2800 cm^{-1}. The results suggest that density fluctuations occur in layers between 3 and 10 μm thick, whereas the hexadecane crystallizes in thinner layers. © *1998 American Institute of Physics.* [S1063-7850(98)02205-8]

Studies of the structure of thin layers of wetting liquid on the surface of solids are of major interest for surface physics and chemistry. Here we report results of a study of the structure of hexadecane ($C_{16}H_{34}$) in layers between ~0.5 and 10 μm thick on an Al surface using infrared spectroscopy (the melting point of hexadecane is 18.2 °C at 1 atm).

Aluminum plates were washed with acetone, a layer of $C_{16}H_{34}$ was applied with a soft brush, and the plates were placed horizontally in an external reflection adaptor, which was mounted in the cell section of a Specord-75 IR infrared spectrophotometer. A light beam was directed onto the substrate at an angle of 20° and passed through the sample layer before and after being reflected by the metal. The spectra were recorded at 25 °C. The thickness of the layer was determined by weighing and from the intensity of the 1378 cm^{-1} reference band. Overlapping bands were separated using the Peakfit program.

Figure 1 shows the infrared spectrum of a 0.5 μm thick layer of hexadecane in the range 2800–3000 cm^{-1}. This ranges includes the 2924 and 2855 cm^{-1}, and 2959 and 2873 cm^{-1} bands assigned to the CH_2 and CH_3 antisymmetric and symmetric vibrations, respectively, and also the ~2900 cm^{-1} band assigned to Fermi-resonant interaction between the CH_2 symmetric mode and the CH_2 overtone of the scissoring mode.[1]

According to data given in Ref. 2, the widths of the 2924 and 2855 cm^{-1} bands at 0.75 maximum are 17 cm^{-1} and 9 cm^{-1} for liquid hexadecane, whereas those measured by us for a 0.5 μm thick layer on an Al surface are 13 and 7 cm^{-1}, respectively. It was shown in Refs. 2–4 that the widths of these bands are predominantly influenced by three factors: the degree of conformational order, the rotational motion of the molecules, and the interaction between the vibrational modes under study and low-frequency libration–torsional vibrations of methylene groups. The authors of Ref. 2 investigated the widths of the infrared bands of CH stretching vibrations of hexadecane molecules enclosed in narrow channels formed by urea molecules. Under these conditions, the methylene groups are completely conformationally ordered, but at room temperature they can rotate about their axis and retain libration–torsional degrees of freedom (rotation of CH_2 groups). The band widths of the stretching vibrations of CH_2 groups at 0.85 maximum measured by us for a thin layer of hexadecane were slightly smaller than the values given in Ref. 2, at 25 °C (≈1 and 0.5 cm^{-1} smaller for the 2924 and 2855 cm^{-1} bands, respectively). However, when the rotational degrees of freedom are completely frozen, the widths of these bands at this height are reduced by 4 and 3 cm^{-1} for the antisymmetric and symmetric modes, respectively.[2] These data suggest that in a 0.5 μm thick layer on an Al substrate $C_{16}H_{34}$ molecules are conformationally ordered (i.e., contain no Gauche conformers) and possess rotational degrees of freedom.

Conformational ordering of the chains and the presence of rotational degrees of freedom are typical of the high-temperature crystalline phase of alkanes and thus we postulate that in a thin layer on a metal surface, hexadecane forms a high-temperature crystal with hexagonal symmetry.

When the thickness of the $C_{16}H_{34}$ layer is increased above 3 μm, the 2924 cm^{-1} band splits into two. This splitting increases with increasing thickness and reaches 20 cm^{-1} (2935 and 2915 cm^{-1}) in the spectra of 10 μm thick samples (Fig. 2). The spectra of the 10 μm thick samples also reveal splitting of the 2855 cm^{-1} bands by 4 cm^{-1} and of the 2900 cm^{-1} band by 6 cm^{-1}.

It has been established that[5] the frequency shifts of the

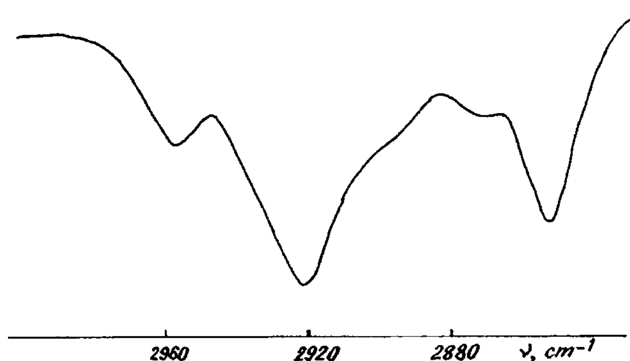

FIG. 1. Infrared spectrum of a thin layer (0.5 μm) of hexadecane on an aluminum substrate in the range 2800–3000 cm^{-1}.

 © 1998 American Institute of Physics

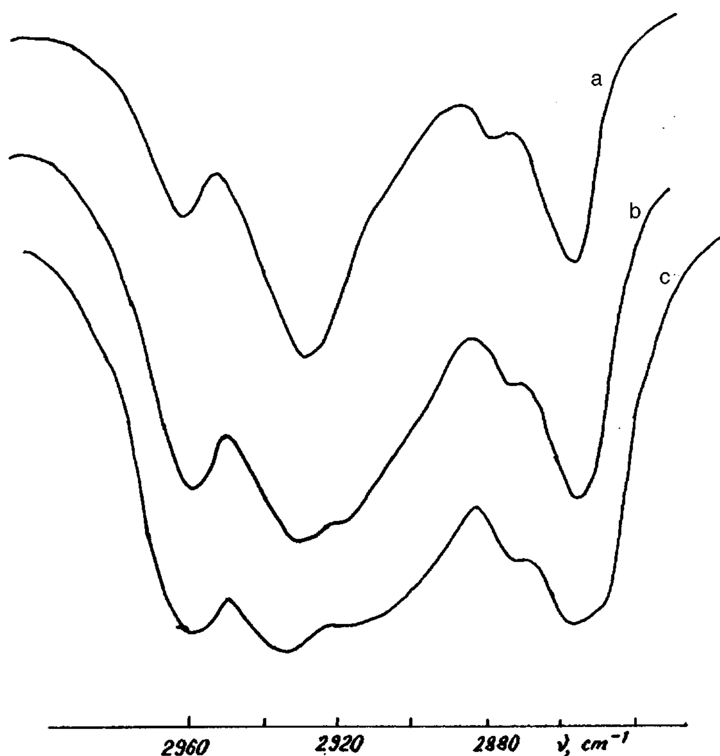

FIG. 2. Infrared spectra of layers of hexadecane of varying thickness on an aluminum substrate in the range 2800–3000 cm^{-1}. Layer thickness: a — 2 μm, b — 5 μm, and c — 10 μm.

CH_2 stretching vibrations are mainly caused by changes in the valence bonds and angles in the CH_2 group. Deformation of molecular bonds and angles is caused by severe compression or stretching of the samples:[6] compression causes a high-frequency shift and stretching causes a low-frequency shift, with these frequency shifts being considerably stronger for the antisymmetric vibrations compared with the symmetric ones.[5,6] For these reasons, the splitting of these bands can be attributed to the existence of density fluctuations.

The amplitude of the density fluctuations in a 10 μm layer calculated from the band shifts was $\approx$5–7% (the Grüneisen parameter for the antisymmetric mode of the CH_2 group was taken as 0.07 (Ref. 8)). It is known that the probability of the formation of high-intensity fluctuations increases abruptly near phase transition points.[7] Thus, the existence of intense fluctuations may be taken as a precursor of hexadecane crystallization.

The half-width of the 2935 cm^{-1} band was the same as that for the 2924 cm^{-1} band in a 0.5 μm thick layer, 24 cm^{-1}, while the half-width of the 2915 cm^{-1} band was 40 cm^{-1}. These data can be explained by the fact that in regions of high density, the hexadecane molecules exhibit conformational ordering, whereas in regions of low density they are disordered.

The effects observed suggest that when the thickness of a layer of hexadecane on an aluminum surface decreases, a phase transition takes place and a high-temperature crystal forms.

The authors would like to thank I. Markovich (Jerusalem University) for supplying the hexadecane.

[1] R. G. Snyder, J. Chem. Phys. **71**, 3229 (1979).
[2] V. R. Kodati, R. El-Jastimi, and M. Lafleur, J. Chem. Phys. **98**, 12191 (1994).
[3] K. A. Wood, R. G. Snyder, and H. L. Strauss, J. Chem. Phys. **91**, 5255 (1989).
[4] K. J. Lee, W. L. Mattice, and R. G. Snyder, J. Chem. Phys. **96**, 9138 (1992).
[5] M. V. Vol'kenshteĭn, L. A. Gribov, M. A. El'yashevich, and B. I. Stepanov, *Molecular Vibrations* [in Russian], Nauka, Moscow (1972).
[6] P. T. T. Wong, T. E. Chagwedera, and H. H. Mantsch, J. Chem. Phys. **87**, 4487 (1987).
[7] H. E. Stanley, *Introduction to Phase Transitions and Critical Phenomena* (Clarendon Press, Oxford, 1971).
[8] C. K. Wu, G. Jura, and M. Shen, J. Appl. Phys. **43**, 4348 (1972).

Translated by R. M. Durham
Edited by David L. Book

Theory of internal thermal equilibrium in inhomogeneous structures

S. O. Gladkov

Institute of Chemical Physics, Russian Academy of Sciences, Moscow
(Submitted September 5, 1997; resubmitted December 29, 1997)
Pis'ma Zh. Tekh. Fiz. **24**, 29–36 (May 26, 1998)

Characteristic features of the establishment of thermal balance between the phases are identified for an arbitrary P-component composite and the time constant for temperature equalization is calculated. An analysis is made to ascertain how the size distribution of the impurity phase influences the time behavior of the composite temperature. A Laplace transformation is used to find a general expression for $\delta T_0(t)$ and the specific form of this functional dependence is calculated when the particles of the finely dispersed phase have a Poisson distribution.
© *1998 American Institute of Physics.* [S1063-7850(98)02305-2]

In most cases, problems associated with studies of heat conduction in various types of crystalline, amorphous, and liquid structures, and other considerably more complex structures, particularly composites and composite materials, have been resolved, and a vast number of original articles and books have been published on these topics. The most comprehensive information which reflects the essence of the problems in these materials can be found in books[1,2] (see also Refs. 3–7) which are rightly regarded as classics and reflect and accurately describe not only an abundance of experimental data but also problems which are purely exercises in applied calculations. For example, the authors of Ref. 1 give numerous examples of solutions of fundamental practical problems which are important for pure engineering applications.

However, it must be said that despite the extensive range of conceivable and speculative examples contained in the literature, there is, in our view, an equally important problem from not only the procedural point of view, but also from the practical point of view, which requires an adequate description and accurate solution. Here we refer to a composite whose basic matrix contains finely dispersed formations (subsequently called the impurity phase or simply impurities) whose physical parameters differ from those of the main phase.

Suppose that such a structure is heated. Since the specific heats and thermal diffusivities of the two phases are different, the heating of the composite will be extremely nonuniform and inhomogeneous. In this context, we can assume that at any time the average temperature in the main matrix will be T_0 and that in the impurity phase will be T_β, where the Greek subscript β, having values of $1,2,3,\ldots,P$, characterizes the number of physically different phases whose number is P. Heating then ceases and the composite is placed instantaneously in a thermally insulated medium (i.e., within a time $\delta t \ll t_{\text{h.c.}}$, where $t_{\text{h.c.}}$ is the time constant for establishment of the temperature over the entire sample as a result of heat conduction). The question then arises as to how the temperature should be redistributed in the structure if we assume, for the sake of argument, that $T_\beta > T_0$? The present paper is devoted to answering this question.

Let us take the specific heat per unit mass of the main matrix as c_{0m} and that of the impurity phase as $c_{\beta m}$. Obviously, as a result of the contact influence of the finely dispersed impurities on the main matrix and because of their large number (but small size!), the temperature T_0 increases and T_β decreases. The equilibrium temperature of all the subsystems for $t \Rightarrow \infty$ will then by given by

$$T_{\text{eq}} = \frac{m_0 c_{0m} T_0 + \Sigma^P m_\beta c_{\beta m} T_\beta}{m_0 c_{0m} + \Sigma m_\beta c_{\beta m}}, \tag{1}$$

where m_0 and m_β are the masses of the two phases, respectively.

The heat conduction equations which describe the approach of the two subsystems to the common temperature T_{eq} are then written as the following system:

$$\begin{cases} C_0 \delta \dot{T}_0 = \varkappa_0 \Delta \delta T_0 - \sum_{\beta=1}^{P} \sum_{i=1}^{N_P} \alpha_{0\beta}^{*(i)} (\delta T_0 + \delta T_\beta^{(i)}), \\ C_\beta \delta \dot{T}_\beta^{(i)} = \varkappa_\beta^{(i)} \Delta \delta T_\beta^{(i)} - \alpha_{\beta 0}^{*(i)} (\delta T_0 + \delta T_\beta^{(i)}), \end{cases}$$

where N_P is the total number of particles of the Pth impurity phase and the new index $i = 1,2,3,\ldots,N_P$ labels these particles, $\delta T_0 = T_{\text{eq}} - T_0$, $\delta T_\beta^{(i)} = T_\beta^{(i)} - T_{\text{eq}}$, $C_0 = \rho_0 c_{0m}$, $C_\beta = \rho_\beta c_{\beta m}$, ρ_0 is the density of the main matrix, and ρ_β is the density of the finely dispersed phase.

The coefficients α^* which appear in Eqs. (2) and (3) are related to the usual heat transfer coefficients by $\alpha_{0\beta}^{*(i)} = \alpha_{0\beta}^{(i)}/\delta_1$ and $\alpha_{\beta 0}^{*(i)} = \alpha_{\beta 0}^{(i)}/\delta_2$, where $\alpha_{0\beta}^{(i)}$ is the coefficient of heat transfer from the main matrix to the ith particle of the β impurity phase, $\alpha_{\beta 0}^{(i)}$ is the coefficient of heat transfer from the ith particle of the β impurity phase to the main matrix, and the linear dimension δ is of the same order of magnitude as the path length l of that quasiparticle which is typical of a given material. If the main matrix and the impurity phase are dielectrics and the temperature of the medium is lower than the Debye temperature, acoustic phonons play the role of these quasiparticles.[8] If the temperatures are high, optical phonons may well play this role. That is to say, for a dielectric we have $\delta_1 \cong l_{1ph} = c_{1s}\tau_1$, where c_{1s} is the velocity of sound in the impurity phase and τ_1 is the relaxation time,

 © 1998 American Institute of Physics

which is associated with interaction between impurity-phase phonons and phonons of the main matrix in the boundary region, and $\delta_2 \cong l_{2ph} = c_{2s}\tau_2$, where c_{2s} is the velocity of sound in the main matrix and τ_2 is the relaxation time associated with interaction between phonons in the main matrix and boundary phonons in the impurity phase. Quite clearly, the relaxation times τ_1 and τ_2 differ because of the difference between the phase volumes for the two types of phonons. It should also be noted that if the particles of the finely dispersed phase are too fine, the role of the path length l_1 and l_2 may be converted simply to the average linear dimension R of these particles.

Equation (2) is averaged over some arbitrary volume δV considerably greater than the volume of the particles of the finely dispersed phase, i.e., $v_\beta^{(i)} \ll \delta V \ll V$, where $v_{\beta(i)}$ is the volume of the ith particle of the β phase and V is the volume of the composite. Clearly, if we imagine the volume of the entire composite to be divided into q volumes δV ($q = V/\delta V$), on average equal, each of the elements δV may contain between one and several impurity particles. We shall therefore assume that the change in the average temperature $T_0 = \langle T_0 \rangle = \int T_0 dv/\delta V$ caused by the presence of several impurities in the volume δV is equal to the natural temperature fluctuations of the main matrix. This implies that

$$\int_{\delta V} \varkappa_0 \Delta\, \delta T_0 dv/\delta V = (\varkappa_0/\delta V) \int_{\delta S} \nabla\, \delta T_0 dS.$$

However, the last integral will be of the same order of magnitude as $\varkappa_0 \delta T_0 / L^2$ because of the continuity of the heat flux from the volume δV, provided that on the surface δS surrounding the volume δV there are no external heat sources. This condition can always be satisfied by suitably selecting the volume δV so as to eliminate any impurity particles from its surface. The parameter L characterizes the linear dimension of the region δV. As a result of this averaging, the system of equations (2)–(3) has the form

$$\begin{cases} C_0 \delta\dot{T}_0 = -\alpha_0^* \delta T_0 - \sum_{\beta=1}^{P} \sum_{i=1}^{N_P} \alpha_{0\beta}^{*(i)} \delta T_\beta^{(i)}, \\ C_\beta^{(i)} \delta\dot{T}_\beta^{(i)} = -\alpha_{\beta 0}^{*(i)} (\delta T_0 + \delta T_\beta^{(i)}). \end{cases}$$

The quantity α_0^* in Eq. (4) allows not only for the dimensions of the region of integration L but also for its limits between the main matrix and the impurity phase, and is given by

$$\alpha_0^* = \varkappa_0/L^2 + \sum_{\beta=1}^{P} \sum_{i=1}^{N_P} \alpha_{0\beta}^{*(i)}.$$

Since the times being considered are $\delta t \ll R_\beta^2/\min\{\chi_\beta^{(i)}\}$, where $\chi_\beta^{(i)}$ is the thermal diffusivity of the impurities and R_β is their linear dimension, the inhomogeneous term $\varkappa_\beta^{(i)} \Delta\, \delta T_\beta^{(i)}$ in Eq. (5) can be dropped.

The solution of Eq. (5) obviously has the form

$$\delta T_\beta^{(i)} = B e^{-\gamma_\beta^{(i)} t} - \gamma_\beta^{(i)} e^{-\gamma_\beta^{(i)} t} \int_0^t \delta T_0(\tau) e^{\gamma_\beta^{(i)} \tau} d\tau, \tag{5}$$

where

$$\gamma_\beta^{(i)} = \alpha_{\beta 0}^{*(i)} / C_\beta^{(i)}. \tag{6a}$$

The integration constant B will be discussed at the end of the calculations.

If the discrete index i is replaced by the size distribution function of β-phase particles $f_\beta(R)$, Eq. (4) with allowance for the solution (6) is written as follows:

$$\begin{aligned} C_0 \delta\dot{T}_0 = &-\alpha_0^* \delta T_0 - B \sum_{\beta=1}^{P} N_\beta \int_0^\infty f_\beta(R) \alpha_{0R}^* e^{-\gamma_{\beta R} t} dR \\ &+ \sum_{\beta=1}^{P} N_\beta \int_0^\infty f_\beta(R) \alpha_{0R}^* \gamma_{\beta R} \\ &\times \int \delta T_0(\tau) e^{-\gamma_{\beta R}(t-\tau)} d\tau dR. \end{aligned} \tag{7}$$

We solve this equation by means of a Laplace transformation. In fact, since the transform is

$$\delta T_p = \int_0^\infty \delta T_0(t) e^{-pt} dt, \tag{8a}$$

and the inverse transform is

$$\delta T_0(t) = \int_{\sigma - i\infty}^{\sigma + i\infty} \delta T_p e^{pt} dp/2\pi i, \tag{8b}$$

we have, from Eq. (7)

$$\begin{aligned} C_0(\delta T(0) + p\,\delta T_p) = &-\alpha_0^* \delta T_p - B \sum_{\beta=1}^{P} N_\beta \\ &\times \int_0^\infty f_\beta(R) \alpha_{\beta 0R}^* dR/(p + \gamma_{\beta R}) \\ &+ \sum_{\beta=1}^{P} N_\beta \int_0^\infty f_\beta(R) \alpha_{\beta 0R}^* \gamma_{\beta R} dR \\ &\times \int_0^\infty dt \int_0^t \delta T_0(\tau) e^{-\gamma_{\beta R}(t-\tau) - pt} d\tau. \end{aligned} \tag{9}$$

Changing the order of integration by means of a Dirichlet transformation[9] reduces the last integral to the form

$$\begin{aligned} J = &\sum_{\beta=1}^{P} N_\beta \int_0^\infty f_\beta(R) \alpha_{\beta 0R}^* \gamma_{\beta R} dR \int_0^\infty dt \int_0^t \delta T_0(\tau) \\ &\times \exp\{-\gamma_{\beta R}(t-\tau) - pt\} d\tau \\ = &\ \delta T_p \sum N_\beta \int f_\beta(R) \alpha_{\beta 0R}^* \gamma_{\beta R} dR/(p + \gamma_{\beta R}), \end{aligned} \tag{10}$$

and we finally have

$$\delta T_p = -\frac{C_0\delta T(0)+B\sum_{\beta=1}^{P} N_\beta \int_0^\infty f_\beta(R)\alpha^*_{\beta 0R} dR/(p+\gamma_{\beta R})}{\alpha_0^* + C_0 p - \sum_{\beta=1}^{P} N_\beta \int_0^\infty f_\beta(R)\alpha^*_{\beta 0R}\gamma_{\beta R} dR/(p+\gamma_{\beta R})}. \tag{11}$$

We now calculate δT_p for a specific dependence $f_\beta(R)$. Let us assume that the distribution function is defined as a Poisson distribution, i.e.,

$$f_\beta(R) = (R/R_{0\beta})^{k_\beta} \exp\{-R/R_{0\beta}\}/k_\beta! R_{0\beta}, \tag{12}$$

where k_β are integers.

Since the coefficients of heat transfer $\alpha_{0\beta}$ ($\alpha_{\beta 0}$) are inversely proportional to the area of the contact surface, $\alpha_{0\beta}$ ($\alpha_{\beta 0}$) is proportional to R_0^{-2}. Using Eqs. (12) and (6a), the integrals appearing in Eq. (11) can easily be calculated using the Cauchy theorem and residue theory. Assuming $B=\delta T_0(0)$, we then have

$$\delta T_p = -\frac{C_0 + \Sigma_{\beta=1}^{P} N_\beta J_{1\beta}(p)}{\alpha_0 + C_0 p - \Sigma_{\beta=1}^{P} N_\beta J_{2\beta}(p)} \delta T_0(0), \tag{13}$$

where

$$J_{1\beta} = (\pi C_\beta/4k_\beta!)(C_\beta p/\alpha^*_\beta)^{k_\beta/2+1} \times \exp\{-(C_\beta p/\alpha^*_\beta)^{1/2}\},$$

$$J_{2\beta} = (\pi C_\beta p/4k_\beta!)(C_\beta p/\alpha^*_\beta)^{k_\beta+0.5} \times \exp\{-(C_\beta p/\alpha^*_\beta)^{1/2}\},$$

where C_β is the specific heat of the β finely dispersed phase, $\alpha^*_\beta = \alpha_\beta/\delta_1$, and α_β is the coefficient of heat transfer of an individual β-phase particle.

Using a Mellin transformation, we can write the change in the temperature of the main matrix as

$$T_0(t) = T_{\rm eq} - \delta T_0(0)\,{\rm Re} \times \int_{\sigma - i\infty}^{\sigma + i\infty} \frac{[e^{pt}(C_0 + \Sigma N_\beta J_{1\beta}(p))]dp}{[\alpha_0 + C_0 p - \Sigma N_\beta J_{2\beta}(p)]}. \tag{14}$$

This integral is easily estimated in two limiting cases: (a) $|p| \gg \alpha^*_\beta/C_\beta$ and (b) $|p| \ll \alpha^*_\beta/c_\beta$. In case (a), $\Sigma N_\beta J_{1,2\beta}(p)$ is exponentially small and the integral (14) for $\sigma < \alpha_0^*/C_0$ gives

$$T_0(t) = T_{\rm eq} - \delta T_0(0) e^{-\alpha_0^* t/C_0}, \tag{15}$$

i.e., the cooling time is

$$t_{1\rm cool} \cong C_0/\alpha_0^*. \tag{16}$$

In case (b), $\Sigma N_\beta J_{1,2\beta}(p)$ is proportional to p^ν. The denominator of the integral (14) is

$$Z = \text{denominator} = C_0 \left[\alpha_0^*/C_0 + p - (\pi p/4) \sum_{\beta=1}^{P} ((C_\beta p/\alpha^*_\beta)^{k_\beta+1.5})/k_\beta! \right].$$

Assuming that $k_\beta = 0$, we then have

$$Z/C_0 = (\alpha_0^*/C_0 + p - \pi p^{5/2} D/4),$$

where $D = \Sigma_{\beta=1}^{P} (C_\beta/\alpha^*_\beta)^{3/2}$. That is to say, for large $|p| \gg \alpha_0^*/C_0$ we have

$$p_0 \cong (4\alpha_0^*/\pi C_0 D)^{2/5} \gg \alpha_0^*/C_0. \tag{17}$$

Thus, in this case the cooling time is

$$t_{2\rm cool} \cong (\pi C_0 D/4\alpha_0^*)^{2/5}. \tag{18}$$

When α_0^* is of the order of α^*_β, C_0 is of the order of C_β and $t_{2\rm cool} \cong [\pi P (C_0/\alpha_0^*)(C_0/\alpha_0^*)^{3/2}]^{2/5}$, or

$$t_{2\rm cool} \cong (C_0/\alpha_0^*) P^{2/5} > t_{1\rm cool}. \tag{19}$$

To sum up, we mention the results which in our view are the most important.

1. A theory has been constructed for the establishment of thermal equilibrium in complex composite structures when the main matrix contains P impurity phases with specific physical characteristics (heat transfer coefficient α, specific heat C_β, and thermal conductivity $\varkappa_\beta$).

2. It has been shown that the size distribution of the impurity phase has a very strong influence on the time taken for the establishment of thermal equilibrium. This spread is taken into account by introducing the distribution function $f_\beta(R)$.

3. It has been demonstrated that the time taken for the establishment of equilibrium between the two subsystems (impurity + main matrix) depends very strongly on the number of impurity phases (see formula (19)) and on the relation between the properties of the main matrix and the impurity.

[1] H. S. Carslaw and J. C. Jaeger, *Conduction of Heat in Solids*, 2nd ed. (Clarendon Press, Oxford, 1959; Nauka, Moscow, 1964).
[2] G. N. Dul'nev and Yu. P. Zarichnyak, *Thermal Conductivity of Mixtures and Composites* [in Russian], Énergiya, Leningrad (1974).
[3] M. S. Bresler, R. V. Parfenov, and S. S. Shalyt, Fiz. Tverd. Tela (Leningrad) **8**, 1776 (1966) [Sov. Phys. Solid State **8**, 1414 (1966)].
[4] S. O. Gladkov, Physica B **167**, 159 (1990).
[5] E. Burzo and R. Teteanu, Solid State Commun. **86**, 493 (1993).
[6] S. O. Gladkov, Fiz. Tverd. Tela (St. Petersburg) **39**, 1622 (1997) [Phys. Solid State **39**, 1446 (1997)].
[7] S. O. Gladkov, Zh. Tekh. Fiz. **67**(7), 8 (1997) [Tech. Phys. **42**, 724 (1997)].
[8] V. L. Gurevich, *Transport in Phonon Systems* (North–Holland, Amsterdam, 1986; Nauka, Moscow, 1980).
[9] V. I. Smirnov, *A Course of Higher Mathematics*, Vol. 2 (Addison–Wesley, Reading, Mass., 1964; Russ. original, later ed., Nauka, Moscow, 1967).

Translated by R. M. Durham
Edited by David L. Book

Mechanisms of photocurrent amplification in isotypic n^+–GaSb–n^0–GaInAsSb–n^+–GaAlAsSb heterostructures

S. V. Slobodchikov, Kh. M. Salikhov, Yu. P. Yakovlev, and B. E. Samorukov

A. F. Ioffe Physicotechnical Institute, Russian Academy of Sciences, St. Petersburg
(Submitted October 2, 1997)
Pis'ma Zh. Tekh. Fiz. **24**, 37–42 (May 26, 1998)

Measurements of the current–voltage characteristics, the photocurrent, and its dependence of the latter on the bias voltage (forward and reverse) and the magnetic field were used to determine the current transport mechanisms in isotypic n^+–GaSb–n^0–GaInAsSb–n^+–GaAlAsSb heterostructures. Two mechanisms of photocurrent amplification were observed. In structures with binary injection in the diffusion approximation amplification is caused by a change in the lifetime with the level of dark carrier injection. In structures with drift transport, amplification is caused by a ''transit'' effect. In both cases, the trapping levels play an important role. © *1998 American Institute of Physics.* [S1063-7850(98)02405-7]

Gallium antimonide heterostructures with narrow-gap ternary and quaternary solid solutions are finding important practical applications. These p–n heterostructures have been used to fabricate light-emitting diodes,[1] lasers,[2] and photodiodes[3] in the middle infrared. Less attention has been paid to studies of the electrical and photoelectrical properties of isotypic heterostructures. The authors of Ref. 4 reported some results of studies of the photoelectric characteristics of these isotypic heterostructures, where the observed photocurrent amplification was attributed to increased transparency of the barrier at the heterojunction.

Here we report new data which reveal a link between the current transport mechanism and the photocurrent amplification mechanism in n^+–GaSb–n^0–GaInAsSb–n^+–GaAlAsSb heterostructures (Fig. 1a). The fabrication technology for the heterostructures was basically the same as that used in Ref. 4. We used a standard photolithographic technique and vacuum deposition to fabricate mesaphotostructures with a mesa diameter of 300 μm and a 50 μm diameter Ohmic point contact to the illuminated n^+–GaAlAsSb surface and a fused contact to n^+–GaSb. For the investigations the structures were mounted in a standard TO-18 casing.

The current–voltage characteristics, photo-emf, and photocurrent were investigated as functions of the forward (at n^+–GaSb) and reverse bias, and the photocurrent was also studied as a function of the magnetic field. Figure 1b shows current–voltage characteristics measured at $T=300$ and 78 K. Two types of characteristic were typically observed at $T=300$ K: a) an exponential dependence of current on voltage at low bias $I\sim\exp(qV/nkT)$ with $n=1.7$–2 (curve *1*) and b) a power dependence $I=b_1V^{n_1}+b_2V^{n_2}$ with $n_1=1$–1.3 and $n_2=2.8$–3.4 (curves *3* and *4*).

We postulate that this behavior is caused by the binary injection of nonequilibrium carriers into the n^0 layer, with the diffusion mechanism of current transport predominating in the first case and the drift mechanism predominating in the second. The current–voltage characteristic at 78 K confirms this assumption (curves *2* and *5*). Curve *2* has a short section with $I\sim V^2$, after which the characteristic has a cutoff, which leads to an S-shaped characteristic, followed by a breakdown section with $I\sim V^6$. In group ''b'' structures, the forward and reverse branches have two sections with $n_1=3$ and $n_2=6$. The S-shaped current–voltage characteristic is caused by modulation of the lifetime of the carriers injected into the n^0 layer as a result of the presence of a high density of hole trapping centers.

The condition for complete filling of trapping levels[5] $V_t=qN_tw^2/\varepsilon$ with $V_t=1$ V for an n^0 layer of thickness $w=4\times10^{-4}$ cm and $\varepsilon=12$ gives a density of centers $N_t=5\times10^{14}$ cm^3. The dependence $I\sim V^{2.8-3.4}$ reflects the dielectric relaxation of carriers injected into the n^0 layer. The deviation from the theoretical curve $I\sim V^3$ is either caused by a decrease in the effective base length w ($n_2>3$) or by an increase ($n_2<3$), depending on how ideal the injecting contacts are.[6] It is important to note that dielectric relaxation takes place when the base transit time t_{tr} is shorter than the Maxwellian relaxation time and the lifetime τ_p.

Figure 2 gives the photocurrent as a function of the forward bias for type ''a'' structures with an exponential current–voltage characteristic and as a function of the forward and reverse bias for type ''b'' structures. In the first case, the maximum gain for $\lambda=1.2$ μm illuminating radiation was ~200 and decreased with increasing λ: for $\lambda=1.6$ μm it decreased by 30% and for $\lambda=1.9$ μm by 60%. This behavior was attributed to an increase in the photocurrent at zero bias. The gain of the ''b'' structures was substantially lower (~25) and did not depend on wavelength. The photocurrent in the ''a'' structures increases approximately exponentially as a function of forward bias between 0.3 and 0.6 V. Unlike the experimental data reported in Ref. 4, the structures studied exhibited no gain at low forward bias or when reverse-biased.

We postulate that the exponential increase in the photocurrent $I_{ph}\sim\exp(qV/nkT)$ with $n=2.3$ is caused by binary injection under diffusion conditions where the photocarrier lifetime varies with the level of injection. In this case, we have $n=\cosh(w/L)$ (for $w>L$), where L is the length of

 © 1998 American Institute of Physics

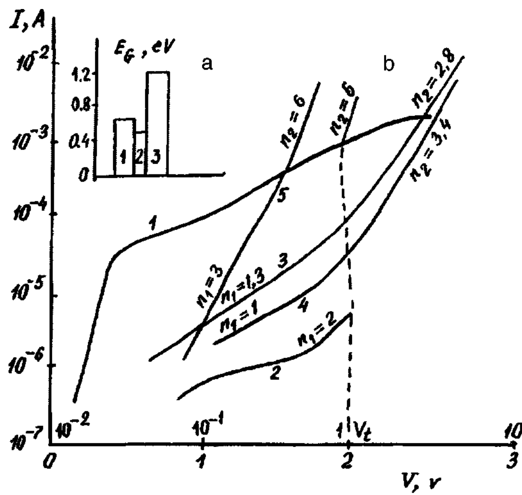

FIG. 1. a — Band profile of n^+–GaSb–n^0–GaInAsSb–n^+–GaAlAsSb heterostructure; b — current–voltage characteristics. Structure ''a'': *1* — forward branch $\log I = f(V)$, $T=300$ K; *2* — characteristic at $T=78$ K, $\log I = f(\log V)$. Structure ''b'': *3* and *4* — forward and reverse branches of current–voltage characteristic $\log I = f(\log V)$, *5* — characteristic at $T=78$ K.

diffusive displacement. For $\mu_n \sim 10^3$ cm$^2 V^{-1} s^{-1}$, we have $w/L = 1.5$. Modulation of the nonequilibrium carrier lifetime is caused to a greater extent by trapping at deep levels rather than in the potential well of the valence band offset at the heterojunction, although the latter is not completely eliminated. In group ''b'' samples this factor is negligible. For these samples, at low bias (Fig. 2, curve *2*) the photocurrent typically decreases with increasing voltage and then begins to increase, reaching a maximum under conditions of dielectric relaxation with $I \sim V^{2.8-3.4}$. This is because, for a high density N_t, the probability of injected dark and optical carriers undergoing intensive trapping and recombination is higher in comparison with group ''a'' and their lifetime falls sharply. Increased injection of dark carriers leads to filling of trapping centers, which reduces the recombination of optical carriers and enhances their lifetime. This results in amplification of the photocurrent owing to the ''transit'' effect of the n^0 layer when the gain is defined as $\tau/t_{\rm tr}$ and $t_{\rm tr} = w^2/\mu_n V$. If it is assumed that we have for the n^0 layer $\mu_n = 10^3$ cm^2 $V^{-1} s^{-1}$, $w = 4 \times 10^{-4}$ cm, and $V = 1$ V, we

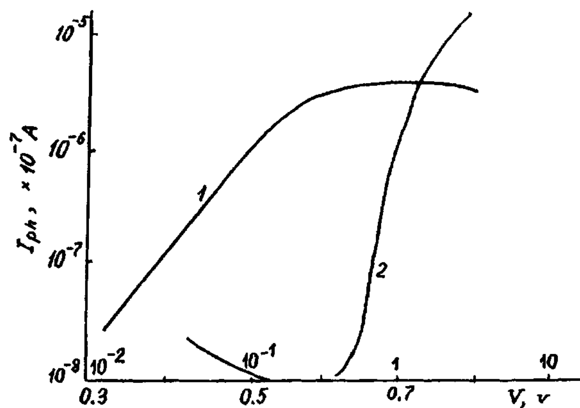

FIG. 2. Photocurrent versus bias. Structure ''a'': *1* — forward bias $\log I_{\rm ph} = f(V)$; structure ''b'': *2* — reverse bias $\log I_{\rm ph} = f(\log V)$.

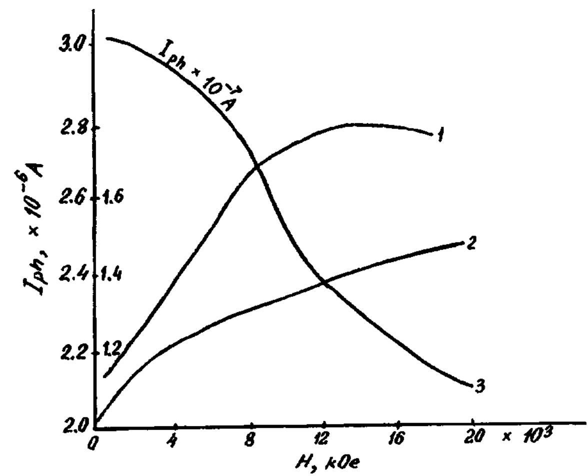

FIG. 3. Photocurrent versus magnetic field. Structure ''a'': *1*—illuminated by $\lambda = 1.8$ μm light, *2*—illuminated by $\lambda = 1.2$ μm light (right-hand scale on ordinate); structure ''b''—illuminated by $\lambda = 1.7$ μm light.

obtain $t_{\rm tr} = 8 \times 10^{-11}$ s, which gives $\tau = 2 \times 10^{-9}$ s. Amplification is observed on the forward and reverse branches of the current–voltage characteristic although its value for the same bias is naturally lower in the second case and reaches the same maxima at voltages more than twice as high.

The influence of the magnetic field on the photocurrent (Fig. 3) is quite different and may indicate the type of amplification mechanism. For structures with a diffusion mechanism of current transport a 40–50% increase in the photocurrent is observed for $H = 20$ kOe, whereas for structures with a drift current, the photocurrent is reduced by 20%. In the first case, the increase in the photocurrent may be caused by an increase in the gradients dn/dx and dp/dx since the Hall field of the dark carriers ''compresses'' the diffusion fluxes, impeding flow parallel to the plane of the heterostructures.

In the second case, the magnetic field reduces the diffusive displacement length of the electron–hole plasma carriers in the n^0 layer as a result of additional scattering which increases the transit time $t_{\rm tr}$.

These experimental results suggest that several amplification mechanisms may be present in n^+–GaSb–n^0–GaInAsSb–n^+–GaAlAsSb heterostructures, depending on the specific technological fabrication conditions.

[1] A. A. Popov, V. V. Sherstnev, Yu. P. Yakovlev, A. N. Baranov, and C. Alibert, Electron. Lett. **33**, 86 (1997).

[2] Yu. P. Yakovlev, A. N. Baranov, A. N. Imenkov, A. A. Popov, and V. V. Sherstnev, J. Phys. (Paris) **4**, 4 (1994).

[3] I. A. Andreev, M. A. Afrailov, A. N. Baranov, V. G. Danil'chenko, M. A. Mirsagatov, M. P. Mikhaĭlova, and Yu. P. Yakovlev, Pis'ma Zh. Tekh. Fiz. **12**, 1311 (1986) [Sov. Tech. Phys. Lett. **12**, 542 (1986)].

[4] I. A. Andreev, A. N. Baranov, M. A. Mirsagatov, M. P. Mikhaĭlova, A. A. Rogachev, G. M. Filaretova, and Yu. P. Yakovlev, Pis'ma Zh. Tekh. Fiz. **14**, 389 (1988) [Sov. Tech. Phys. Lett. **14**, 173 (1988)].

[5] M. A. Lampert and P. Mark, *Current Injection in Solids* (Academic Press, New York, 1970; Mir, Moscow, 1973).

[6] É. I. Adirovich, P. M. Karageorgiĭ-Alkalaev, and A. Yu. Leĭderman, *Binary Injection Currents in Semiconductors* [in Russian], Sovetskoe Radio, Moscow (1978), Sec. 3.3, pp. 73–122.

Translated by R. M. Durham
Edited by David L. Book

A possible method of reducing the magnetic field in a relativistic backward-wave tube

I. K. Kurkan, V. V. Rostov, and E. M. Tot'meninov

Institute of High-Current Electronics, Siberian Branch of the Russian Academy of Sciences, Tomsk
(Submitted October 20, 1997)
Pis'ma Zh. Tekh. Fiz. **24**, 43–47 (May 26, 1998)

A new configuration is proposed and implemented for a relativistic backward-wave tube using the symmetric TM_{01} mode which can appreciably enhance, by a factor of 2–3, the generation efficiency of high-power 3 cm radiation pulses using low magnetic fields. © *1998 American Institute of Physics.* [S1063-7850(98)02505-1]

One possible application of a relativistic backward-wave tube (BWT) is as a source of high-power microwave pulses in nanosecond radars.[1] Efficient oscillation is achieved in strong magnetic fields, which are required to form and transport the high-current electron beam. Thus, to date, pulse-periodic operation has been implemented using superconducting solenoids. In view of the expense and maintenance difficulties, it is important to reduce the magnetic field to levels attainable in permanent magnets while maintaining the BWT generation efficiency at around 20–30% (Ref. 2).

A conventional relativistic BWT uses the TM_{01} lowest axisymmetric mode, and the average diameter of the rippled slow-wave structure is close to the wavelength. In a moderating structure of these transverse dimensions, wave selection and single-frequency oscillation are relatively easy to achieve. However, when the magnetic field is reduced, effects associated with the transverse motion of the electrons begin to play an important role. So-called cyclotron absorption of the oppositely propagating electromagnetic wave and violation of the starting conditions for oscillation are observed near the cyclotron resonance $\omega_B=\omega+k_\parallel v_\parallel$ (Refs. 3 and 4). Here $v_\parallel$ is the longitudinal electron velocity, $k_\parallel$ is the longitudinal wave number, $\omega=2\pi c/\lambda$, and $\omega_B=eB/mc\gamma$ is the cyclotron frequency. For the wavelength range $\lambda\approx 3$ cm and energies $\gamma\approx 2$, exact resonance corresponds to $B_R\approx 1.2$ T. A reduction in the efficiency is observed over a very wide range of magnetic fields $(\Delta B/B_R\sim 1)$.

This is typical of relativistic electronics, since the ratio of the power bunching parameter responsible for the transverse driving of the electrons to the inertial bunching parameter is proportional to $I_b^{1/6}\gamma^{1/2}\beta_\parallel\lambda/r_0Z^{1/3}$ (Ref. 4), where I_b is the beam current, $\beta_\parallel=v_\parallel/c$, r_0 is the average radius of the slow-wave structure, and Z is the impedance of the coupling with the spatial harmonic. This notation omits any factor which describes the radial structure of the wave, i.e., the TM_{01} mode is being analyzed. In weak fields with an induction of 0.4–0.8 T, the electron beam structure contains a fraction of particles with a high transverse velocity: $\beta_\perp^{\max}\approx E_\perp/\gamma B$ (Ref. 5), where $E_\perp$ is the electric field strength near the cathode. This gives rise to additional effects which reduce the efficiency, the most important of these being the dispersion of the electron longitudinal velocities. Resonant absorption near the second harmonic of the cyclotron frequency may also be observed. An analysis of these processes yields the conclusion that the radii of the cathode (r_c) and of the slow-wave structure must be increased and the highest possible impedances Z must be used. If increasing r_c does not sufficiently improve the quality of the electron beam, decompression in a magnetic field decreasing smoothly from the cathode to the slow-wave structure should be used to achieve a further reduction in the velocity spread.[6]

Thus, the selective excitation of the working wave is a key factor toward increasing the transverse dimensions. The selection element in the proposed BWT system using the TM_{01} mode is a resonant reflector[7] which is used to reflect the oppositely propagating wave, instead of a waveguide with an upper cutoff, i.e. a low-pass filter, with the radius $r<\nu_{01}\lambda/2\pi$ $(\nu_{01}=2.405)$. The equivalent electrical circuit to describe the mechanism for reflection of the TM_{01} mode from a special cavity is a simplified version of a band-stop filter, a parallel resonant circuit built into a discontinuity in a transmission line. The cavity geometry is formed by an axisymmetric groove of radius b and width L bordered by waveguides of radius a matched at the edges. Although rounded transitions having a radius of curvature $\approx(b-a)/2$ were used experimentally, we can assume for simplicity that the groove has a rectangular profile.

In the wavelength range $\nu_{02}/b<2\pi/\lambda<\nu_{02}/a$, where $\nu_{02}=5.52$, conditions for the existence of at least one trapped-mode oscillation TM_{02} are satisfied. The frequencies of the natural oscillations in the absence of losses may be determined similarly, as in the well-known quantum-mechanics problem of finding the energy levels in a rectangular potential well of finite depth.[8] The natural oscillation is only unique if the condition $\nu_{02}L(1-a^2/b^2)^{1/2}<2a$ is satisfied. The existence of diffraction losses and Ohmic losses causes a downward shift of the resonant frequency. Since the coupling coefficient between the natural oscillation and the TM_{01} traveling wave is a function of the step height, the diffraction Q factor may be taken to be smaller than the Ohmic Q factor: $Q_d\ll Q_0$. For copper walls and a frequency of 10 GHz, we find $Q_0\sim 10^4$. Then, in accordance with Ref. 9, the reflection coefficient at the resonant frequency is close to unity, $R\approx 1-Q_d/Q_0$.

For the experiments we used a reflector geometry which provides fairly good coverage of the generated spectrum $(Q_d\approx 10)$. It is fundamentally important that even for a relatively low Q factor, as a result of the difference in the radial

 © 1998 American Institute of Physics

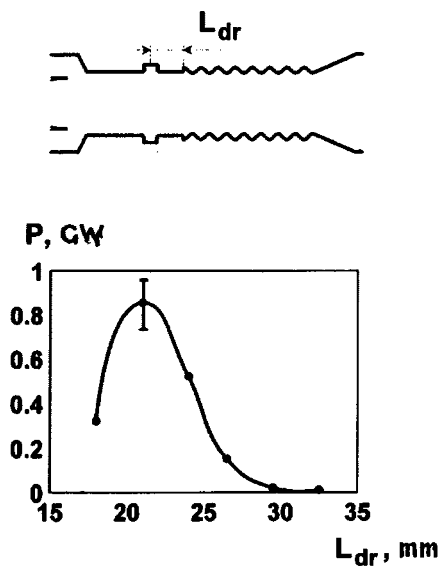

FIG. 1. Schematic of relativistic backward-wave tube with resonant reflector and experimental dependence of output power on reflector position.

distribution of the field, the z component of the electric field in the central plane of the reflector (at the radius $\approx 0.7b$) is almost an order of magnitude greater than the amplitude of the first negative spatial harmonic in the slow-wave structure. Thus, the reflector also functions as a modulating gap. The depth of velocity modulation of the electrons may be very substantial, so it is important to optimize the position of the reflector relative to the first ripple of the slow-wave structure. The choice of this distance (L_{dr} in Fig. 1) influences the evolution of beam bunching, but at the same time it cannot be arbitrary since it determines the phase difference between the modulating field and the spatial harmonic at the beginning of the slow-wave structure. A numerical analysis of a linear boundary-value problem for a BWT with preliminary electron modulation in a δ-gap revealed that if the phasing of the fields is favorable, the starting current of the generator is almost halved (the depth of modulation was chosen on the basis of real experimental conditions).

The experiments were carried out using a pulsed solenoid and the SINUS-6K electron accelerator. The maximum amplitude of the accelerating voltage could reach 600 V with an electron beam current of 5.5 kA. The current pulse length was 18 ns. As might be expected, the experimentally determined dependence of the pulse power on the distance between the reflector and the beginning of the slow-wave structure (Fig. 1) has a clearly defined optimum. The maximum microwave radiation power was 0.8 GW, which corresponds to an efficiency of 24%. The generation efficiency in a magnetic field of 0.7 T was almost the same as that in a strong

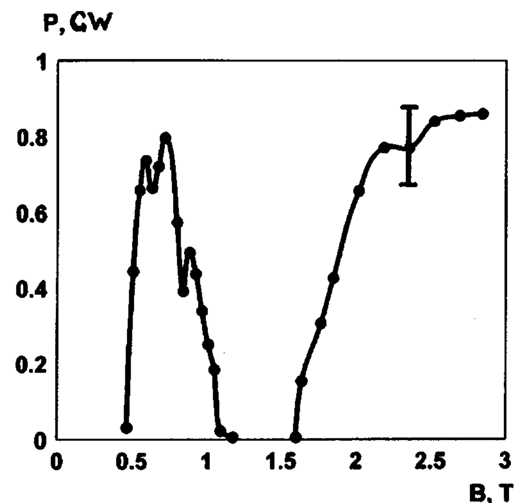

FIG. 2. Microwave radiation power versus magnetic field.

magnetic field (Fig. 2). The pulse length was around 10 ns. When electron beam decompression was used with the field at the cathode exceeding that in the moderating structure by a fixed excess of 1.4, the generation zone expanded toward weaker fields, which was observed as a shift of the left-hand boundary by approximately 20%.

To sum up, the first experiments to produce a moderately oversize BWT with a resonant reflector have shown that the efficiency in weak magnetic fields can be enhanced appreciably and the fields required can be generated using a permanent magnet.

This work was partly supported by the GEC–Marconi Research Center (UK).

[1] B. V. Bunkin, A. V. Gaponov–Grekhov, A. S. El'chaninov *et al.*, Pis'ma Zh. Tekh. Fiz. **18**(9), 61 (1992) [Sov. Tech. Phys. Lett. **18**, 299 (1992)].

[2] S. D. Korovin, V. V. Rostov, and A. V. Smorgonskiĭ, Izv. Vyssh. Uchebn. Zaved. Radiofiz. **29**, 1278 (1986).

[3] É. B. Abubakirov, V. I. Belousov, V. N. Varganov *et al.*, Pis'ma Zh. Tekh. Fiz. **9**, 533 (1983) [Sov. Tech. Phys. Lett. **9**, 230 (1983)].

[4] N. I. Gunina, S. D. Korovin, and V. V. Rostov, Abstracts of papers presented at the *Sixth All-Union Symposium on High-Current Electronics*, Tomsk, 1986, Vol. 3 [in Russian], p. 23.

[5] S. D. Korovin and I. V. Pegel', Zh. Tekh. Fiz. **62**(4), 139 (1992) [Sov. Phys. Tech. Phys. **37**, 434 (1992)].

[6] E. B. Abubakirov, M. I. Fuchs, L. G. Kolganov *et al.*, Abstracts of papers presented at the *Third International Workshop on Strong Microwaves in Plasmas*, Nizhniĭ Novgorod, Russia, 1996, p. S19.

[7] G. G. Denisov, D. A. Lukovnikov, and S. V. Samsonov, Int. J. Infrared Millim. Waves **16**, 745 (1995).

[8] L. D. Landau and E. M. Lifshitz, *Quantum Mechanics: Non-Relativistic Theory*, 3rd ed. (Pergamon Press, Oxford, 1977) [Russ. original, Nauka, Moscow, 1974]

[9] A. P. King and E. A. Marcatili, Bell Syst. Tech. J. **35**, 899 (1956).

Translated by R. M. Durham
Edited by David L. Book

Initial stages in the formation of a CsAu surface alloy

M. V. Knat'ko, M. N. Lapushkin, and V. I. Paleev

A. F. Ioffe Physicotechnical Institute, Russian Academy of Sciences, St. Petersburg

(Submitted December 23, 1997)
Pis'ma Zh. Tekh. Fiz. **24**, 48–54 (May 26, 1998)

Threshold photoemission spectroscopy is used to study the formation of a CsAu alloy during deposition of Cs on an Au substrate. It is shown that both the Cs surface layer and the CsAu near-surface alloy undergo indirect photoexcitation. It is found that the formation of a CsAu alloy is accompanied by a sharp rise (by several factors of ten) in the photoemission current while the photoemission threshold remains almost constant. This behavior is attributed to the formation of a band of electronic states near the Fermi level. © *1998 American Institute of Physics.* [S1063-7850(98)02605-6]

The interaction between alkali metal (M) atoms and gold has been studied on numerous occasions. The adsorption of alkali metal atoms leads to reconstruction of the surface layer and to the formation of M_xAu_y alloys in the near-surface region of the gold substrate.[1–6] In this case, the properties of the alloys differ substantially from those of gold metal. Alloys of CsAu are usually formed by exposing a gold substrate to cesium vapor at $T>250$ K. The CsAu alloy is formed by the diffusion of Cs atoms into the gold metal after a Cs monolayer coating has been formed.[4] The compound thus obtained has a CsCl crystal structure and a lattice constant of 4.25 Å. Moreover, CsAu is an ionic semiconductor with a band gap $E_g=2.6$ eV (Ref. 1). However, very few experimental investigations have been made of its electronic structure near the Fermi level (E_F). This is because the ultraviolet spectroscopy conventionally used for this purpose exhibits very poor sensitivity to states near E_F which are responsible for the semiconducting properties of the solid.

This shortcoming does not arise in threshold photoemission spectroscopy,[7] which has been successfully used to study the adsorption of alkali metal atoms on Cs/W (Ref. 7) and Cs/Ag metals,[8] and also on Cs/Si(111) semiconductors.[9] A characteristic feature of this method is that it can separate the surface and bulk photoemission, since the component of the electric vector $\mathscr{E}_\parallel$ of light parallel to the surface only induces bulk photoemission, while the component $\mathscr{E}_\perp$ normal to the surface induces emission mainly from the surface layer. In addition, the threshold photoemission method is sensitive to states near E_F. We used this method to study the adsorption of Cs on Au, which changes the electronic structure of the surface and near-surface layers of the gold substrate.

The experiments were carried out in an ultrahigh vacuum system at $P\approx 5\times 10^{-10}$ Torr. Gold foil of 99.99% purity was used as the substrate. The gold was purified from contaminants by heating in vacuum at $T=1100$ K for 10 h and then at $T=1100$ K in oxygen at pressure $P_{O_2}=2\times 10^{-6}$ Torr for 2 h (Ref. 10). An atomically pure flux of Cs atoms was then directed onto the Au substrate at room temperature. The coverage was assessed from the cesium deposition time t.

We recorded the following: (a) the spectral dependence of the integrated photoemission currents $I_s(h\nu)$ and $I_p(h\nu)$ using s- and p-polarized exciting light, respectively, in the energy range $h\nu=1.4$–3.5 eV for various Cs deposition times (the s-light only has the $\boldsymbol{\varepsilon}_\parallel$ component, while the p-light has both $\mathscr{E}_\parallel$ and $\mathscr{E}_\perp$ components); (b) the concentration dependence of the reflection coefficients $R_s(t)$ and $R_p(t)$ as a function of the Cs deposition time on an Au substrate for $h\nu=1.96$ and 2.81 eV. The angle of incidence of light on the sample was $\gamma=45°$.

The spectral dependence of $R_{p,s}$ for pure Au varies abruptly in the energy range $h\nu=1.4$–3.5 eV. The deposition of Cs on Au caused no change in the reflection coefficients R_s and R_p of the substrate to within 0.5% ($h\nu=1.96$ eV) and 1.5% ($h\nu=2.81$ eV) for all the deposited Cs films. Thus, these coefficients remain the same as the initial values for pure gold, which indicates that they vary negligibly as a result of processes induced by Cs adsorption. Therefore, we normalized the measured photocurrent to the same number of absorbed photons (the coefficients $R_{s,p}$ were calculated using the Fresnel formulas, using known values of the permittivity $\varepsilon_{\mathrm{Au}}(h\nu)$ (Ref. 11).

Figure 1 gives the spectral dependence of the photocurrents $I_{s,p}(h\nu)$ for various times of Cs deposition on an Au substrate. For times $t<200$ s, the photocurrents $I_s(h\nu)$ and $I_p(h\nu)$ are the same, within experimental error, over the entire spectral range. Further deposition of Cs ($t>200$ s) leads to substantial differences in the shape of these curves and the magnitude of the photocurrents in the energy range $h\nu=1.4$–2.6 eV. For short Cs deposition times, the photoemission is obviously excited from the same spatial region in the bulk of the substrate, whereas for longer deposition times, photoemission begins to be excited from the surface layer.

Since it is known that CsAu is a semiconductor, an approach proposed in Ref. 10 can be used to analyze the photocurrent spectrum. In this approach, the dependence of the photocurrent on the excitation energy near the photoemission threshold $h\nu^0$ is described by the following expression:

$$I(h\nu)=c(h\nu-h\nu^0)^n,$$

where c is a coefficient and n is an exponent whose value depends on the mechanism of photoexcitation.

 © 1998 American Institute of Physics

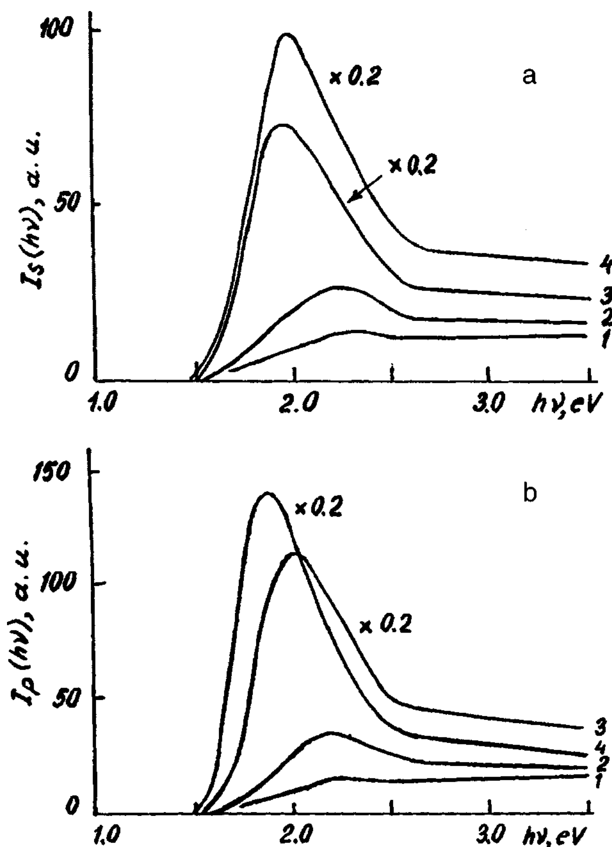

FIG. 1. Spectral dependence of the photocurrents $I_s(h\nu)$ (a) and $I_p(h\nu)$ (b) for various times of Cs deposition on Au: *1* — $t=65$ s, *2* — $t=200$ s, *3* — $t=270$ s, and *4* — $t=370$ s.

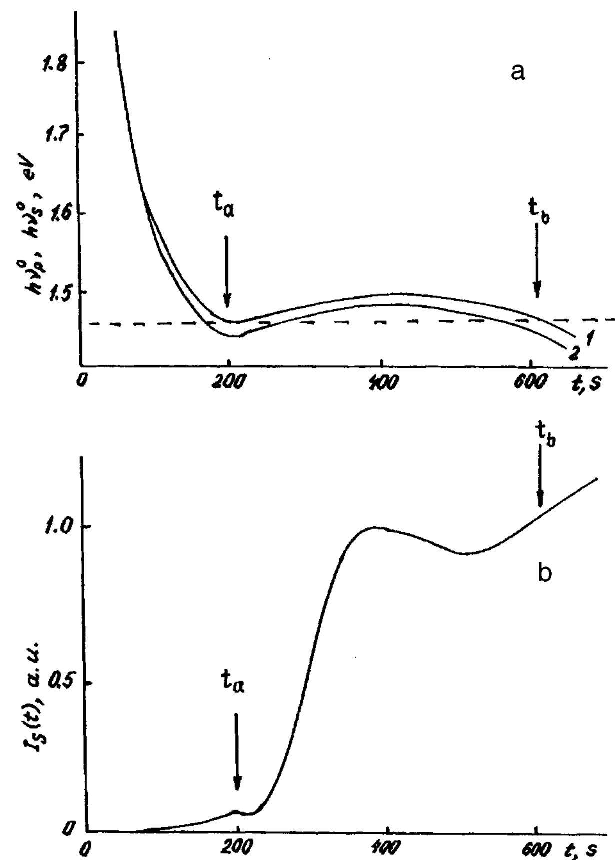

FIG. 2. a — Photoemission thresholds $h\nu_s^0$ (*1*) and $h\nu_p^0$ (*2*) versus time of Cs deposition on Au: b — photocurrent $I_s(t)$ versus time of Cs deposition on Au for the excitation energy $h\nu=1.96$ eV.

We used this approach to analyze the curves plotted in Fig. 1, and found that for cesium deposition times $t<200$ s, this exponent is $n=1$. This value of n is indicative of direct optical photoexcitation of the semiconductor structure in the bulk of the solid. In our case, this may be attributed to the initial stage of growth of the alloy into the Au substrate.

We observed that further deposition of Cs was accompanied by a change in the mechanism for the photoexcitation of emission by p- and s-polarized exciting light. For s-polarized light n increases to $n=3$, which corresponds to indirect optical excitation in the bulk of the solid. This value of n is observed for the classical Si semiconductor[13] and for the adsorption of Cs atoms on this semiconductor.[9] For p-polarized light, n increases to $n=2$ which corresponds to indirect optical transitions accompanying surface photoemission and indicates that the Cs surface layer becomes metallized. Metallization of the Cs surface layer was detected by threshold photoemission spectroscopy in a Cs/Si(100) system at submonolayer Cs concentrations.[9] In a Cs/Au system metallization of the Cs surface layer was detected by neutralization of metastable-excited atoms.[4]

Figure 2a gives the photoemission thresholds $h\nu_{p,s}^0$ as a function of the deposition time t of cesium on Au. For short Cs deposition times, the thresholds $h\nu_s^0$ and $h\nu_p^0$ are the same. For $t>100$ s, some difference can be observed between the thresholds $h\nu_s^0$ and $h\nu_p^0$. Figure 2b gives the photocurrent $I_s(t)$ as a function of the cesium deposition time for the excitation energy $h\nu=1.96$ eV. Since the s-polarized light only excites bulk photoemission, it is logical to expect that the $I_s(t)$ profile will reflect the changes in $h\nu_s^0$, as was observed in a Cs/Si(100) system.[14] In our case, it can be seen that for $t>240$ s, even negligible changes $\Delta h\nu_s\approx 0.1$ eV change the photocurrent severalfold.

For example, the times t_a and t_b correspond to the same photoemission thresholds $h\nu_s^0(t_a)=h\nu_s^0(t_b)$ although the photocurrent $I_s(t_a)$ is ten times smaller than $I_s(t_b)$. This difference can only be explained by an increase in the density ρ of electronic states involved in the photoelectron emission process. Thus, the adsorption of Cs is accompanied by an increase in ρ, i.e., by the formation of a band of CsAu electronic states in the near-surface region of the substrate as a result of growth of the alloy into the substrate. This band is positioned near and below E_F and determines the electrophysical and chemical properties of the alloy. We assume that the minimum of $h\nu_{p,s}^0$ corresponds to the formation of a monolayer Cs coating on the substrate after which the CsAu surface alloy begins to grow rapidly into the gold. This behavior is consistent with the results of Refs. 4 and 6 in which it was found that the alloy begins to form after a monolayer Cs coating has formed on the Au.

To sum up, adsorption of Cs before formation of a monolayer is accompanied by diffusion of Cs atoms into the Au substrate and by the formation of a subsurface CsAu alloy. After the CsAu alloy has been formed, the Cs surface

layer begins to become metallized and further growth of the CsAu alloy is accomplished by diffusion of Cs atoms through the already-formed alloy.

This work was supported by the Russian Fund for Fundamental Research (Project No. 96-02-16908) and by the State Program of the Ministry of Science and Technology of the Russian Federation ''Surface Atomic Structures'' (Project No. 95-2.13).

[1] W. E. Spicer, A. H. Sommer, and J. C. White, Phys. Rev. **115**, 57 (1959).
[2] H. Overhof, J. Knecht, R. Fisher *et al.*, J. Phys. F **8**, 1607 (1978).
[3] P. Münster and W. Freyland, Philos. Mag. B **39**, 93 (1979).
[4] M. S. Skottke–Klein, A. Böttcher, and R. Imbeek, Thin Solid Films **203**, 131 (1991).
[5] J. A. Rodrigues, J. Hrbeck, and Y.-W. Yang, Surf. Sci. **293**, 260 (1993).
[6] G. K. Wertheim, J. F. Rowe, and C.-M. Chiang, Surf. Sci. **330**, 27 (1995).
[7] G. V. Benemanskaya, M. N. Lapushkin, and M. I. Urbakh, Zh. Éksp. Teor. Fiz. **102**, 1664 (1992) [Sov. Phys. JETP **75**, 899 (1992)].
[8] A. Liebsch, G. V. Benemanskaya, and M. N. Lapushkin, Surf. Sci. **302**, 303 (1994).
[9] G. V. Benemanskaya, G. E. Frank–Kamenetskaya, and M. N. Lapushkin, Surf. Sci. **331–333**, 552 (1994).
[10] É. Ya. Zandberg, M. V. Knat'ko, V. I. Paleev *et al.*, Pis'ma Zh. Tekh. Fiz. **21**(19), 15 (1995) [Tech. Phys. Lett. **21**, 774 (1995)].
[11] J. H. Weaver, C. Krafka, and D. W. Lynch, Phys. Data No. 18–2 1 (1981).
[12] E. O. Kane, Phys. Rev. **127**, 131 (1962).
[13] F. G. Allen and G. W. Gobelli, Phys. Rev. **127**, 150 (1962).
[14] G. V. Benemanskaya, D. V. Daĭneka, and G. É. Frank–Kamenetskaya, JETP Lett. **65**, 729 (1997).

Translated by R. M. Durham
Edited by David L. Book

New prospects for the development of short-wavelength x-ray holography

A. M. Egiazaryan

Institute of Applied Problems in Physics, Armenian Academy of Sciences, Yerevan
(Submitted October 20, 1997)
Pis'ma Zh. Tekh. Fiz. **24**, 55–59 (May 26, 1998)

A description is given of an original proposal to use an analog of a Mach–Zehnder interferometer to record holograms in the x-ray range. © *1998 American Institute of Physics.* [S1063-7850(98)02705-0]

The implementation of short-wavelength x-ray holography is extremely important for the development of microscopy, and also for visualizing the internal microstructure of substances opaque to optical radiation. Thus, short-wavelength x-ray holography is of particular interest as a complement to electron microscopy and optical holography. The method opens up new prospects for x-ray flaw detection, holography of micro-objects, and coherent x-ray optics.

There is no doubt that certain difficulties must be overcome to implement x-ray holography. No intense sources of coherent x-rays are available. However, estimates of the coherent density of the radiation intensities of existing x-ray sources[1,2] indicate that a resolution of around $1\,\mu$m is a realistic proposition for x-ray holography. The development of x-ray interferometry and the fabrication of x-ray crystal monochromators as distinctive sources of coherent x-rays have led me to the idea of using x-ray beams diffraction-collimated in crystal monochromators for short-wavelength x-ray holography using an interference technique.[3,4]

Comparing the problem of recording x-ray interference patterns with the recording of holograms, we note that, subject to certain constraints, these patterns may be considered to be holograms and the object image may be reconstructed in visible light. Assume that an x-ray monochromatic beam having the amplitude $\psi_0^i(\mathbf{r})$ is incident on a triple-unit interferometer cut from perfect monolithic crystal at the angle of incidence (Fig. 1). If the first unit is fairly thick ($\mu t_1 \gg 1$, where t_1 is the thickness of the first unit and μ is the linear absorption coefficient of the crystal), diffraction of the primary incident wave in this unit results in the formation of almost identical waves $\psi_h(\mathbf{r})$ and $\psi_0(\mathbf{r})$, propagating in the directions of reflection and transmission, respectively.[5,6] Diffraction of these waves in units *2* and *3* produces the waves of interest to us, having the amplitudes ψ_{ho} and ψ_{oh}, which converge at the entry face of unit *3*. Diffraction and interference in unit *3* produces the beams *4* and *5*. The waves ψ_{hoh} and ψ_{ohh} propagate in the direction of beam *4*, while ψ_{oho} and ψ_{hho} propagate in the direction of beam *5*, interfering in the spatial regions where they overlap. We estimate the dimensions of the angular region α of those Fourier components of the wave $\psi_0^i(\mathbf{r})$, which, on passing through unit *1* and a vacuum layer of the same thickness t_1, are identical in the sense of acquiring the additional phase

$$\frac{kt_1(1-n)}{\cos(\theta_B+\alpha)} - \frac{kt_1(1-n)}{\cos\theta_B} < \frac{\pi}{10}, \tag{1}$$

where n is the refractive index of the crystal and θ_B is the Bragg angle.

When $t_1 \sim 10^{-1}$ cm, $k \sim 10^8$ cm^{-1}, and $1-n \sim 10^{-5}$, condition (1) yields $\alpha \sim 10^{-3}$ rad. Since the angular region of transmission of the crystal is of the same order of magnitude, for an ideal interferometer geometry the phase surfaces $\psi_0^i(\mathbf{r})$, ψ_h, and ψ_0 are similar. The experimental results (Fig. 2) show that for an ideal interferometer geometry, the interference patterns are equidistant fringes and are obtained by interference between two plane quasimonochromatic waves ψ_{hoh} and ψ_{ohh} or ψ_{oho} and ψ_{hoo}.

In this case the wave ψ_{ohh} may be considered to be the reference wave and ψ_{hoh} the object wave. Thus, these interference patterns are very simple x-ray holograms. The angle between the directions of propagation of the ψ_{hoh} and ψ_{ohh} waves is extremely small, However, so that the distance between the interference fringes is much greater than the wavelength of visible light (Fig. 2). Thus, the object wave ψ_{hoh} cannot be reconstructed from this hologram using optical laser light. In order to reduce the distance between the interference fringes to the order of the wavelength of visible light, the angle between the directions of propagation of ψ_{hoh} and ψ_{ohh} must be increased as far as possible. This can be achieved by placing a suitable homogeneous prism in the path of the reference wave ψ_{oh} which does not deflect this wave from its reflection position (see *8* in Fig. 1). The angle of deflection $\Delta\alpha$ of the wave ψ_{oh} incident normally on the entry face of the prism is given by

$$\Delta\alpha \sim (1-n)\tan\alpha, \tag{2}$$

where α is the prism angle and n is the refractive index of the prism.

The angular region of transmission of the crystal is of the order of ten arc seconds, and thus the angle between the directions of the waves ψ_{hoh} and ψ_{ohh} may be increased up to this limit in accordance with Eq. (2). Consequently, the distance between the interference fringes may be reduced to the wavelength of visible light so that the object wave ψ_{hoh} can be reconstructed by optical laser radiation. Structural modifications can be introduced In the left arm of unit *2* (in the region of diffraction of the wave ψ_h) without deflecting the wave ψ_h from its reflection position (i.e., the shaded area

 © 1998 American Institute of Physics

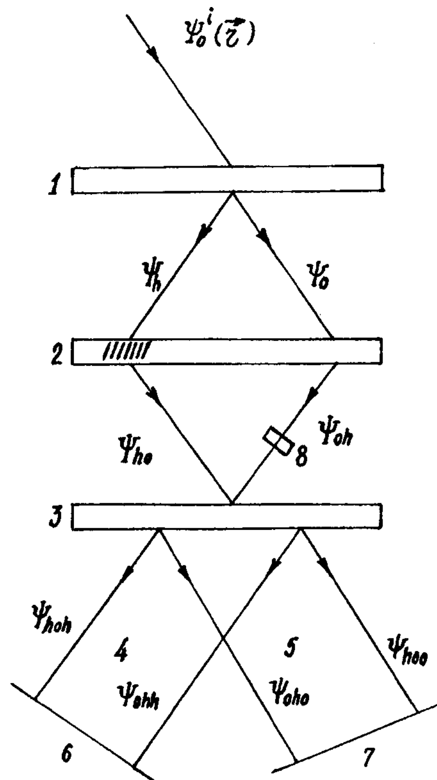

FIG. 1. Interferometer system for recording short-wavelength x-ray holograms.

in Fig. 1). A corresponding object wave ψ_{hoh} is then formed, whose phase surface is similar to that of the wave ψ_{h0} in accordance with formula (1). By reconstructing the wave ψ_{hoh} with optical laser radiation, we obtain a visible, magnified image of the inhomogeneities in the shaded part of the crystal.

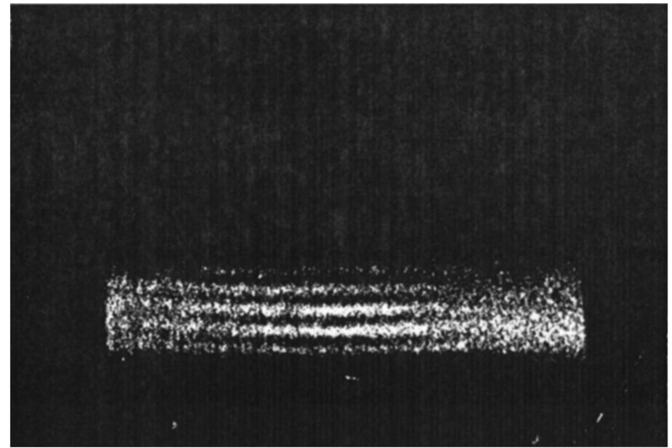

FIG. 2. Interference pattern of triple-unit interferometer with ideal geometry.

The author would like to thank F. O. Éĭramdzhyan for supplying the experimental results and for valuable discussions.

[1] V. V. Aristov and G. A. Bashkina, in *Proceedings of the All-Union Inter-University Meeting on Multiwave Scattering of X-rays* [in Russian], Yerevan State University Press, Yerevan, (1978), p. 123.
[2] R. K. Muller and S. Jorna, Appl. Opt. **16**, 525 (1977).
[3] A. M. Egiazaryan, A. G. Rostomyan, and P. A. Bezirganyan, Dokl. Akad. Nauk Arm. SSR **66**, 228 (1978).
[4] A. M. Egiazaryan and P. A. Bezirganyan, Izv. Akad. Nauk SSSR, Ser. Fiz. **15** (1980).
[5] A. M. Afanesiev and Yu. Kagan, **24**, 163 (1968).
[6] V. L. Indenbom and F. N. Chukhovskiĭ, Usp. Fiz. Nauk **107**, 229 (1972) [Sov. Phys. Usp. **15**, 298 (1972)].

Translated by R. M. Durham
Edited by David L. Book

Relation between the plasticity index and the pseudopotential of covalent tetrahedral crystals

A. F. Shchurov, V. A. Perevoshchikov, and A. V. Kruglov

N. I. Lobachevskiĭ State University, Nizhniĭ Novgorod
(Submitted October 29, 1997)
Pis'ma Zh. Tekh. Fiz. **24**, 60–64 (May 26, 1998)

On the basis of experimental results of measurements of the plasticity index of covalent crystals including Si, Ge, and III–V compounds, it is established that the low-temperature plasticity characteristics of tetrahedral crystals are related to the pseudopotential. © *1998 American Institute of Physics.* [S1063-7850(98)02805-5]

The literature now contains a wealth of theoretical and experimental results which indicate that the plastic properties of covalent crystals are related to their electronic structure.[1–7] The authors of Refs. 4 and 5 give dependences of the plasticity characteristics (such as the activation energy and dislocation velocity, critical shear stress, and hardness) on the crystal band gap (Fig. 1). It is known[6] that the dislocation velocity may be given by

$$V_d = B\tau^m \exp(-U_0/kT), \tag{1}$$

where B and m are constants and τ is the applied stress. It can be seen from Eq. (1) that as U_0 increases, the dislocation velocity decreases. Thus, as can be deduced from Fig. 1, the plasticity of covalent crystals decreases as the band gap E_g increases. In Refs. 4 and 7 the correlation between U_0 and E_g is explained by the need for covalent bonds to be broken during the motion of dislocations and by the transfer of electrons from the valence band to the conduction band.

Here we attempt to show how the low-temperature plasticity characteristics of covalent tetrahedral crystals are related to the pseudopotential.

The dimensionless parameter δ_H, known as the plasticity index, was taken as the plasticity characteristic. This index determines the fraction of plastic deformation in the total elasticoplastic deformation taking place beneath an indenter in the absence of any macroscopic damage to the material and may be given by[8]

$$\delta_H = 1 - 14.3(1-\nu-2\nu^2)HV/E, \tag{2}$$

where HV is the Vickers hardness, E is Young's modulus, and ν is the Poisson ratio. The measurements were made using a PMT-3 device.

For the investigations we used silicon and germanium elementary semiconductors and III–V compounds comprising phosphides, arsenides, and antimonides of indium and gallium. All the samples were rectangular wafers measuring at least 10×10 mm, at least 1 mm thick, with the main

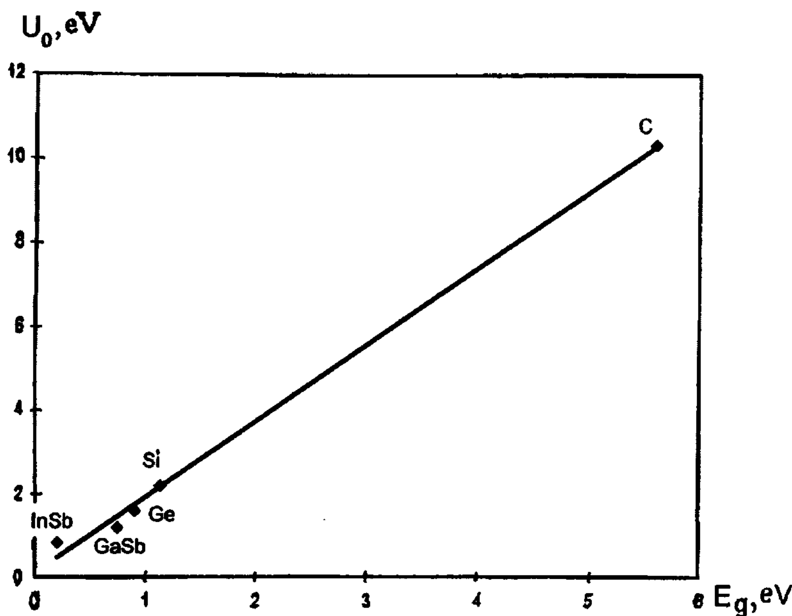

FIG. 1. Correlation between the activation energy for motion of dislocations and the band gap for covalent crystals.[4]

 © 1998 American Institute of Physics

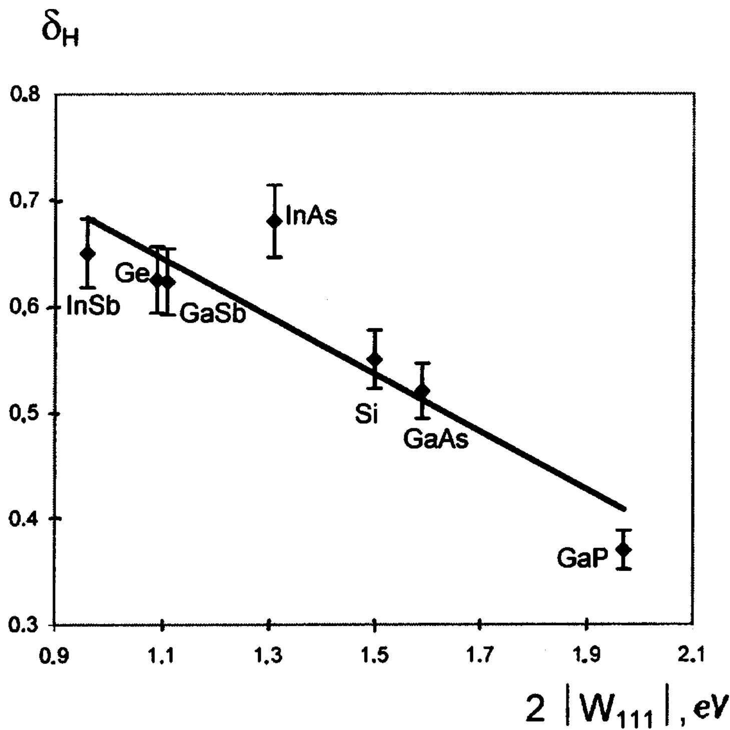

FIG. 2. Plasticity index versus pseudopotential of covalent crystals.

surface oriented in the (111) crystallographic direction for Si and Ge, and in the (111)B direction for III–V compounds. The surfaces of all the samples were treated and prepared as follows: bilateral (on the working and nonworking sides) mechanical grinding and diamond polishing was followed by chemical dynamic polishing[9] to remove the structurally damaged layer of single crystals and obtain a surface with a roughness height of $\leqslant 0.05\ \mu$m.

Microindentation can be used to determine the characteristics of low-temperature plastic deformation produced mainly by dislocation glide, without the application of high-temperature deformation processes. Almost all the data available in the literature refers to relatively high temperatures, but the low-temperature behavior remains little studied because of the brittle fracture of the materials. For low-temperature plasticity one of the present authors put forward the hypothesis that the activation energy U_0 for the motion of dislocations (Peierls barrier for $\sigma=0$) is related to the pseudopotential.[10] Here it is shown that if dislocations move conservatively through the crystal lattice, the energy for rearrangement of atoms in a dislocation center without any change in the average density is proportional to the effective spherical potential $V_{\mathrm{eff}}(r)$, which is proportional to the square of the pseudopotential $W(q)$ (Ref. 11). From this it follows that the activation energy U_0 is related to the band gap E_g since $E_g=2|W(q)|$ (Ref. 12).

Here we establish a correlation between another plasticity characteristic, the plasticity index δ_H), and the pseudopotential.

The electronic states in III–V compounds and in carbon group crystals can be conveniently described using a large Jones band whose volume is sufficient to accommodate all four electrons from each atom. The planes bounding the Jones band are (220) planes for which diffraction is weak. However, diffraction processes may cause electron transitions across the entire Jones band accompanied by a change in the electron wave vector by [111] $2\pi/a$ (Ref. 11). This corresponds to a large matrix element W_{111} which determines the band gap at point X. Thus, the gap at the (220) face is $2|W_{111}|$, and the matrix element is given by[13]

$$W_{111}=-4\pi Ze^2/V_0q^2\varepsilon(0), \tag{3}$$

where $q=2\pi\sqrt{3}/a$, Z is the number of valence electrons per atom, V_0 is the atomic volume, and $\varepsilon(0)$ is the static permittivity.

Using known experimental values of $\varepsilon(0)$ (Ref. 11), we calculated $2|W_{111}|$ and plotted the plasticity index δ_H as a function of the theoretical value of the band gap $2|W_{111}|$ calculated using the pseudopotential method (Fig. 2). A clear relationship is obtained, which indicates that pseudopotential theory may be applied to describe the plastic properties of covalent crystals.

The value of W_{111} can easily be calculated using data on the crystal and electronic structure of a material, making it possible to obtain a theoretical prediction of its plastic properties.

[1] P. Haasen, *Atomic Theory of Fracture* (New Topics in Foreign Science) [in Russian], Mir, Moscow (1987), pp. 213–235.
[2] Yu. A. Osip'yan and V. F. Petrenko, in *Physics of II–VI Compounds*, edited by A. N. Georgobiani and M. K. Sheĭnkman [in Russian], Nauka, Moscow (1986) pp. 35–71.
[3] H. Teichler, Phys. Status Solidi **23**, 341 (1967).
[4] J. Gilman, J. Appl. Phys. **46**, 5110 (1975).
[5] Yu. E. Belousova, Yu. M. Litvinov, and F. R. Khashimov, Élektron. Tekh. Ser. 6. Mater. **1**, 28 (1984).
[6] T. Suzuki, S. Takeuchi, and H. Yoshinaga, *Dislocation Dynamics and Plasticity* (Springer-Verlag, Berlin, 1991; Mir, Moscow, 1989).

[7] C. Ahlquist, M. Carroll, and P. Stroempl, J. Phys. Chem. Solids **33**, 337 (1972).

[8] Yu. V. Milman, B. A. Galanov, and S. I. Chtugunova, Acta Metall. Mater. **41**, 2523 (1993).

[9] V. A. Perevoshchikov and V. D. Skupov, *Characteristics of the Abrasive and Chemical Treatment of Semiconductor Surfaces* [in Russian], Nizhniĭ Novgorod State University Press, Nizhniĭ Novgorod (1992).

[10] A. F. Shchurov, Pis'ma Zh. Tekh. Fiz. **20**(20), 72 (1994) [Tech. Phys. Lett. **20**, 842 (1994)].

[11] W. A. Harrison, *Electronic Structure and the Properties of Solids: The Physics of the Chemical Bond*, Vol. 2 (Freeman, San Francisco, 1980; Mir, Moscow (1983).

[12] V. Heine, M. L. Cohen, and D. Weaire, in *Solid State Physics*, Vol. 24, edited by H. Ehrenreich, F. Seitz, and D. Turnbull (Academic Press, New York, 1970; Mir, Moscow 1973).

[13] O. Madelung, *Solid-State Physics. Localized States* [in Russian], Nauka, Moscow (1985).

Translated by R. M. Durham
Edited by David L. Book

Quenching of photoconduction in semiconductors with pulsating recombination activity

S. Zh. Karazhanov

Physicotechnical Institute, "Solar Physics" Scientific Industrial Association, Tashkent

(Submitted November 6, 1997)
Pis'ma Zh. Tekh. Fiz. **24**, 65–69 (May 26, 1998)

A new mechanism is proposed for the quenching of photoconduction and a negative internal photoeffect caused by the metastable nature of defects. © *1998 American Institute of Physics.* [S1063-7850(98)02905-X]

It can now be considered to be well-established that photo-, thermal-, recombination-, and exciton-stimulated transformations of metastable defects have a strong influence on the elastic, thermal, electronic, and magnetic properties of solids[1–9] and are responsible for many phenomena and effects, especially the formation of dissipative structures and the photovoltaic effect, among others. The idea that such a mechanism may be responsible for these two effects was first suggested in Ref. 1 and was confirmed experimentally.[2–7] The formation of dissipative structures was attributed to the photostimulated transformation of metastable EL2 defects in gallium arsenide in Ref. 2, to the photostimulated generation of metastable dangling bonds in hydrated amorphous silicon in Ref. 3, to the injection transformation of charge states of metastable manganese impurities in silicon in Ref. 4, to the photostimulated transformation of metastable gallium impurities in lead telluride in Ref. 5, and to photostimulated structural conversions in germanium disulfide in Ref. 6, and so on.

Here it will be shown that the metastable nature of defects may also be responsible for the quenching of photoconduction and a negative photoeffect. Since these effects have an adverse influence on the characteristics of, e.g., photoelectric solar energy converters, and metastable defects occur in many semiconductors widely used in modern photoenergetics (for example, in silicon, gallium arsenide, hydrated amorphous silicon, and so on), it is interesting to study the mechanisms responsible for the quenching of photoconduction.

An analysis is made of a semiconductor containing metastable defects with the concentration N_R^t, of which a negligible fraction N_R^a is in a recombination-active state, i.e., they exchange carriers with both allowed bands. The largest fraction of these centers, N_R^p, are in a recombination-passive state, i.e., carriers do not recombine via these centers. It is postulated that the recombination-passive centers undergo photo-, recombination-, and exciton-stimulated transformation which helps to transfer them to the recombination-active state. The centers are transformed back spontaneously.

The kinetics of the relaxation of excitation in this type of semiconductor is described by the system

$$\begin{cases} \dfrac{dn}{dt} = C_n N_R^a [n_1 f_R - n(1-f_R)] + \Phi = -U_n + \Phi, & (1) \\ \dfrac{dp}{dt} = C_p N_R^a [(1-f_R)p_1 - f_R p] + \Phi = -U_p + \Phi, & (2) \\ \dfrac{dN_R^a}{dt} = -\dfrac{N_R^a - N_{R0}^a}{\tau_N} + \Gamma, & (3) \\ N_R^t = N_R^a + N_R^p, \quad p = n + N_R^a f_R. & (4)-(5) \end{cases}$$

Here Φ is the rate of photogeneration of free carriers, Γ is the rate of stimulated conversion of recombination-passive centers to recombination-active ones, n_1 and p_1 are the statistical Shockley–Read factors related to the energy level E_R of the recombination-active center, and f_R is the degree of electron filling of N_R^a.

Let us consider the case where the activation of a passive center is stimulated by illumination. In this case, the term Γ in Eq. (3) may be expressed as $\Gamma = \varkappa \Phi^* N_R^p$, where Φ^* is the number of photons incident per unit time per unit volume, which transfer the center to the recombination-active state by photostimulation. Then Φ and Φ^* may correspond to different frequency ranges of the incident photons.

Under steady-state conditions $(dn/dt = dp/dt = de/dt$, $U_n = U_p = U)$, by linearizing Eqs. (1)–(5), we can obtain a system of algebraic equations for the small increments of the free electron concentration $\Delta n = n - n_0$, the hole concentration $\Delta p = p - p_0$, the concentration of recombination-active metastable centers $\Delta N_R^a = N_R^a - N_{R_0}^a$, and also the degree of filling $\Delta f_R = f_R - f_0$, whose solution can give

$$\Delta n = \frac{\Phi[C_p N_{R0}^a f_0 + C_n(n_0+n_1) + C_p(p_0+p_1)] - C_n C_p \varkappa \Phi^* (N_R^t - N_{R0}^a) N_{R0}^a n_0 f_0 \tau_N (1+\varkappa\tau_N\Phi^*)^{-1}}{C_n C_p N_{R0}^a [N_{R0}^a f_0(1-f_0) + (n_0+n_1) f_0 + (p_0+p_1)(1-f_0)]}, \tag{6}$$

$$\Delta p = \frac{\Phi[C_n N_{R0}^a (1-f_0) + C_n(n_0+n_1) + C_p(p_0+p_1)] - C_n C_p \varkappa \Phi^* (N_R^t - N_{R0}^a) N_{R0}^a [p_1(1-f_0)\tau_N/(1+\varkappa\tau_N\Phi^*)]}{C_n C_p N_{R0}^a [N_{R0}^a f_0(1-f_0) + (n_0+n_1) f_0 + (p_0+p_1)(1-f_0)]}, \tag{7}$$

$$\Delta N_R^a = \varkappa \tau_N \Phi^* N_{R0}^p (1+\varkappa\tau_N\Phi^*)^{-1}. \tag{8}$$

Here n_0, p_0, N_{R0}^a, and N_{R0}^p are the concentrations of electrons, holes, recombination-active, and passive centers in a thermodynamically equilibrium state. By analyzing Eqs. (6)–(8), we can easily establish that for $\varkappa\tau_N\Phi^* < 1$, Δn and

 © 1998 American Institute of Physics

Δp decrease, while ΔN_R^a increases as the rate of photostimulated transformation of metastable defects Φ^* increases, when

$$\Phi[C_p N_{R0}^a f_0 + C_n(n_0+n_1) + C_p(p_0+p_1)] > C_n C_p \varkappa \Phi^* (N_R^t - N_{R0}^a) \frac{N_{R0}^a n_0 f_0 \tau_N}{(1+\varkappa \tau_N \Phi^*)}, \tag{9}$$

$$\Phi[C_n N_{R0}^a (1-f_0) + C_n(n_0+n_1) + C_p(p_0+p_1)] > C_n C_p \varkappa \Phi^* (N_R^t - N_{R0}^a) N_{R0}^a \frac{p_1(1-f_0)\tau_N}{1+\varkappa \tau_N \Phi^*}. \tag{10}$$

Thus, the carrier lifetime τ

$$\tau = \frac{\Delta n}{U} = \frac{1}{C_p N_R}\frac{n_0+n_1}{n_0+p_0} + \frac{1}{C_n N_R}\frac{p_0+p_1}{n_0+p_0}, \tag{11}$$

obtained from Eqs. (1)–(2) under steady-state conditions decreases, which supports the evolution of an optical photoconduction quenching effect. For high rates of photostimulated conversions of metastable defects to the recombination-active state, inequalities (9)–(10) are not satisfied. Thus, the increments of the electron and hole concentrations, Δn and Δp given by Eqs. (6) and (7) respectively, become negative, which implies a negative photoeffect.

It should be noted that this effect may also occur as a result of recombination- and exciton-stimulated rearrangements of metastable defects. In this case, recombination-passive centers are converted to the recombination-active state as a result of the action of the energy released by nonradiative recombination of electrons and holes, and also by exciton annihilation. The system (1)–(5) was analyzed assuming that the function Γ in Eq. (3) is $\Gamma = \varkappa^* n p N_R^p$ in the first case and $\Gamma = \varkappa e N_R^p$ in the second. Conditions for the onset of photoconduction quenching and the negative photoeffect were obtained in both cases.

This effect may also occur as a result of the influence of thermal effects when the recovery of the recombination activity of a center is thermally stimulated. In this case, the term Γ in Eq. (3) should be viewed as an increasing function of the crystal temperature. The concentration of recombination-active centers then increases with temperature, which is accompanied by a reduction in the lifetime and indicates the onset of a thermal photoconduction quenching effect.

It is known that at high temperatures defects are annealed. In this temperature range the rate of thermally stimulated activation of recombination activity Γ and the lifetime τ_N of metastable defects in Eq. (3) decrease with increasing crystal temperature, which causes a drop in N_R^a and recovery of photoconduction.

To sum up, photo-, thermo-, recombination-, and exciton-stimulated transformations of metastable defects may give rise to photoconduction quenching and a negative internal photoeffect. Under the conditions of the quenching effect, the carrier lifetime τ decreases as the rate of conversion of the metastable centers increases. This decrease in the lifetime τ reduces the short-circuit current J_{sc} and the open-circuit voltage V_{oc} of the photocells:

$$J_{sc} = q\Phi \cosh^{-1}(w/L),$$

$$V_{oc} \approx \frac{kT}{q} \ln[J_{sc} L (q D_p)^{-1} \coth(w/L)],$$

where $L = (D\tau)^{0.5}$ is the diffusion length, D is the diffusion coefficient, and w is the base length. Thus, the quenching effects ultimately lower the efficiency of semiconductor photoconverters.

The author would like to thank Prof. A. Yu. Leĭderman for useful discussions of this work.

[1] P. M. Karageorgy-Alkalaev and A. Yu. Leiderman, Phys. Status Solidi A **100**, 221 (1987).
[2] I. A. Buyanova, A. U. Savchuk, and M. K. Sheĭnkman, Pis'ma Zh. Tekh. Fiz. **16**(2), 40 (1990) [Tech. Phys. Lett. **16**, 59 (1990)].
[3] B. G. Budagyan and O. N. Stanovov, Pis'ma Zh. Tekh. Fiz. **18**(12), 88 (1992) [Sov. Tech. Phys. Lett. **18**, 401 (1992)].
[4] K. S. Ayupov and N. F. Zikrillaev, Dokl. Akad Nauk Uz. SSR No. 8–9, 41 (1992).
[5] V. M. Lyubin and V. K. Tikhomirov, JETP Lett. **55**, 25 (1992).
[6] B. A. Akimov, N. B. Brandt, A. V. Albul, and L. I. Ryabova, Fiz. Tekh. Poluprovodn. **31**(2), 197 (1997) [Semiconductors **31**, 100 (1997)].
[7] D. M. Zayachuk, JETP Lett. **54**, 394 (1991).
[8] É. A. Manykin and S. S. Makhmudov, Zh. Éksp. Teor. Fiz. **101**, 1312 (1992) [Sov. Phys. JETP **74,** 704 (1992)].
[9] V. I. Emel'yanov, Izv. Ross. Akad. Nauk, Ser. Fiz. **60**, No. 6, 121 (1996).

Translated by R. M. Durham
Edited by David L. Book

Laws governing dilatational contrast transmission electron microscope images and the accuracy of models of nonequilibrium ordering in III–V compositions

K. S. Maksimov and S. K. Maksimov

Moscow Institute of Electronic Technology
(Submitted September 15, 1997)
Pis'ma Zh. Tekh. Fiz. **24**, 70–75 (May 26, 1998)

Expressions are given for the fields of the elastic displacements and the elastic component of the excitation error for a composition-modulated crystal. Calculated and experimental dilatational contrast transmission electron-microscope images are compared for a spontaneously modulated GaAsP/GaAs composition. It is demonstrated that the experimental images correspond to continuous variations in the composition which are possible in a "synergistic" model of nonequilibrium order. © *1998 American Institute of Physics.* [S1063-7850(98)03005-5]

Epitaxy of III–V compounds is accompanied by nonequilibrium ordering:[1–3] compositional self-modulation[1–3,5] and atomic order.[3,6] These two types of ordering are explained using different models,[3,5] and it has been shown that atomic order is associated with surface reconstruction.[3] Both types of ordering are observed in the same structures and in the same processes.[2] Thus, in Refs. 7 and 8 they were interpreted in terms of a unified model based on the assumption that surface reconstruction increases the mixing energy (Ω). This hypothesis contradicts that put forward in Ref. 2, where the atomic order in III–V compounds is attributed to a decrease in Ω caused by this reconstruction. The hypothesis put forward in Ref. 2 was confirmed by molecular dynamics calculations using a pseudopotential[6] although these calculations contain various assumptions. Thus, the question as to whether the interpretation, from Refs. 3 and 6 or that from Refs. 7 and 8 is correct needs to be resolved experimentally.

It is easier to check experimentally the self-modulation behavior, for which the model described in Refs. 7 and 8 competes with the model of conjugating phases, which attributes self-modulation to equilibrium spinodal decomposition.[9–11]

We studied the compound $GaAs_{1-y}P_y(001)GaAs$, obtained from the vapor phase[1,3] and consisting of a layer of length $\approx 20\ \mu$m formed by continuously increasing the fraction of GaP from $y=0$ to $y=0.4$, and a layer for which the growth conditions should give $y=\text{const}=0.4$. At this composition, spontaneous oscillation of the composition occurs in the [001] direction of growth, with a period of a hundreds of nanometers and an amplitude Δx of several mol.% (Ref. 1) so that the modulation can be studied using transmission electron microscope (TEM) images.

The contrast of a TEM image is determined by the variation of the excitation error w (Ref. 12):

$$w=w_e+w_B,$$

where w_e is the component of the total error caused by elastic deformations of the grating and w_B is caused by deviations of the crystal from the exact Bragg condition.

On the basis of Ref. 13, the displacements in an object consisting of two elastically connected volumes with varying lattice parameters are described by

$$\mathbf{u}=\varepsilon_{yy}(\mathbf{x}_c-\mathbf{X}_m)+\frac{1+\sigma}{1-\sigma}\mathbf{e}_1'\left[\int_0^{(\mathbf{x}_c-\mathbf{X}_m)\cdot\mathbf{e}_1'}\frac{\Delta a}{a_0}dx' - \varepsilon_{yy}((\mathbf{x}_c-\mathbf{X}_m)\cdot\mathbf{e}_1')\right], \quad (1)$$

where $\mathbf{u}$ is the displacement vector, ε_{yy} is the constant strain over the entire object in the directions perpendicular to the direction of variation of the lattice, $\mathbf{x}_c$ is the vector of the instantaneous point, $\mathbf{X}_m$ is the vector of the point lying on the interface at the center of the crystal, σ is the Poisson ratio, $\mathbf{e}_1'$ is the unit vector in the direction of variation of the composition, Δa is the variation of the lattice parameter, and a_0 is the averaged lattice parameter.

Expression (1) can be used to calculate w_e:

$$w_e=\xi_g\left[\frac{1+\sigma}{1-\sigma}(\mathbf{g}_0\cdot\mathbf{e}_1')\left(\mathbf{B}\cdot\mathbf{e}_1'+\theta_0\frac{\mathbf{g}_0\cdot\mathbf{e}_1'}{g_0}\right)\times\left(\frac{\Delta a}{a_0}-\varepsilon_{yy}\right)+\theta_0\varepsilon_{yy}g_0\right], \quad (2)$$

where ξ_g is the extinction distance, $\mathbf{g}_0$ is the effective diffraction vector of the averaged grating, $\mathbf{B}$ is the unit vector in the direction of the electron beam, and θ_0 is half the scattering angle. For the calculations we took $\sigma=0.32$.

Two types of TEM images are observed for GaAsP/GaAs. If the direction of modulation lies in the plane of the image, the TEM images possess dilatational contrast.[14,15] If this direction is inclined relative to this plane, images of inclined boundaries are obtained at which a specific interference contrast is formed by interference between waves scattered by different sections of the bicrystal.[14]

For the dilatational-contrast TEM images used in the present study, it can be shown that if the thickness and excitation error w_B are constant, the light sections correspond to regions with a higher fraction of GaAs and that similar compositions have the same intensity level.

 © 1998 American Institute of Physics

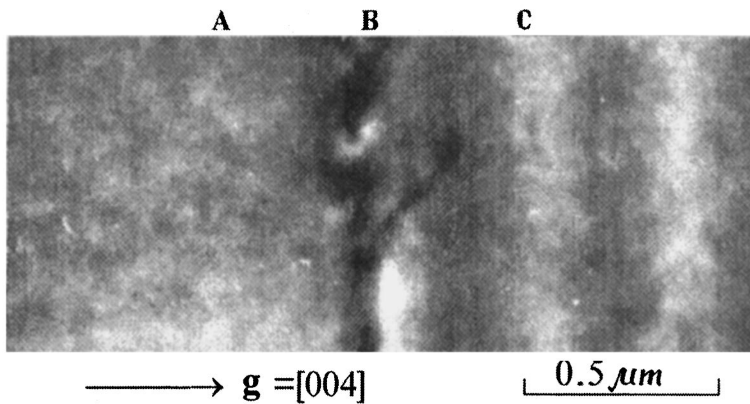

FIG. 1. Section of GaAsP/GaAs heterocomposition, [110] projection, dark field, A — unmodulated section of GaAsP layer; B — second misfit network, and C — region of spontaneous compositional modulation.

As we move in the [001] direction of growth from the GaAs substrate to the epitaxial $GaAs_{1-y}P_y$ layer on TEM images from the 004 reflection and the (110) projection plane, the structure of the heterocomposition varies as follows.[1,2] The GaAs substrate contains no structural defects. The substrate/epitaxial layer interface is indicated by the first misfit network. A section free from modulation extends from the heterojunction to a depth of $\approx 5\ \mu$m in the epitaxial layer. The second misfit network occurs at the interface between the unmodulated and spontaneously modulated volumes (Fig. 1). Intensity oscillation caused by compositional modulation is observed for the layer of varying composition and for the layer with $\langle y \rangle = 0.4$ (Fig. 1 and 2).

As the distance from the heterojunction increases and the ratios between the molar fractions of GaAs and GaP vary, the oscillation period changes, as does the ratio between the total length of the sections enriched in GaAs or GaP, but the amplitude of the intensity oscillation (which is proportional to the amplitude of the variations in composition) remains almost constant over the length of the modulated composition (Fig. 2), which is consistent with both the models being compared. The existence of an initial unmodulated layer is also consistent with both models of self-modulation.

If the differences in the intensity levels on the TEM images of the layer preceding the second misfit network and the contours on the images of the modulated structure are exclusively assigned to differences in the compositions, in the GaAs-enriched domains the content is higher than in the layer preceding the network, which is consistent with the model described in Refs. 7 and 8. This conclusion requires confirmation, however, because the volumes separated by the misfit network are strained differently.

In Fig. 2 the intensity oscillates smoothly. The TEM images in the 220 reflection where the dilatational contrast is suppressed, reveal variations in contrast caused by grooving of the surface, which can also be seen in Fig. 1, but the scale of these variations is much smaller than the oscillation period and the grooving is not periodic. Thus, the smoothness of the intensity oscillation cannot be attributed to variations in the thickness of the object synchronous with variations in the composition. This smoothness of the intensity oscillation also cannot be explained by surface relaxation, since the influence of the surface sharpens the intensity variation on the dark-field TEM images, even with sinusoidal variations in the composition.[16] For the dilatational TEM images, the smoothness of the intensity oscillation reflects the continuity of the variations in the lattice period, i.e., is caused by continuous variations in the composition.

The model described in Refs. 7 and 8 has two stages of parabolic variations in composition and two abrupt stages.

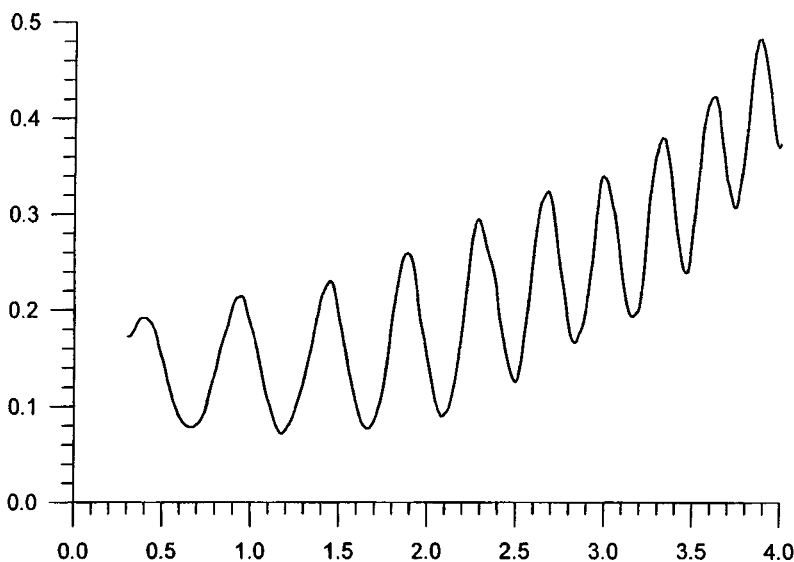

FIG. 2. Intensity profile in [001] direction; dark field using $1\bar{1}3$ reflection, [110] projection, x axis — distance in μm; y — relative intensity; the profile was obtained by averaging more than 400 individual scans; the increase in the average intensity level toward the right edge is caused by a variation in w resulting from bending of the foil; in the section for which the profile is plotted, the molar fraction of GaP increases by $\approx 10\%$. As the composition varies, the oscillation period changes but the amplitude remains almost constant.

Spinodal decomposition leads to the formation of two phases of constant composition separated by a transition region, whose length is determined by the interatomic interaction distance, i.e., does not exceed ≈ 1 nm (Ref. 13).

Modeling the TEM images of objects whose composition varies as in the model described in Refs. 9–11, even with transition regions of tens of nanometers, shows that this model cannot be used to explain the smooth intensity oscillation. The observed characteristics of dilatational TEM images are more consistent with the model from Refs. 7 and 8, especially the variant where parabolic variations in composition within compositional domains exceed abrupt variations at domain boundaries.

[1] S. K. Maksimov and E. N. Nagdaev, Dokl. Akad. Nauk SSSR **245**, 1369 (1979) [Sov. Phys. Dokl. **24**, 297 (1979)].
[2] S. K. Maksimov, AIP Conf. Proc. **117**, 491 (1991).
[3] J.-P. Chevalier and R. Portier, AIP Conf. Proc. **117**, 453 (1991).
[4] S. K. Maksimov, L. A. Bondarenko, A. S. Petrov, and V. V. Kuznetsov, Fiz. Tverd. Tela (Leningrad) **24**, 628 (1982) [Sov. Phys. Solid State **24**, 355 (1982)].
[5] S. K. Maksimov, Kristallografiya **39**, 315 (1994) [Crystallogr. Rep. **39**, 269 (1994)].
[6] J. E. Bernard, S. Froyen, and A. Zunger, Phys. Rev. B **44**, 1178 (1991).
[7] S. K. Maksimov, K. S. Maksimov, and É. A. Il'ichev, JETP Lett. **63**, 433 (1996).
[8] K. S. Maksimov and S. K. Maksimov, Pis'ma Zh. Tekh. Fiz. **22**(4), 60 (1996) [Tech. Phys. Lett. **22**, 160 (1996)].
[9] I. P. Ipatova, V. G. Malyshkin, A. Yu. Maslov, V. A. Shchukin, Fiz. Tekh. Poluprovodn. **27**, 285 (1993) [Semiconductors **27**, 158 (1993)].
[10] S. Mahajan, Mater. Sci. Eng., B **32**(3), 187 (1995).
[11] L. González, Y. Gonzáles, G. Aragón *et al.*, J. Appl. Phys. **80**, 3327 (1996).
[12] *Electron Microscopy of Thin Crystals*, edited by P. B. Hirsch, A. Howie, R. B. Nicholson, D. W. Pashley, and M. J. Whelan (Plenum Press, New York, 1965; Mir, Moscow, 1968).
[13] A. G. Khachaturyan, *Theory of Phase Transitions and Structure of Solid Solutions* [in Russian], Nauka, Moscow (1974).
[14] S. K. Maksimov and E. N. Nagdaev, Phys. Status Solidi A **68**, 645 (1981).
[15] S. K. Maksimov and E. N. Nagdaev, Phys. Status Solidi A **69**, 505 (1982).
[16] M. M. J. Treasy, J. M. Gibson, and A. Howie, Philos. Mag. A **51**, 380 (1985).

Translated by R. M. Durham
Edited by David L. Book

Measurement and stabilization of the energy parameters of laser radiation using nonlinear optical effects[1)]

B. N. Morozov

All-Russia Scientific-Research Institute of Physicotechnical and Radio Engineering Measurements, Mendeleevo, Moscow Province

(Submitted July 8, 1996; resubmitted March 6, 1997)
Pis'ma Zh. Tekh. Fiz. **24**, 76–79 (May 26, 1998)

A new method is reported for the measurement, stabilization, and control of the energy parameters of laser radiation based on the optical rectification effect and the photogalvanic effect. It is proposed to use the same nonlinear optical crystal mounted inside a laser cavity for harmonic generation, as a voltage or current detector, and also as a modulator. A brief comparison is made with earlier methods. © *1998 American Institute of Physics.* [S1063-7850(98)03105-X]

A well-known method[1] of stabilizing the power P of pulsed laser radiation is based on the optical rectification effect[2] using feedback systems. The voltage conversion efficiency $V_i^{(0)}/P$ in the optical rectification effect can be appreciably enhanced if the nonlinear optical crystal is mounted inside the laser cavity.[3]

Here we report a new, efficient method for measurement, stabilization, and control of the energy parameters (power P and energy W) based on using the optical rectification effect inside a laser cavity. This reduces the overall size of a Q-switched laser. One of the simplest systems for controlling the energy parameters of laser radiation is shown in Fig. 1a. The optical rectification signal $V_i^{(0)}$ from a crystal capacitor *6* is passed through an amplifier *8* to an electrooptic switch *3*. This stabilizes the power $P1w$ of the fundamental-frequency laser radiation and its second harmonic $P2w$ which is generated in the crystal *4*. The $P2w$ radiation is linearly polarized by means of a Glan prism *5* inserted in a cavity formed by a nontransmitting mirror *1*, a transmitting mirror *7*, and the active element *2*. An additional pulsed voltage source U_{const} can also be connected to the switch *3*, which increases or decreases (depending on the sign of U_{const}) the output energy parameters of the laser radiation, thereby acting as a controller.

A second possible system is shown in Fig. 1b. In this case, the crystal generates the harmonic $2w$, produces (simultaneously[4] with the $2w$ second harmonic generation process) the voltage $V_i^{(0)}$ by means of optical rectification,[4] and also functions as a Q switch. In order to make sufficiently accurate calculations of the absolute or relative[2] values of the crystal nonlinear susceptibilities ij, we need to know their relationship simultaneously for optical rectification,[2] second harmonic generation, and the electrooptic effect, particularly linear effects. These relationships have been established theoretically in the microwave range.[5] The nonlinear susceptibilities $\varkappa_{ij}^{(0)}$ for optical rectification depend very weakly on the laser wavelength λ (Ref. 2) and their signs can be measured experimentally.[6] The theoretical relation between $\varkappa_{ij}^{(w)}$, $\varkappa_{ij}^{(0)}$, and $\varkappa_{ij}^{(2w)}$ can be obtained from[2]

$$P_i^{(2w)}=\varkappa_{ij}^{(2w)}E_j^{(w)}E_k^{(w)} \quad \text{for the second harmonic,}$$

$$P_i^{(0)}=\varkappa_{ij}^{(0)}E_j^{(w)}E_k^{(w)} \quad \text{for the optical rectification effect,}$$

$$P_i^{(w)}=\varkappa_{ij}^{(w)}E_j^{(0)}E_k^{(0)} \quad \text{for the electrooptic effect,}$$

where P are the nonlinear polarizations.

A third version of the system is shown in Fig. 1c. A nontransmitting metallized grating-like mirror *1* in which the voltage $V_m^{(0)}$ is generated by optical rectification in the metal[7] serves as a source of fairly high current $j_m^{(0)}$ or $V_m^{(0)}$ which, after being passed through the amplifier *8*, modulates and controls (particularly stabilizes) the power P and energy W of the fundamental-frequency radiation at frequency w. In a metal the optical rectification effect is stronger than that in a nonlinear optical crystal.

In noncentrosymmetric crystals, the photogalvanic (photovoltaic) effect[8] competes with (accompanies) the optical rectification effect. The optical rectification signal does not depend on the size of the laser beam cross section, whereas

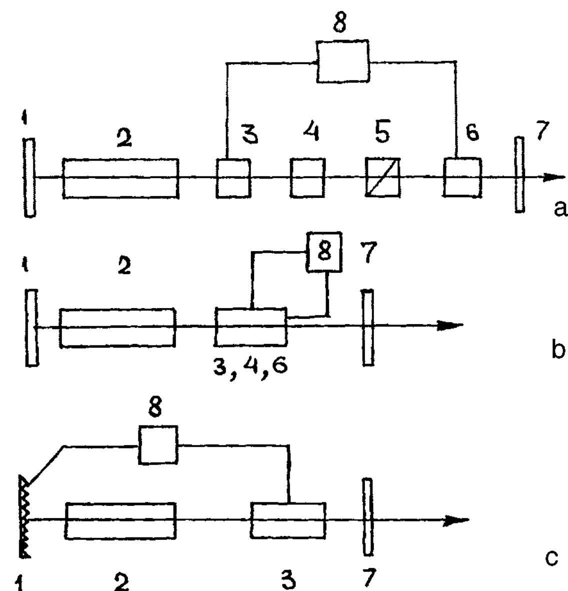

FIG. 1.

the photogalvanic effect does, so that these effects can be distinguished experimentally. The voltage (and current) produced as a result of the optical rectification effect and the photogalvanic effect in nonlinear optical crystals are of comparable magnitude. The photogalvanic effect can also occur in glasses doped with semiconductors.[9] This effect is caused by the separation of photoinduced charges in the activated glass.

The proposed autonomous method of stabilization has advantages over the method based on the nonlinear optical activity[10] in crystals, since in this last case the laser radiation intensity J does not depend linearly on the angle of rotation of the vector E in the crystal and stabilization of the power density in time and space involves 5–10% losses of the laser radiation power P incident on the crystal. When stimulated Brillouin scattering is used, measurements of the intensity J require[11] an elaborate system for recording the frequency difference by a heterodyning technique.

[1)] Presented at the Joint Conference on Coherent and Nonlinear Optics, St. Petersburg, May 1995 (Presented prior to April 15, 1995 at Moscow State University)

[1] B. N. Morozov, Kvantovaya Élektron. (Moscow) **19**, 587 (1992) [Sov. J. Quantum Electron. **22**, 540 (1992)].
[2] B. N. Morozov and Yu. M. Aĭvazyan, Kvant. Élektron. (Moscow) **7**, 5 (1980) [Sov. J. Quantum Electron. **10**, 1 (1980)].
[3] P. N. Zanadvorov, Radiotekh. Elektron. **15**, 1989 (1969).
[4] B. N. Morozov and V. É. Pozhar, Kvant. Elektron. (Moscow) **21**, 1195 (1994).
[5] Yu. V. Shaldin, *Nonlinear Optics* (in *Proceedings of the Second All-Union Symposium on Nonlinear Optics*) [in Russian], Nauka, Novorossiĭsk (1968), pp. 227–235.
[6] E. V. Pestryakov and V. M. Plyasulya, Pis'ma Zh. Tekh. Fiz. **7**, 470 (1981) [Sov. Tech. Phys. Lett. **7**, 200 (1981)].
[7] A. A. Kovalev and P. S. Kondrat'ev, Pis'ma Zh. Tekh. Fiz. **16**(7), 75 (1987) [Sov. Tech. Phys. Lett. **16**, 275 (1987)].
[8] B. I. Sturman and V. M. Fridkin, *The Photovoltaic and Photorefractive Effects in Noncentrosymmetric Materials*, Gordon and Breach, Philadelphia, 1992; Nauka, Moscow, 1992.
[9] E. M. Dianov, P. G. Kazansky, D. S. Staradubov, and D. Yu. Stepanov, Sov. Lightwave Commun. **2**(2), 83 (1992).
[10] I. N. Govor and B. N. Morozov, Zh. Tekh. Fiz. **37**(12), 2400 (1987) [Sov. Phys. Tech. Phys. **32**, 1456 (1987)].
[11] B. N. Morozov, Metrologiya No. 5, 15 (1984).

Translated by R. M. Durham
Edited by David L. Book

Interaction between relativistic charged particles and an extended strong rf field

O. P. Korovin, E. O. Popov, S. O. Popov, and I. V. Rozova

A. F. Ioffe Physicotechnical Institute, Russian Academy of Sciences, St. Petersburg
(Submitted October 16, 1997)
Pis'ma Zh. Tekh. Fiz. **24**, 80–86 (May 26, 1998)

An investigation is made of the interaction between relativistic charged particles and a high-intensity microwave electric field over long interaction lengths. The microwave field has no magnetic component over the entire interaction length. It is shown that the interaction of the relativistic particles has features which depend on the relation between the incoming particle energy and the field strength. In particular, part of a monoenergetic particle beam may be accelerated by the beam's own energy with some of the energy being transferred from the beam to the field. © *1998 American Institute of Physics.* [S1063-7850(98)03205-4]

INTRODUCTION

Progress in fundamental research in high-energy physics involves increasing the energy of the pulsed and cw power of charged particle accelerators. This in turn necessitates increasing the electromagnetic field strengths in the accelerating structures and transmission lines. The factors which determine the behavior of the charged particles in accelerating gaps at high field strengths are of decisive importance under these conditions. Increasing the field strength in systems with small drift gaps increases the probability of electrical breakdown. A large gap has a higher electrical strength and consequently, in microwave devices the output power of the device or the accelerated particle energy may be increased by enlarging the drift gap. However, studies of large gaps are few in number. It has been assumed that in this case, the particles interact inefficiently with the field. Here we shall show that under certain conditions, efficient interaction between a charged particle and an rf field may be achieved in large drift gaps. We shall study the behavior of charged particles in an extended electromagnetic microwave field as a function of the particle energy on entry to the interaction space, the input phase of the field, the oscillation frequency of the field, and the length of the interaction space. The problem will be analyzed for a microwave field with no magnetic component which is encountered, in particular, when a particle beam propagates along the central axis of a cylindrical cavity utilizing the TM_{01N} mode.

A mathematical model described in Ref. 1 was used to calculate the motion of a particle of any mass and charge.

MATHEMATICAL MODEL

The equation of motion for a particle is

$$\frac{dm\mathbf{v}}{dt}=q\mathbf{E}+q(\mathbf{v}\times\mathbf{B}), \tag{1}$$

where $m=m_0/\sqrt{1-v^2/c^2}$ is the particle mass, m_0 is the particle rest mass, $\mathbf{v}$ is the particle velocity, c is the velocity of light, q is the particle charge, $\mathbf{B}$ is the magnetic induction, and $\mathbf{E}$ is the electric field strength.

In the absence of a magnetic field, we have

$$\omega\frac{dmv}{d\vartheta}=qE_0\sin\vartheta=\frac{qV_0}{h}\sin\vartheta, \tag{2}$$

where h is the length of the interaction gap, V_0 is the amplitude of the voltage, and E_0 is the amplitude of the electric field strength.

After integrating expression (2), we introduce the function $A(\vartheta)$:

$$A(\vartheta)=\frac{\beta}{(1-\beta^2)^{1/2}}=\frac{\beta_e}{(1-\beta_e^2)^{1/2}}+\left(\frac{qV_0}{m_0c^2}\right)\left(\frac{\lambda}{2\pi h}\right)[\cos\vartheta_e-\cos\vartheta], \tag{3}$$

where $\beta=v/c$ is the electron velocity in units of the velocity of light, λ is the wavelength, β_e is the particle velocity, and ϑ_e is the phase of the microwave field at the beginning of interaction.

Equation (3) describes the particle motion in a time-varying electric field. The path covered by the particle in the accelerating gap as a function of the input phase of the microwave field is calculated using the formula:

$$S=\frac{c}{\omega}\int_{\vartheta_e}^{\vartheta_h}\frac{A(\vartheta)d\vartheta}{[1+A^2(\vartheta)]^{1/2}}. \tag{4}$$

Thus, by integrating Eq. (4) with a variable upper limit ϑ_h, we can determine when the particle leaves the interaction space.

The kinetic energy W of the particle leaving the interaction space is determined from the well-known relation:

$$W=m_0c^2[(1-\beta^2)^{-1/2}-1]. \tag{5}$$

Based on this model, a code running under Windows 95/NT was developed which can completely describe the interaction process. It can be used to calculate the interaction between particles of any mass, charge, and energy with a microwave electric field of any frequency and strength.

 © 1998 American Institute of Physics

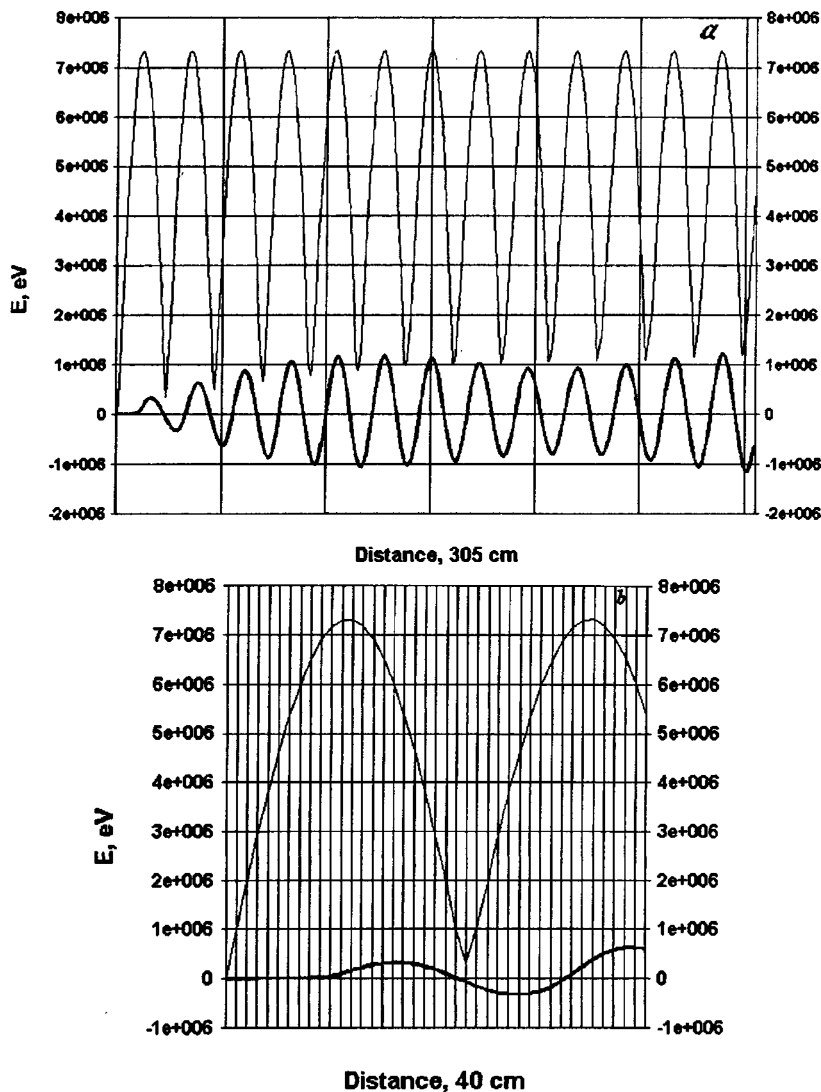

FIG. 1. Maximum energy (upper trace) and average energy (lower trace) acquired by an electron as a function of the drift gap length.

During development of the application we created dynamic link libraries and an ActiveX mathematical model.[2] The results were analyzed using multiplication.

RESULTS AND DISCUSSION

For the calculations we specified the frequency and amplitude of the microwave electric field, the electron energy on entry to the interaction space, and the phase of the field at the beginning of interaction. By varying the initial phase of the field between 0 and 360 deg at intervals of 1–3 deg, we can identify the nature of the interaction of the field with a continuous electron beam. To check the accuracy of the calculations we analyzed the interaction between a charged particle and a three-dimensional standing-wave field in a rectangular waveguide, for which this problem is a particular case. Although the programs were developed for different cases and the problems were solved by different methods, in all cases the results of the calculations agree to within at least 0.1%, which suggests that they are reliable.

The calculations were made for frequencies between 0.8 and 3 GHz in microwave fields between 100 kV/m and 100 MV/m for input electron energies between 7 keV and 700 MeV. Figures 1a and 1b give the maximum energy acquired by the electrons and the average energy received or imparted by electrons which started with input phases between 0 and 2π, plotted as a function of the length of the interaction space. The electric field strength was 100 MV/m, the frequency 1.3 GHz, and the input electron energy 7 MeV.

An analysis of the curves yields the following conclusions.

1. In a comparatively long gap of 8 cm (Fig. 1b), the electrons acquire an increased energy of 6.45 MeV or $\sim 80\%$ of the maximum possible which they would acquire in a dc field of 100 MV/m. In this case, the total energy transferred from the field to the electrons is close to zero, i.e., the electrons are accelerated by the energy of other beam electrons. This observation may be of interest for superconducting cavities.

2. When the length of the drift gap is half the wavelength, the electrons are sorted into fast and slow, depending on the input phase. The electrons exiting in the bunch which started near zero input phase subsequently remain the most energetic.

3. For relativistic electrons, the maximum energy ac-

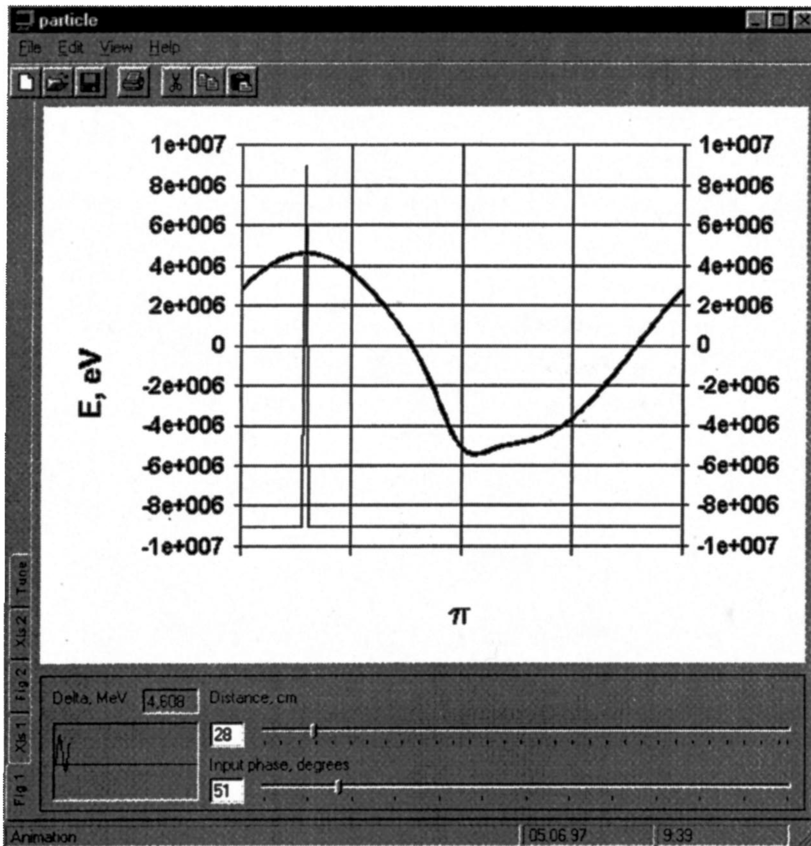

FIG. 2. Particle energy distribution as a function of input phase of field in the range between 0 and 2π over a length of 28 cm.

quired by the electrons in the section equal to half the wavelength is 63.4% of the energy increment which they would have acquired in this section in a dc field whose strength is equal to the amplitude of the ac field.

4. As the electrons propagate in the field, after each section of length equal to the wavelength, they acquire a maximum energy of ~7.3 MeV, the same as the first maximum, to a high degree of accuracy (Fig. 1a).

5. Of particular interest is an accelerating gap whose length is ~5/4 of the wavelength of 28 cm (Fig. 1b). In this gap the most highly accelerated electrons acquire an additional energy of ~4.6 MeV. For this case, the electrons which started in one period, on average transfer an energy of $\geqslant$200 keV per period to the field. Figure 2 shows the electron energy distribution at the exit from a gap 28 cm long as a function of the input phase. This implies that energy is transferred from the electrons to the field, accompanied by the acceleration of some of the electrons, i.e., the electrons are accelerated by the electron beam energy itself. A similar effect can be observed in large drift gaps only for relativistic electrons. For example, in a 32.4 cm long drift gap the electrons acquire an energy of 7.1 meV entirely from the energy of other electrons, without acquiring energy from the field.

These calculations have shown that under certain conditions in large drift gaps, electrons may interact efficiently with a microwave field and may be accelerated by the electron beam energy itself. These characteristics are only typical of relativistic electrons.

The authors would like to than V. O. Naĭdenov for useful discussions and interest in this work and K. V. Vereshchagin for helping to debug the program.

[1] P. D. Coleman, J. Appl. Phys. **28**, 927 (1957).
[2] E. O. Popov and S. O. Popov, Pis'ma Zh. Tekh. Fiz. **23**(17), 48 (1997) [Tech. Phys. Lett. **23**, 677 (1997)].

Translated by R. M. Durham
Edited by David L. Book

Influence of nitrogen on the optical and mechanical properties of diamond-like carbon films

N. I. Klyuĭ

Institute of Semiconductor Physics, Ukrainian National Academy of Sciences, Kiev

(Submitted December 3, 1997)
Pis'ma Zh. Tekh. Fiz. **24**, 87–92 (May 26, 1998)

Optical and mechanical properties of diamond-like carbon films grown by chemical vapor deposition were investigated as a function of the nitrogen content in the gas mixture. The nonmonotonic variation of the optical band gap and the microhardness of the films are interpreted using a model which allows for the influence of nitrogen on their structure. It is shown that nitrogen-containing diamond-like carbon films hold out promise as protective and antireflection coatings for silicon solar cells. *© 1998 American Institute of Physics.* [S1063-7850(98)03305-9]

Studies of diamond-like carbon films are attracting considerable interest because of the prospects for using these as protective and antireflection coatings in modern optoelectronics devices.[1,2] At the same time, diamond-like carbon films can be used to reduce the work function of field emitters,[3] to fabricate light-emitting structures,[4] to modify the properties of porous silicon[5] and in other applications. The properties of these films can be varied widely by varying the deposition conditions. In chemical vapor deposition (CVD), which is widely used to deposit diamond-like carbon films, one of these parameters is the gas composition in the reaction chamber. It has been shown in various studies that the properties of these films are substantially influenced by nitrogen even when this is added to the gas mixture in small quantities.[6,7] However, since different methods and deposition regimes were used, the mechanism responsible for the influence of nitrogen on diamond-like carbon films has not been definitively established and the results are frequently contradictory. Thus, studies of the influence of nitrogen on the optical and mechanical properties of diamond-like carbon films are undoubtedly of interest, and this is the aim of the present study. In addition, the optical and mechanical properties mainly determine the fields of practical application of these films, for instance as protective and antireflection coatings for solar cells.

The diamond-like carbon films used here were deposited from a capacitive rf discharge plasma (13.56 MHz) at a low gas pressure in the reaction chamber ($P=0.2$–0.8 Torr). The working mixture was a mixture of CH_4:H_2:N_2 gases and films containing different amounts of nitrogen were obtained by gradually replacing hydrogen with nitrogen at a fixed rf bias across the substrate (1990 V) and at room temperature. The optical properties of the films were investigated using a spectral ellipsometer with a rotating analyzer in the spectral range 1.5–5.5 eV. The well-known Tauc relation was used to determine the optical band gap E_{opt} from the measured spectral dependence of the optical constants. The refractive index n, extinction coefficient k, and film thickness d at $\lambda=632.8$ nm were determined using an LÉF-3M laser ellipsometer. The mechanical properties of the films were investigated using a Nano Indenter-2 (Nano Instruments Inc, Knoxville, USA). The average values of the microhardness H were determined by averaging over ten measurements. For the investigations we used a Berkovich indenter with a 0.1 g load. All the experiments were carried out at room temperature.

Figure 1a gives E_{opt} as a function of the nitrogen content in the gas mixture P_{N2}. It can be seen that when nitrogen is added to the gas mixture in concentrations up to 10–15%, E_{opt} decreases but as P_{N2} increases further, E_{opt} begins to increase and for $P_{\mathrm{N2}}=40\%$ reaches 3.96 and 2.2 eV for films grown at gas pressures $P=0.8$ and $P=0.2$ Torr in the reaction chamber, respectively. In contrast, the microhardness of the films (see Fig. 1b) initially increases for $P_{\mathrm{N2}}<15\%$ and then decreases again when $P_{\mathrm{N2}}>15\%$. This nonmonotonic behavior of E_{opt} and H is attributed to the influence of nitrogen on the structure of the films and may be explained using the following model. When the nitrogen content in the gas mixture and thus in the film is negligible, the nitrogen atoms are mainly incorporated at the boundaries of sp^2 clusters. In this case, by impairing the symmetry of the graphite rings, the nitrogen leads to an increased content of the sp^2 disordered phase in the film.[6,7] This should reduce E_{opt} and increase the microhardness, as was observed experimentally.

This conclusion is supported by an increase in n and k when P_{N2} increases to 15–20% (these results are not given). As P_{N2} increases further, the excess nitrogen begins to become incorporated between sp^2 clusters, leading to a reduction in the internal mechanical stresses and stimulating the formation of sp^3 coordination carbon–hydrogen bonds. In this case the films become less dense and more transparent, which is observed as an increase in E_{opt} (see Fig. 1a) and a decrease in n and k. Naturally, the microhardness of the films should also decrease (see Fig. 1b). At $P=0.8$ Torr and $P_{\mathrm{N2}}=40\%$, the values of E_{opt} and H indicate that a polymer-like film is formed with a high hydrogen content. The influence of the pressure in the chamber on the properties of the carbon films is caused by a change in the kinetic energy of

 © 1998 American Institute of Physics

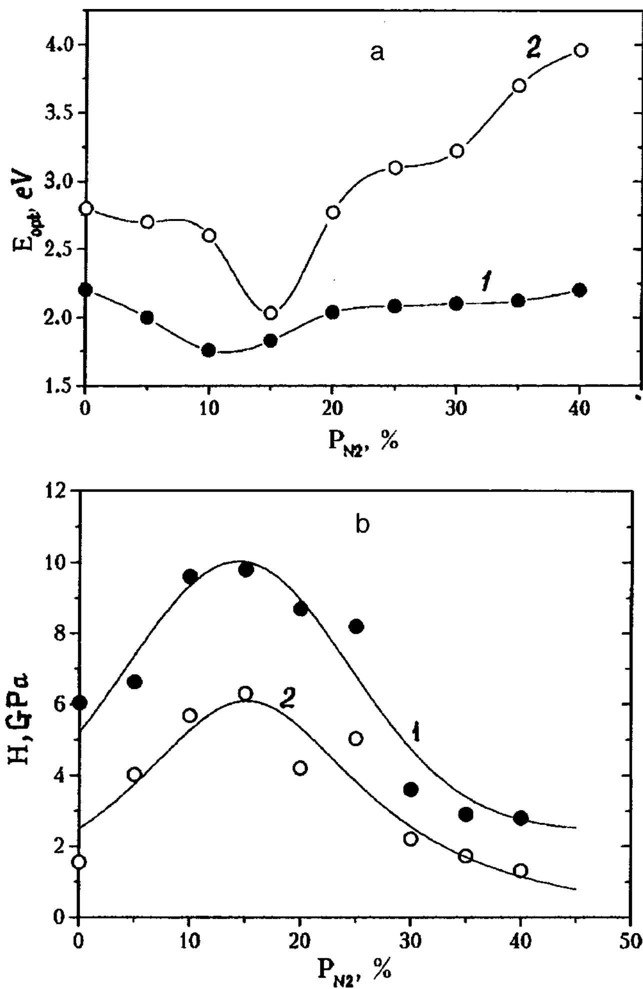

FIG. 1. Optical band gap E_{opt} (a) and microhardness H (b) of a-C : H : N films versus nitrogen content in gas mixture P_{N2}: *1* — $P=0.2$ Torr and *2* — $P=0.8$ Torr.

the ions in the plasma and has already been discussed.[7,8]

These a-C : H : N films were deposited on silicon solar cells to illustrate the scope for their practical application as protective and antireflection coatings. The parameters of the films and the efficiency of the solar cells before and after deposition of the films are given in Table I. Note that two types of films were used. Films obtained at $P=0.2$ Torr and P_{N2} = 10% were used as antireflection coatings (see Series 1 samples in Table I). In this case, the refractive index of the film $n=2.07$ corresponds well to the optimum antireflection condition: $n_{film}=(n_{Si})^{1/2}$ for a single-layer coating.[9] The fairly high value of k and low E_{opt} do not have any significant effect because the light absorption losses are negligible for the film thicknesses used. It can be seen from Table I that the deposition of an a-C : H : N antireflecting film can enhance the efficiency of the solar cell by a factor of almost 1.4 (Sample 1a).

The films exhibit high thermal stability, since thermal annealing did not influence the optical properties of the films or the characteristics of the solar cells (Sample 1b). The considerable hardness of the series 1 films is important for terrestrial applications of solar cells. These a-C : H : N films may also be used as protective coating for solar cells in

TABLE I. Parameters of diamond-like carbon films and efficiency of silicon solar cells before and after deposition of these films.

Sample No.	Diamond-like carbon film: d, nm	n	k	E_{opt}, eV	H, GPa	Solar cell, efficiency, %
1	–	–	–	–	–	10.4
1a	67	2.07	0.12	1.77	9.6	14.0
1b*	67	2.07	0.12	1.77	9.6	14.0
2	–	–	–	–	–	11.2
2a	1500	1.65	0.005	3.96	1.32	10.3
2b**	1500	1.66	0.006	3.93	1.32	10.2
2c***	–	–	–	–	–	4.3

*Sample 1a after annealing at 350°C for 1 h in a nitrogen atmosphere.
**Sample 2a after multienergy implantation of 50 and 100 keV H^+ ions with doses of $3.3\times10^{15}+3.3\times10^{15}$ cm^{-2}.
***Sample 2a after multienergy implantation of 50 and 100 keV H^+ ions with doses of $3.3\times10^{15}+3.3\times10^{15}$ cm^{-2}.

space. In this case, thick films must be used to protect against protons in the solar wind and ultraviolet radiation. The most suitable films for this application are those obtained at $P=0.8$ Torr and P_{N2}=40% (Series 2 samples in Table I) which have low k and high E_{opt}. In this case, the light absorption losses in a 1.5 μm thick film reduce the efficiency of solar cells with these coatings by more than 1% (Sample 2a). Proton irradiation of a a-C : H : N + solar cell structure does not degrade the characteristics of the solar cell (Sample 2b), which indicates that these films possess good radiation resistance. However, the efficiency of an unprotected solar cell drops catastrophically after irradiation (Sample 2c).

In conclusion, these results indicate that changes in the nitrogen content when the other deposition parameters are fixed substantially influence the structure of diamond-like carbon films and can modify their optical and mechanical properties over a wide range. Using these films as antireflection or protective coatings can substantially enhance the efficiency and radiation resistance of silicon solar cells.

This work was supported by the Ukrainian Ministry of Science (Project No. 4.4/406) and by the Ukrainian Science and Technology Center (Project No. 382).

[1] V. A. Semenovich, N. I. Klyui, and V. P. Kostylyov *et al.*, J. CVD **5**, 213 (1997).
[2] M. Allon-Alaluf, J. Appelbaum, M. Maharizi *et al.*, Thin Solid Films **303**, 273 (1997).
[3] A. A. Evtukh, V. G. Litovchenko, R. I. Marchenko *et al.*, J. Vac. Sci. Technol. B **14**, 2130 (1996).
[4] S. B. Kim and J. F. Wager, Appl. Phys. Lett. **53**, 1880 (1988).
[5] Yu. P. Piryatinskii, V. A. Semenovich, N. I. Klyui *et al.*, J. CVD **5**, 207 (1997).
[6] D. Mendoza, J. Aguilar-Hernandez, and G. Contreras-Puente, Solid State Commun. **84**, 1025 (1992).
[7] F. Demichelis, X. F. Rong, S. Schreiter *et al.*, Diamond Relat. Mater. **4**, 361 (1995).
[8] A. Bubenzer, B. Dishler, G. Brandt *et al.*, J. Appl. Phys. **54**, 4590 (1983).
[9] *Physics of Thin Films*, Vol. 2, edited by G. Haas and R. Toon, Mir, Moscow (1967).

Translated by R. M. Durham
Edited by David L. Book